

**VISION BASED NAVIGATION SYSTEM FOR AUTONOMOUS
PROXIMITY OPERATIONS:
AN EXPERIMENTAL AND ANALYTICAL STUDY**

A Dissertation

by

JU-YOUNG DU

Submitted to the Office of Graduate Studies of
Texas A&M University
in partial fulfillment of the requirements for the degree of

DOCTOR OF PHILOSOPHY

December 2004

Major Subject: Aerospace Engineering

**VISION BASED NAVIGATION SYSTEM FOR AUTONOMOUS
PROXIMITY OPERATIONS:
AN EXPERIMENTAL AND ANALYTICAL STUDY**

A Dissertation

by

JU-YOUNG DU

Submitted to Texas A&M University
in partial fulfillment of the requirements
for the degree of

DOCTOR OF PHILOSOPHY

Approved as to style and content by:

John L. Junkins
(Chair of Committee)

Srinivas R. Vadali
(Member)

Johnny Hurtado
(Member)

Shankar P. Bhattacharyya
(Member)

Walter E. Haisler
(Head of Department)

December 2004

Major Subject: Aerospace Engineering

ABSTRACT

Vision Based Navigation System for Autonomous Proximity Operations:
An Experimental and Analytical Study. (December 2004)

Ju-Young Du, B.S., Yonsei University;

M.S., Yonsei University

Chair of Advisory Committee: Dr. John L. Junkins

This dissertation presents an experimental and analytical study of the Vision Based Navigation system (VisNav). VisNav is a novel intelligent optical sensor system invented by Texas A&M University recently for autonomous proximity operations. This dissertation is focused on system calibration techniques and navigation algorithms. This dissertation is composed of four parts. First, the fundamental hardware and software design configuration of the VisNav system is introduced. Second, system calibration techniques are discussed that should enable an accurate VisNav system application, as well as characterization of errors. Third, a new six degree-of-freedom navigation algorithm based on the Gaussian Least Squares Differential Correction is presented that provides a geometrical best position and attitude estimates through batch iterations. Finally, a dynamic state estimation algorithm utilizing the Extended Kalman Filter (EKF) is developed that recursively estimates position, attitude, linear velocities, and angular rates. Moreover, an approach for integration of VisNav measurements with those made by an Inertial Measuring Unit (IMU) is derived. This novel VisNav/IMU integration technique is shown to significantly improve the navigation accuracy and guarantee the robustness of the navigation system in the event of occasional dropout of VisNav data.

To my parents, my husband, Won-Hyouk Jang, and my lovely son, Hyoung-wuk

ACKNOWLEDGMENTS

I would like to express my most sincere appreciation to my advisor, Dr. John L. Junkins, for his academic guidance and financial support throughout my graduate studies. Without enthusiastic encouragement from Dr. Junkins, this work could not have been completed.

I would also like to thank my committee members, Dr. Srinivas R. Vadali, Dr. Johnny Hurtado, and Dr. Shankar P. Bhattacharyya for helpful advice and support. Special thanks go to Dr. Declan Hughes for discussions, technical support and expert knowledge of the VisNav system hardware. Also, I would like to thank Ms. Lisa Willingham, Administrative Assistant to Dr. John L. Junkins, for her assistance and kindness.

I would like to express my gratitude from the bottom of my heart to my parents for endless love and belief throughout my whole life. In addition, I would like to express my special thanks to my sister-in-law for taking care of my son during my preparing of this dissertation and many thanks to all family members.

Finally, thanks to my dear husband, Won-Hyouk Jang, who kept me focused on finishing this research and my lovely son, Hyoung-wuk.

TABLE OF CONTENTS

		Page
ABSTRACT.....		iii
DEDICATION.....		iv
ACKNOWLEDGMENTS.....		v
TABLE OF CONTENTS.....		vi
LIST OF TABLES.....		viii
LIST OF FIGURES.....		ix
CHAPTER		
I	INTRODUCTION.....	1
	1.1 Background.....	1
	1.2 New Features of the VisNav System.....	4
	1.3 Objective and Outlines.....	5
II	VISNAV SYSTEM CONFIGURATION.....	7
	2.1 VisNav System Geometry	7
	2.2 VisNav Sensor	10
	2.3 Beacon Assembly.....	12
	2.4 Electronics.....	15
	2.4.1 Digital Signal Processor.....	16
	2.4.2 Beacon Controller.....	17
III	VISNAV SENSOR CALIBRATION	22
	3.1 Experimental Configuration.....	23
	3.2 Global Calibration.....	31
	3.2.1 Traditional Distortion Model.....	31
	3.2.2 Bivariate Polynomial Model.....	32
	3.3 Weighted Averaging Method.....	39
	3.4 Two Step Calibration Process.....	41
	3.5 Calibration Summary.....	44
IV	RELATIVE POSITION AND ATTITUDE ESTIMATION.....	46
	4.1 Attitude Parameterization.....	47
	4.2 Measurement Model.....	50

CHAPTER	Page
4.3 Measurement Sensitivity Matrix.....	50
4.4 Gaussian Least Square Differential Correction.....	52
V DYNAMIC STATE ESTIMATION.....	57
5.1 Extended Kalman Filter Description.....	57
5.2 Zero Acceleration Dynamic Model.....	59
5.3 VisNav/IMU Integration.....	61
5.3.1 IMU Measurement Model.....	62
5.3.2 Extended Kalman Filter with VisNav/IMU Integration...	64
VI SIMULATION STUDIES.....	66
6.1 GLSDC Implementation.....	66
6.2 EKF Implementation with Zero Acceleration Model.....	73
6.3 EKF Implementation with VisNav/IMU Integration.....	78
6.4 Discussion.....	85
VII SUMMARY AND CONCLUSION.....	87
REFERENCES.....	89
VITA.....	93

LIST OF TABLES

TABLE		Page
1	Vision Sensor Specifications.....	20
2	Beacon Controller Specifications.....	21
3	Beacon Specifications.....	21
4	Specifications of Crossbow IMU-300CB.....	63
5	Initial Guess of GLSDC.....	69
6	Acceleration and Gyro Error Specifications for the IMU.....	78
7	Navigation Accuracy Summary.....	85

LIST OF FIGURES

FIGURE	Page
1 Spacecraft docking using VisNav system.....	5
2 VisNav system geometry.....	8
3 PSD sensitivity and LED emission characteristics.....	11
4 VisNav sensor.....	13
5 VisNav sensor structure.....	13
6 Beacon boxes.....	14
7 Beacon structure.....	14
8 VisNav electronic schematic.....	15
9 Experimental setup.....	24
10 Nonlinearity of output voltages for the one dimensional test with fixed pitch angle = 0°	26
11 Standard deviation of output voltages for the one dimensional test with fixed pitch angle = 0°	27
12 Relative target locations for calibration test.....	28
13 Ideal image coordinates, (y, z)	29
14 Actual VisNav sensor outputs, (V_y, V_z)	29
15 Standard deviation of V_y	30
16 Standard deviation of V_z	30
17 Bivariate basis functions.....	34
18 Order of polynomial basis vs y calibration accuracy.....	37
19 Order of polynomial basis vs y calibration accuracy.....	37
20 y axis calibration errors of 25 th order Chebyshev polynomial calibration function.....	38
21 z axis calibration errors of 25 th order Chebyshev polynomial calibration function.....	38

FIGURE	Page
22 Local surface averaging.....	39
23 Four preliminary surfaces.....	40
24 Weighting functions.....	40
25 y axis calibration errors of two step calibration function.....	43
26 z axis calibration errors of two step calibration function.....	43
27 Radial distance of calibrated images vs standard deviation of calibration errors.....	44
28 Gaussian Least Squares Differential Correction algorithm.....	56
29 Simulated trajectory.....	67
30 Beacons' configuration.....	67
31 Time evolution of the image coordinates corresponding to the simulated trajectory.....	68
32 Condition numbers of GLSDC.....	70
33 Iteration numbers of GLSDC.....	70
34 Position/attitude errors and 3-sigma bounds of GLSDC (Approach phase).....	71
35 Position/attitude errors and 3-sigma bounds of GLSDC (End-game).....	72
36 Position/attitude errors and 3-sigma bounds of EKF with zero acceleration model (Approach phase).....	74
37 Position/attitude errors and 3-sigma bounds of EKF with zero acceleration model (End-game).....	75
38 Linear velocity/angular rate errors and 3-sigma bounds of EKF with zero acceleration model (Approach phase).....	76
39 Linear velocity/angular rate estimation and 3-sigma bounds of EKF with zero acceleration model (Approach phase).....	77
40 Position/attitude errors and 3-sigma bounds of EKF with IMU (Approach phase).....	80
41 Position/attitude errors and 3-sigma bounds of EKF with IMU (End-game).....	81
42 Linear velocity/angular rate errors of EKF with IMU (Approach phase)....	82

FIGURE		Page
43	Linear velocity/angular rate estimation of EKF with IMU (Approach phase).....	83
44	Accelerometer bias/ gyro bias estimation of EKF with IMU (Approach phase).....	84

CHAPTER I

INTRODUCTION

NASA is pursuing autonomous proximity navigation technologies to make access to space safer, more reliable, and less expensive for many customers. Likewise many other commercial and military scenarios include autonomous proximity operations, inspection, self-assembly. The Vision Based Navigation (VisNav) system developed at Texas A&M University is a low-cost, flexible, and robust navigation system. VisNav applies an adaptive approach in which cooperative active beacons and commanded via real-time feedback, to optimize navigation accuracy. Owing to the many attractive features of the VisNav system as discussed herein, VisNav has widespread possibility for applications, such as spacecraft rendezvous and docking, aerial refueling, formation flying, and space robotic manipulation in aerospace industry, as well as motion capture, and intelligent robotic applications in many other fields. The purpose of this dissertation is to present fundamental calibration techniques and navigation algorithms for the VisNav system application, and validation using analytical studies and by application to experimental data.

1.1 Background

Precise six degree-of-freedom relative position and attitude determination represents an important and challenging problem for proximity operations. For a number of years, position sensing systems used for autonomous navigation have been accomplished by a variety of means including dead reckoning sensors and external sensors [1].

This dissertation follows the style and format of *IEEE Transactions on Automatic Control*.

Dead reckoning sensors measure a subset of dynamic quantities such as velocity, acceleration, and angular velocity. This information is then used with a kinematic model of the vehicle in order to predict future motion. Most dead reckoning sensors are inertial sensors. For example, the Inertial Measurement Unit (IMU) provides densely measured linear acceleration and angular rate by 3 axial accelerometers and 3 axial gyroscopes [2], [3]. The IMU can capture the fast dynamics of a maneuverable vehicle such as an aircraft due to its high bandwidth and high sampling rate. In addition, prediction using an IMU typically does not rely on any external aids and does not necessary to emit or receive any detectable radiation. However, IMU measurements are usually corrupted by initial condition errors, noise, bias and drift variation, so that the navigation errors may be accumulated and lead to significant errors in the position, velocity, and attitude output.

External sensors provide position information through the direct observation of landmarks or beacons, either natural or artificial. Radars, laser ranging systems, ultrasonic sensors, image-based sensors, and Global Positioning System (GPS) sensors belong to the category of external sensors. However, there are always limitations on accuracy, bandwidth, and flexibility for applications of these existing external sensor systems. Radars, laser ranging systems, and ultrasonic sensors provide accurate range information, however there is a significant difference between measuring the range and solving the full six degree-of-freedom navigation problem [4].

GPS is the most common navigation system in use today [5]. GPS provides real time absolute or relative position data, but the accuracy and bandwidth are limited compared to the typical requirements of relative proximity operation. A number of difficulties associated with geometric dilution of precision, integer ambiguity resolution, multipath must be resolved for each application. For example, when a spacecraft approaches the ISS to perform rendezvous and docking, the signals from the GPS satellites may be blocked and degraded by multipath signals reflected by the ISS. Differential GPS (DGPS) can partially address these problems and under ideal circumstances can lead to high accuracy, especially if coupled with an IMU.

The Video Guidance Sensor (VGS) is considered as a candidate proximity navigation sensor by NASA [6], [7]. The VGS is an optical sensor that measure the range and attitude of the chase vehicle relative to the target vehicle in the terminal phase of automated rendezvous and capture, out to about 100 meters [7]. It employs a Charge Coupled Device (CCD) camera mounted on the chaser to image a set of passive reflective targets located on the target vehicle. The target reflectors are illuminated using an array of laser diodes collocated with the camera and the resulting 2D camera image is processed to produce an estimate of the relative six degree-of-freedom. The relative range accuracy of VGS is a few centimeters in each axis and the accuracy of the relative attitude is less than 0.3 degrees in each axis [7], [8], [9]. However, VGS has a narrow field-of-view (30 degrees) and the relative range and relative attitude are computed with a slow rate of about 2Hz. This slow update rate is adequate for slow spacecraft relative motions but not for many other applications. All kinds of image-based navigation systems that use CCD cameras require a substantial burden for image processing or pattern recognition or target identification. So these systems usually have slow data update rates and may suffer from occasional failures of the pattern recognition or target identification.

Texas A&M University researchers have developed an analog vision sensor system (VisNav) and associated software algorithms in order to overcome above weaknesses of the existing image based navigation. VisNav makes use of Position Sensing Diode (PSD) technology which has a fast rise time of a few microseconds and provides a direct sensor reading that indicates the centroid location of the incident light, and thereby permits the very fast measurements for estimating position and attitude of moving object. The fast rise time allows the beacon energy to be structured in the frequency domain to ensure reliable discrimination and rejection of ambient energy. The fast rise time also allows time sequential imaging of many beacons, as well as many other additional desirable features as discussed below.

1.2 New Features of the VisNav System

The VisNav system comprises a new type of analog electro-optical sensor combined with specific structured light sources called beacons in order to achieve a selective or “intelligent” vision [10]. The VisNav sensor is made up of a PSD placed in the focal plane of a wide-angle lens. When the active area of the PSD is illuminated by energy from a beacon focused by the lens, it generates electrical currents in four terminals on each side of the PSD. These currents can be processed with appropriate electronic and digital processing equipment to accurately measure the line-of-sight vector directions of the incident energy. The Digital Signal Processor (DSP) embedded in the VisNav sensor calculates the six degree-of-freedom position and attitude estimates using these line-of-sight vector measurements. The VisNav technology has many attractive features including:

- Smart vision sensor with embedded DSP.
- Wide field-of-view by unique optical design.
- Small size, light weight, and low cost.
- All solid state, no moving parts, and simple electronics.
- No reliance on external systems.
- Maximum signal to noise ratio by beacon orchestration via active feedback.
- Depth-of-field can vary from a few centimeters to infinity, due to fisheye optics.
- Zero image processing or pattern recognition by the PSD technology.
- Excellent rejection of light disturbance under various operating conditions.
- High accuracy: fraction of a centimeter relative position error and a small fraction of a degree relative attitude error
- High bandwidth: navigation data updated at 100 Hz or faster, to enable general feedback control of proximity operations without any other motion sensor.

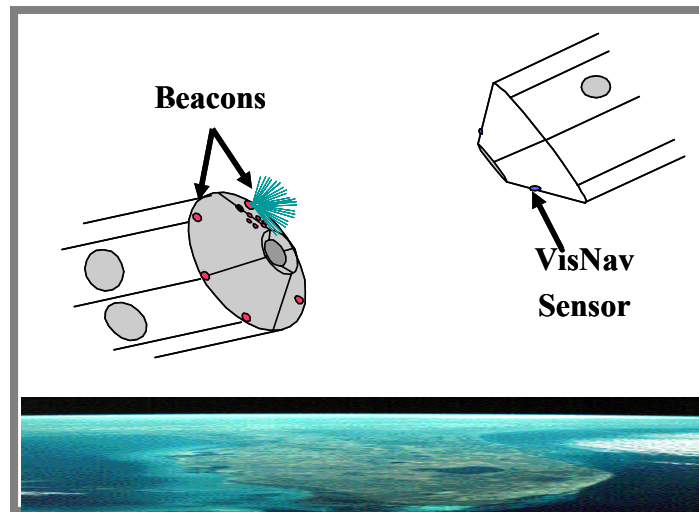


Figure 1. Spacecraft docking using VisNav system

Due to these advantages, the VisNav system can be an effective starting point to realize precise and versatile proximity navigations. Furthermore, the VisNav system can be used for a variety of applications due to its flexible configurations [11], [12], [13]. Figure 1 illustrates the autonomous rendezvous and docking using the VisNav system. The Vision sensor fixed on the chase spacecraft is designed to measure the line-of-sight vectors from the sensor to beacons attached on the reference target spacecraft or space station.

1.3 Objective and Outlines

The objective of this research is to develop calibration and navigation algorithms and software for the VisNav system and to use these to evaluate that the new VisNav system performance for proximity navigation through laboratory experiments and numerical simulation studies.

Laboratory experiments have been conducted to collect the vision sensor data and develop the calibration methodology to improve the VisNav system accuracy. In order to perform the calibration, the global calibration models have been developed based on optimal approximation using bivariate Chebyshev polynomials. In addition, local

calibration functions using a weighted averaging method have been investigated to achieve a required accuracy.

Navigation algorithms to estimate the six degrees-of-freedom relative motion of two vehicles using the VisNav system have been developed. A Gaussian Least Square Differential Correction (GLSDC) method using Modified Rodrigues Parameters (MRPs) has been developed to determine the best geometric position and attitude estimates from each set of four or more measurements through batch iterations. An Extended Kalman Filter (EKF) then improves the navigation accuracy and estimates an optimal linear velocity and angular rate trajectory consistent with these geometric solutions.

The applicability of the EKF depends upon the availability of an adequate dynamical model or direct measurement of velocity or acceleration. However, dynamical modeling for aircraft and spacecraft includes many difficulties in applying valid torque and force models. Moreover, the VisNav system has a risk of intermittent data dropout due to occasional situations where too few beacons are within the field-of-view (FOV). Therefore, the integration of VisNav and IMU using the complementary EKF provides a more precise and robust proximity navigation solution. The above navigation algorithms have been fully developed and their feasibilities are demonstrated through numerical simulations.

In Chapter II, the fundamental hardware and software design configuration of the VisNav system is described. In Chapter III, system calibration techniques designed to enable more accurate VisNav system application are investigated. In Chapter IV, six degree-of-freedom navigation algorithms based on the GLSDC are presented. In Chapter V, an EKF algorithm is established, using a piecewise nominal zero acceleration model and also a second EKF approach using integration of VisNav measurements with acceleration and rate measurements from an Inertial Measuring Unit (IMU). Finally, all algorithms will be demonstrated by numerical simulations.

CHAPTER II

VISNAV SYSTEM CONFIGURATION

The VisNav system consists of a set of active optical targets (Beacons) each radiating bursts of light modulated at a carrier frequency, a small electro-optical VisNav sensor that senses the image plane centroid locations of these light packets from the beacons, and controlling electronics such as signal controller and beacon controller for both the VisNav sensor and the beacons.

2.1 VisNav System Geometry

The basic geometry of the class of optical sensor systems under consideration is based on the perspective projection in which all object space points are projected onto the image plane through one point called the perspective center, C in Figure 2. Point o is the principal point which is optical center defined mathematically as the foot of the perpendicular dropped from the perspective center to the image plane and P_i is the image point. This geometrical camera model approach is usually known as the pin-hole camera model and represents an idealization of any actual sensor. The x-axis of the Image Space Coordinate frame (ISC) is defined to be directed outward along the bore-sight and the image plane placed at the focal plane of the lens. Then their coordinates in the ISC are: for C $(0, y_o, z_o)$; for o $(-f, y_o, z_o)$; for P_i $(-f, y_i, z_i)$. Where f is the effective focal length of lens. The line-of-sight vector \mathbf{B} defined by the line from image point P_i to the camera exposure position C in ISC is represented by

$$\mathbf{B}_i = \begin{pmatrix} f \\ -(y_i - y_o) \\ -(z_i - z_o) \end{pmatrix} \equiv \begin{pmatrix} f \\ -\bar{y}_i \\ -\bar{z}_i \end{pmatrix} \quad (2.1)$$

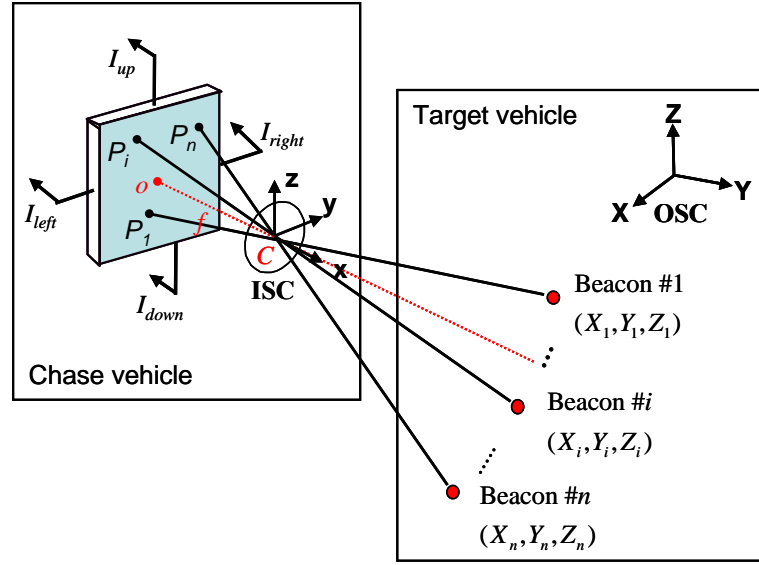


Figure 2. VisNav system geometry

where \bar{y}_i and \bar{z}_i are the displacements of image coordinates along the y and z axis from the optical center (y_o, z_o) . The coordinates of the perspective center in the Object Space Coordinate frame (OSC) are (X_c, Y_c, Z_c) and the coordinates of the i^{th} beacon in the OSC is (X_i, Y_i, Z_i) . So, the line-of-sight vector \mathbf{R} defined by the line from camera exposure position C to i^{th} beacon location is represented in the OSC frame by

$$\mathbf{R}_i = \begin{pmatrix} X_i - X_c \\ Y_i - Y_c \\ Z_i - Z_c \end{pmatrix} \quad (2.2)$$

The attitude describes the angular spatial relationship between the OSC and ISC frames. There are several attitude parameters such as Euler angles, Quaternion, classical Rodrigues parameters, and modified Rodrigues parameters. The relationship between the OSC and ISC is expressed by a 3×3 orthogonal matrix named by direction cosine matrix, A . The nine elements of A are functions of the chosen attitude parameters and is taken by convention to transformation from the OSC to ISC. Geometrically, the line-

of-sight vector, \mathbf{B} and \mathbf{R} are collinear for the ideal pin-hole camera [14]. Thereby, the following relationship can be derived.

$$\mathbf{B}_i = k\mathbf{A}\mathbf{R}_i \quad (2.3)$$

Note that k is an unknown scale factor. The Eq. (2.3) is the ideal pin-hole camera model that represents the relationship between the object space vector and the corresponding ideal image space vector. Eq. (2.3) can be written by

$$\begin{pmatrix} f \\ -\bar{y}_i \\ -\bar{z}_i \end{pmatrix} = k \begin{bmatrix} A_{11} & A_{12} & A_{13} \\ A_{21} & A_{22} & A_{23} \\ A_{31} & A_{32} & A_{33} \end{bmatrix} \begin{pmatrix} X_i - X_c \\ Y_i - Y_c \\ Z_i - Z_c \end{pmatrix} \quad (2.4)$$

Rearranging Eq. (2.3) and eliminating the proportional constant k

$$\bar{y}_i = g_{y,i}(X_i, Y_i, Z_i, X_c, Y_c, Z_c, A) = -f \frac{A_{21}(X_i - X_c) + A_{22}(Y_i - Y_c) + A_{23}(Z_i - Z_c)}{A_{11}(X_i - X_c) + A_{12}(Y_i - Y_c) + A_{13}(Z_i - Z_c)} \quad (2.5)$$

$$\bar{z}_i = g_{z,i}(X_i, Y_i, Z_i, X_c, Y_c, Z_c, A) = -f \frac{A_{31}(X_i - X_c) + A_{32}(Y_i - Y_c) + A_{33}(Z_i - Z_c)}{A_{11}(X_i - X_c) + A_{12}(Y_i - Y_c) + A_{13}(Z_i - Z_c)} \quad (2.6)$$

Eq. (2.5) and Eq. (2.6) are called the co-linearity equations. From the knowledge that the line-of-sight unit vector of i^{th} beacon can be written in unit vector form in ISC

$$\mathbf{b}_i = \frac{1}{\sqrt{f^2 + \bar{y}_i^2 + \bar{z}_i^2}} \begin{pmatrix} f \\ -\bar{y}_i \\ -\bar{z}_i \end{pmatrix} \quad (2.7)$$

and in OSC

$$\mathbf{r}_i = \frac{1}{\sqrt{(X_i - X_c)^2 + (Y_i - Y_c)^2 + (Z_i - Z_c)^2}} \begin{pmatrix} (X_i - X_c) \\ (Y_i - Y_c) \\ (Z_i - Z_c) \end{pmatrix} \quad (2.8)$$

Then, the collinear relationship in Eq. (2.3) can also be reconstructed in unit vector form:

$$\mathbf{b}_i = A\mathbf{r}_i \quad (2.9)$$

Also, it is evident from Eq. (2.4) that the geometric interpretation of scale factor k is

$$k = \frac{\sqrt{f^2 + \bar{y}_i^2 + \bar{z}_i^2}}{\sqrt{(X_i - X_c)^2 + (Y_i - Y_c)^2 + (Z_i - Z_c)^2}} \quad (2.10)$$

2.2 VisNav Sensor

The VisNav sensor is made up of a Duo-Lateral Position Sensing Diode (PSD) [15] placed in the focal plane of a wide angle fisheye lens. The PSD is sensitive across a broad color spectrum, peaking near 900nm; this allows one to select the beacon's color (wavelength) with great freedom, but one should emphasize the near infrared region (800 to 1000 nm) where the PSD sensitivity is near maximum. Figure 3 shows the PSD Sensitivity and LED Emission characteristic.

The PSD consists of a silicon substrate and a resistive layer. When the active silicon area of the PSD is illuminated by incident energy, it will generate a photo-current, which flows from the point of incident through the resistive layer to the terminal. The resistivity of the resistive layer is nominally uniform so the photo-current at each terminal is approximately inversely proportional to the distance between the incident spot location of light and terminals. For example, if the input light spot is exactly at the PSD center then equal current signals would be expected through each of the four terminals. Thereby, the imbalance of the currents of left and right terminal show the light centroid location of horizontal direction and the imbalance of the currents of up and down terminal show the light centroid location of the vertical direction.

Each pair of horizontal and vertical current imbalances generated is almost linearly proportional to the horizontal and vertical location, respectively, of the centroid of the light beam onto the PSD active area. While the individual currents depend on the intensity of the light, their non-dimensionalized current imbalances are nominally not dependent on the intensity.

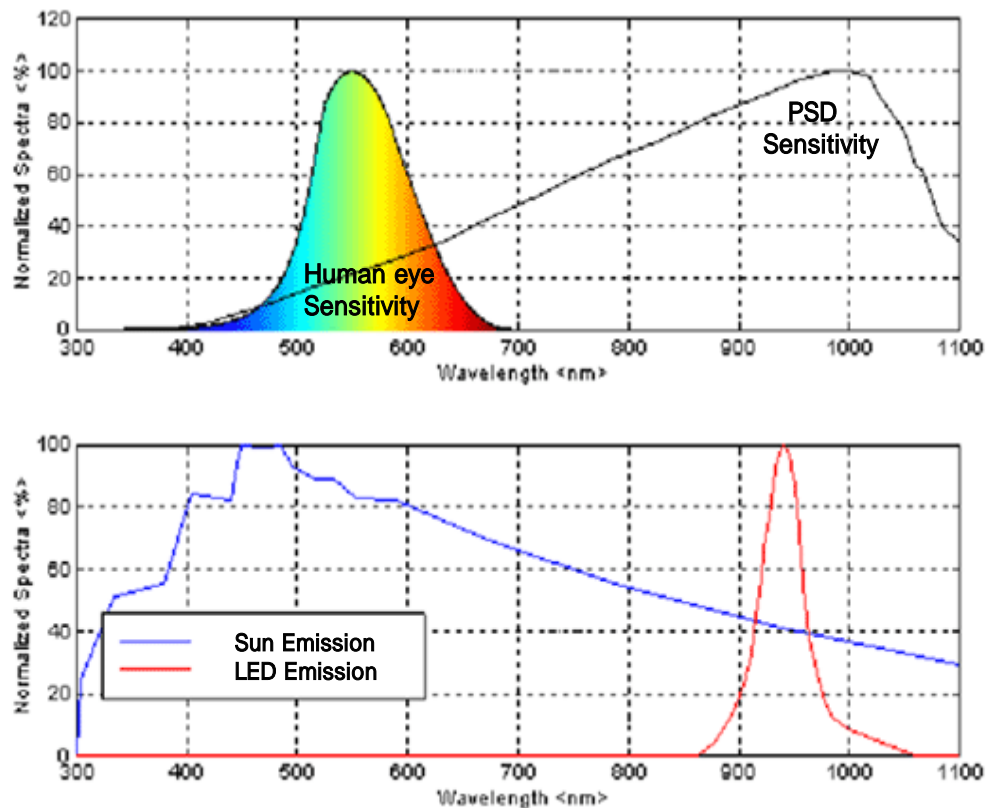


Figure 3 PSD sensitivity and LED emission characteristics

These ideal proportionalities and de-coupling only approximate the actual PSD behavior; the coupling and lens distortion must be determined by calibration.

A second order dependence arises due to signal-to-noise consideration, therefore we prefer to keep the sum of the currents is an ideal range around 70% of the saturation intensity. Therefore, active feedback is used to command each individual beacon to maintain received energy in the optimal range for maximum signal to noise.

The PSD has very fast rising time, about 5 micro seconds, so it is capable of “seeing” targets at thousands of “frames” per second. Moreover, The PSD offers outstanding position linearity, high analog resolution, and simple operating circuits. The position non-linearity is defined as the geometric position error divided by the detector

dimension. Position non-linearity of currently used duo-lateral PSD is less than 0.3% [15], [16], and systematic errors can be corrected via calibration.

Figure 4 and Figure 5 show that the VisNav sensor structure. The 18mm diameter fisheye lens that has a focal length of $f = 10mm$ collects the light from a cone of angle ± 45 degrees field-of-view and focus the incident energy onto the PSD active area. A narrow bandpass passive color filter is placed in front of the lens in order to reject most ambient light noise and therefore reduce shot noise which is known to be proportional to the square root of the total energy incident on the detector.

2.3 Beacon Assembly

Figure 6 shows these sizes of beacon prototypes. These are laboratory prototypes, future beacons are expected to be much smaller. Figure 7 shows the beacon structure. The command to one of beacons is shown; time multi-plexing is used to activate the beacon sequentially for 0.001 second each. The beacons used in the VisNav system are composed of omni-directional light emitting diodes (LEDs) that radiate energy over a near hemispherical shape. Each of those shown in Figure 7 is actually an array of LEDs, and has a diffuser element in order to make light have reduced intensity variations. This design was adopted because low power LEDs are very inexpensive and reliable. The wavelength of the LEDs used in the beacons is 880nm (Near Infra Red region), which is invisible to the human eye. This wavelength was chosen to be close to the optimal response wavelength of the PSD. The advantages of using LEDs are compact size, high bandwidth, low cost, long life, and good power efficiency. The number of LEDs used to form a beacon depends on the cost, type of LED, required signal-to-noise ratio, and the maximum operating distance. It is expected that the optimal design will be “dime-size” beacons. The beacons of Figure 7 have the advantage of being eye-safe and this consideration is to avoid the optimal higher energy density design in these laboratory studies.



Figure 4 VisNav sensor

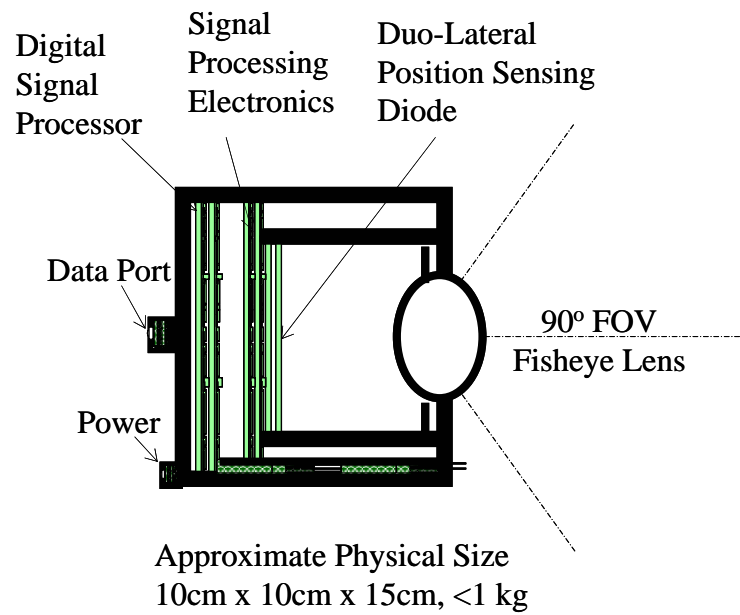


Figure 5 VisNav sensor structure



Figure 6 Beacons boxes

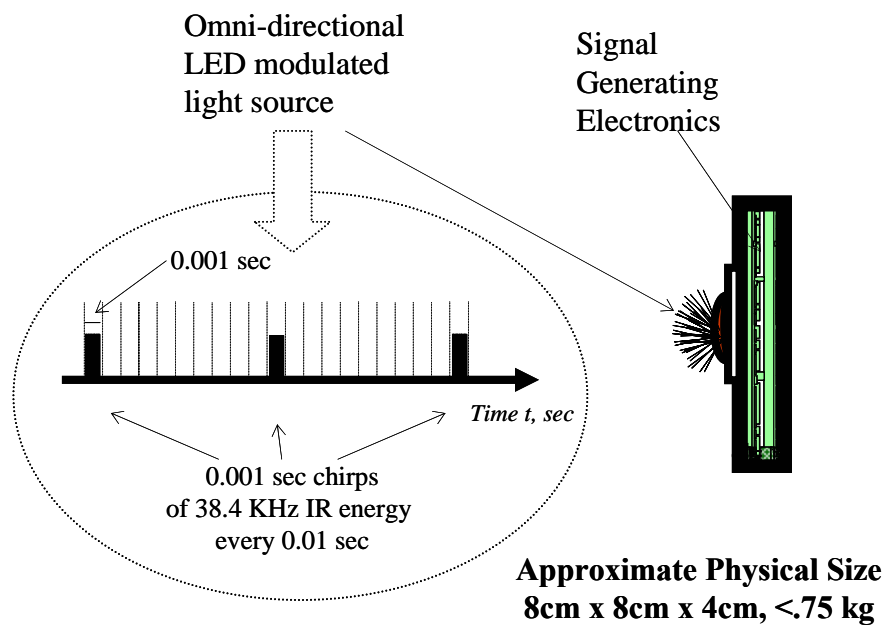


Figure 7 Beacon structure

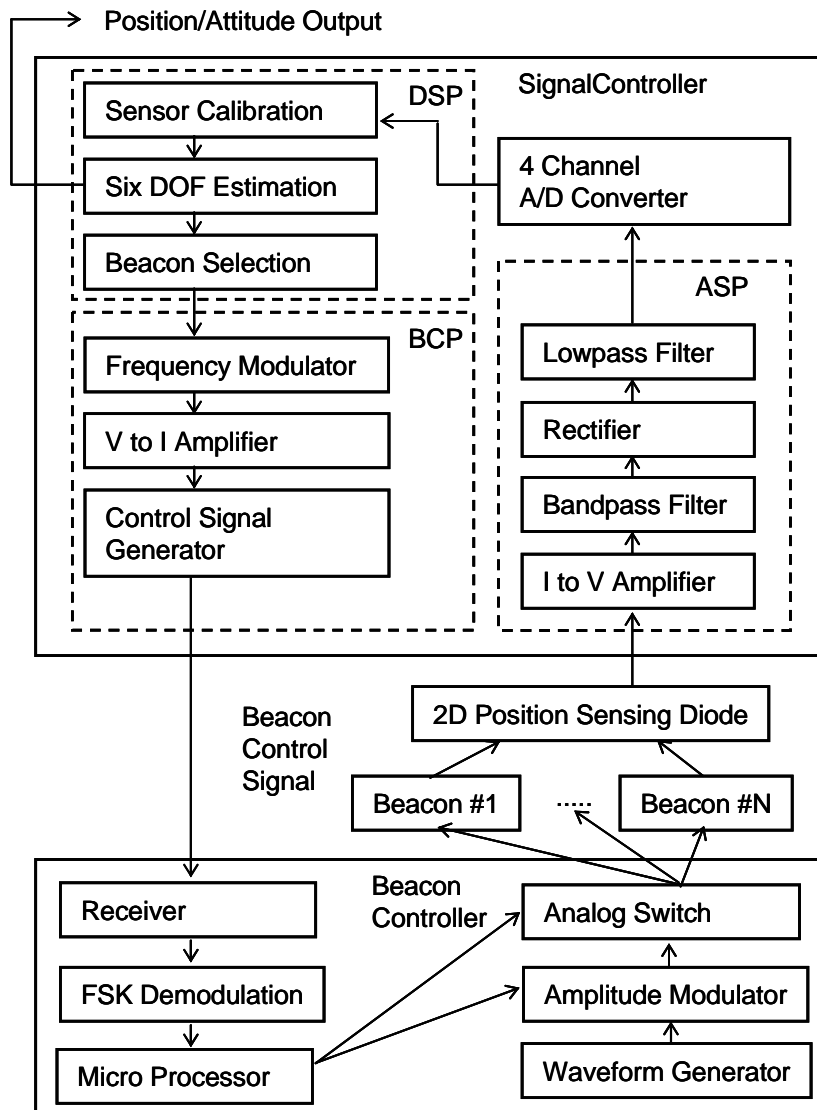


Figure 8. VisNav electronic schematic

2.4 Electronics

Figure 8 shows that the electronic schematic of the VisNav system. The VisNav system's main subsystems are the signal controller and the beacon controller. The signal controller includes the Analog Signal Processing system (ASP), Digital Signal Processor (DSP), and Beacon Control Processor (BCP).

The ASP receives output current signals, $I_{left}, I_{right}, I_{up}, I_{down}$ generated by PSD in response to receiving an optical signal from a beacon. The ASP is comprised of current-to-voltage amplifiers, a bandpass filter, a rectifier, and a lowpass filter. Amplifiers receive output current signals, $I_{left}, I_{right}, I_{up}, I_{down}$ from VisNav sensor and converts to scaled electrical voltages. Then the bandpass filter removes unwanted frequency noise and disturbance signals, and outputs bipolar voltages. Rectifiers convert bipolar voltages to unipolar voltages. A lowpass filter smoothes voltages to final outputs, $V_{left}, V_{right}, V_{up}, V_{down}$. These voltages $V_{left}, V_{right}, V_{up}, V_{down}$ are digitized by an Analog-to-Digital (A/D) converter operable to run as a DSP input device.

2.4.1 Digital Signal Processor

The DSP receives the digitized voltage signals $V_{left}, V_{right}, V_{up}, V_{down}$ from the ASP and determines the non-dimensionalized horizontal and vertical normalized voltages signals, V_y, V_z by comparing voltage signals to each other using the following definition:

$$\begin{aligned} V_y &= \frac{V_{right} - V_{left}}{V_{right} + V_{left}} \\ V_z &= \frac{V_{up} - V_{down}}{V_{up} + V_{down}} \end{aligned} \quad (2.11)$$

Notice that these normalized voltages measure the location of the light centroid on PSD of an optical signal and thus, the direction of the corresponding beacon relative to axis of ISC. Then normalized voltages can be mapped into corresponding ideal pin-hole camera model image coordinates using the nonlinear calibration functions. In Chapter III, the calibration process will be discussed in detail.

Also, the DSP commands which beacon is to be turned on next, and at what intensity power in order to optimize the signal to noise level of the received signal considering, the maximum PSD current level induced the last time, and also sends a two byte package of these data to the beacon controller via an infrared or radio data link.

Specifically, the DSP commands a small percentage increase or decrease (1% in the current prototype) in each beacon's emitted power 100 times per second. Finally, the DSP executes the six degree-of-freedom navigation algorithms which estimate the position and attitude of sensor fixed frame based on Gaussian Least Square Differential Correction and the Extended Kalman Filter. In Chapter IV and Chapter V, the six degree-of-freedom navigation algorithms will be discussed in detail. The overall data update rate is 100Hz for the current VisNav system prototype. This is sufficient for controlling most proximity operations anticipated and is much better than competing approaches. The choice of DSP depends on several factors including sampling frequency, computational requirements, amounts of parallelism in the algorithm, programmability, power consumption, design time, and non-recurring costs. We chose a 16-bit fixed-point DSP TMS320C55 manufactured by Texas Instruments due to the system flexibility. We do not claim this is the optimal processor, but it has proven satisfactory.

The Beacon Control Processor (BCP) comprises a frequency modulator, a voltage-to-current amplifier, and control signal generator. In operation, the frequency modulator receives the information regarding the next beacon to be activated from the DSP and encodes the information as a frequency shift keyed voltage signal. After encoding, the voltage-to-current amplifier and converts the frequency shift keyed voltage signal to frequency shift keyed current signal. The frequency shift keyed current signal is then transmitted to control signal generator to generate control signal transmitted to beacon controller.

2.4.2 Beacon Controller

The beacon controller comprises a signal receiver, a frequency demodulator, and micro processor. The signal receiver is operable to receive the control signal generated by control signal generator. The demodulator demodulates control signal and transmits digital information to the processor regarding the next beacon to be activated. The beacon controller is comprised by a waveform generator, an amplitude modulator, and an analog switch. A waveform generator generates a time varying voltage wave form for

the optical signals generated by the beacons. The amplitude modulator determines and sets a peak voltage level for the time varying voltage waveform. Then the time varying voltage waveform is transmitted to an analog switch which is controlled by the micro processor for the activation and deactivation of the beacons. Thus, the optical signals generated by the beacons are separated from background or ambient light using an analog signal processing system, essentially a matched filter that takes advantage of the fact that the beacon waveform is known. For example, in operation, unwanted background light from extraneous sources such as the sun, computer monitors or light fixtures would also be focused on PSD, thereby generating electrical currents associated with these extraneous light sources. However, the light strength of beacon required to sufficiently dominate the extraneous electrical currents would be undesirably large and could constitute a safety hazard. Thus, small optical signals generated by beacons are varied at a unique waveform, and at sufficiently high frequencies that a matched filter can be used to distinguish optical signals from lower frequency variations of extraneous light sources. As a consequence, only the beacon energy not rejected by the matched filter is centroided and thus we achieve a high degree of robustness to ambient energy results.

For example, a simple sine or square wave on/off modulation at 40,000 switches per second, and left on for an interval of 0.001 seconds may be used. During intervals where all of beacons are not activated, the frequency of the extraneous light source currents generated by PSD may be monitored to check the ambient noise and to ensure appropriate modulation frequency selection. (i.e., there is near negligible ambient energy that comes through the matched filter) Currently, a 38.4 KHz sinusoidal carrier signal is applied to each beacon control current so the resulting beacon energy incident on the PSD and the output signal currents then varies sinusoidally at the same frequency. This frequency was chosen as a compromise between good rejection of low frequency background light, and to minimize the VisNav sensor noise that was found to occur at higher frequencies. Additionally, the amount of optical energy received from each beacon by the VisNav sensor depends upon many factors, including, but not limited to,

the radiation pattern of a particular beacon, the position and attitude of the VisNav sensor system relative to a beacon, and the conditions of the intervening medium such as water content. Since some of these factors may vary widely in operation, the strength of optical signals for particular applications may saturate the amplifier, especially if the light path length between a beacon and VisNav sensor is relatively small. At other times, the strength of optical signals broadcast by the beacons may be too weak, resulting in an unsatisfactorily small output signal to noise ratio of the VisNav sensor. However, we know a distance squared relationship exists between the transmitted and received energy. Thus, for example, a tenfold change in the distance between a beacon and VisNav sensor requires on the order of the hundred fold change in the emitted energy of beacon to maintain optimal signal to noise ratio of the measurements of VisNav sensor.

In accordance with the VisNav invention, the system rapidly and automatically adapts to the varying distance and environmental conditions by controlling the amplitude of the time varying optical signal energy broadcast by each beacon. Thus system adapts to maintain the maximum of the output current signals generated by VisNav sensor at some fixed percentage about 25% less than 100% of the saturation level of amplifier. Experiments indicate variation of $\pm 5\%$ about the ideal received energy has negligible impact on the signal to noise ratio, so this is a first order sensitivity to beacon energy that indicates an ideal situation as regards system robustness. The ideal output current signal level may be identified as I_x and may be determined to optimize the signal to noise ratio of VisNav sensor, for each individual measurement. The specification each of the VisNav prototype system is summarized in Table 1 - Table 3.

Table 1 Vision sensor specifications

Mass	< 1 Kg
Dimensions	< 10 x10 x15 cm
Electrical Power	< 1.4 A at +5 V (7 W) < 0.4 A at +12 V (4.8 W) < -0.4 A at -12 V (4.8 W)
Sensor Data Position Format	X, Y and Z cartesian coord. wrt. the SmartLight coordinate frame.
Sensor Data Angular Format	Modified Rodrigues Parameter wrt. the SmartLight coordinate frame.
Data Byte Format	4 bytes per DEGREE-OF-FREEDOM 4 framing/control bytes
Output Data Electrical Format	RS-485 transmit and receive channels
Output Data Bit Rate	115.2 Kbaud
6DOF Data Update Rate	100 HZ
Data Latency	Between 7 and 30 msec
Optical Link Peak Wavelength	Between 880 and 940nm.
Optical Link Radiated Power	< 0.5 W
Optical Link Radiation Cone Angle	>= +/-45 deg
Optical Link Maximum Light Intensity	0.1 mW/cm ² at 1 m radius
Optical Link Carrier Frequencies	Between 400 KHz and 3 MHz

Table 2 Beacon controller specifications

Mass	< 1.5 Kg
Dimensions	< 10 x15 x15 cm
Electrical Power	< 0.4 A at +5 V (2 W) < 0.3 A at +12 V (3.6 W) < -0.3 A at -12 V (3.6 W) Total wattage <= 9.2W.

Table 3 Beacon specifications

Mass	< 0.75 Kg
Dimensions	< 8 x8 x4 cm
Electrical Power	< 0.8 A at +12 V (9.6 W)
Radiation Peak Wavelength	Between 880 and 940nm.
Radiated Power	< 0.9 W
Radiation Cone Angle	>= +/-50
Radiation Carrier Frequency	Between 30 KHz and 100 KHz
Maximum Light Intensity	1 mW/cm ² at 1 m radius
Maximum Light Radiant Intensity	10 W/sr

CHAPTER III

VISNAV SENSOR CALIBRATION

The ideal object to image space mapping of the optical sensor system is based on the perspective projection (the ideal pin-hole camera model), called the co-linearity equations in Eq. (2.5) and (2.6). The co-linearity equations represent the transformation between the object space coordinates and the corresponding ideal image coordinates. The VisNav camera's main optical properties are the intrinsic parameters describing the characteristics of the sensor assembly such as the lens' effective focal length and the optical center location. In addition, the extrinsic parameters, the relative position and attitude [17], [18] obviously affect the object to image space projection. However, all optical sensor systems have significant image distortion due to lens distortion, misalignment of sensor assembly, and related effects which induces departures from the ideal perspective projection [19]. Furthermore, the PSD used in the VisNav sensor system shows an unexpected non-linearity, especially near the edge of the field of view, that causes a serious deviation from the ideal pin-hole camera model. The VisNav system laboratory experimental data show that the measured sensor output voltages include significant amount of systematic distortion and shifting; these are a combination of optical and electronic non-linearity. Therefore, the VisNav sensor calibration process should correct all these deviations of the measured sensor output from the ideal pin-hole camera model before applying the navigation algorithm.

Traditionally, optical sensor calibration can be classified roughly into two categories: photogrammetric calibration and self-calibration [20]. Photogrammetric calibration is performed by observing a calibration object whose geometry in 3D space is known with very good precision and finding the distortion coefficients for the lens distortion model. On the other hand, self-calibration does not use any calibration object. Instead, by moving a camera in a static scene, the rigidity of the scene provides in

general two constraints on the cameras' intrinsic parameters from one camera displacement by using image information alone [21]. While the self-calibration is very flexible conceptually, it is very difficult to implement because there are too many parameters to estimate. So, practical self-calibration can consider only a simple low-dimensional distortion model. Tasi developed a self-calibration technique, determining the internal optical camera characteristics and 3D position and orientation of the camera frame relative to a reference coordinate system, considering also radial distortion [22].

However, for the VisNav system, it is necessary to capture the fine features of distortion to obtain the required high accuracy. Thus, more general and complicated nonlinear calibration models are needed instead of simple radial and decentering lens distortion model. VisNav calibration can be achieved based on optimal mapping techniques in the photogrammetric calibration sense. The VisNav sensor calibration is performed by observing calibration objects whose geometry in 3D space is known with very good precision. One way is to make many measurements and use direct interpolation of the calibration correction using a look-up table constructed from the experiment data set. Another way is to determine a best fitting calibration model which minimizes the re-projection errors of these calibration objects. The model based calibration is preferred to the interpolation because it can be determined consistent with a optimum least squares criterion, statistically consistent with measured precision and has proved more accurate and sufficiently fast to compute in real-time evaluation and has a smaller memory requirement.

3.1 Experimental Configuration

For VisNav sensor calibration, we first collect the extensive experimental data set using our laboratory calibration facility which consists of a high precision two axes Contraves air bearing table, capable of 1 arc second pointing with 360 degrees of yaw motion and 5 arc second pointing with +/- 50 degrees of pitch motion and mechanical positioning system.

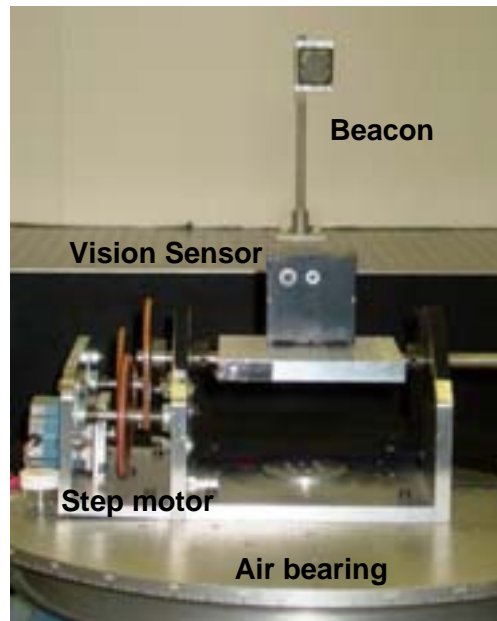


Figure 9 Experimental setup

The VisNav sensor is mounted on the two axes Contraves air bearing table and an beacon is mounted on the mechanical positioning system that gives the position information accurately. Figure 9 shows the experimental setup. As the sensor is rotated by known, commanded incremental angle about yaw and pitch axes, measurements with known relative position and attitude of the sensor can be obtained with an active beacon swept over the whole field-of-view of the sensor. These variations can be controlled by the calibration computer automatically, and over several hours, an extensive measured data set with corresponding known line-of-sight vectors from the VisNav sensor to the beacon can be collected. Unfortunately, we must accept the realistic uncertainty in the sensor position, attitude, and optical target location since we can only achieve certain levels of precision in the laboratory experiment.

First, the relative pitch angle is fixed at 0 degree and we sweep the yaw angle from -50 degree to +50 degree for a one dimensional test. This one dimensional test results shows the nonlinearity of the output voltages (Figure 10). Ideally, the only horizontal output voltage V_y should depend on the yaw angle and V_z should be zero. From the one

dimensional test with zero relative pitch angle, the optical center (offset) in voltage space can be determined as ($V_{yo} = 0.0004, V_{zo} = 0.0517$). The standard deviation of output voltages are shown in Figure 11. These were obtained by repeating each measurement 200 times and computing the statistics experimentally. It is clear that the standard deviations of output voltages near the optical center are smaller than those of far from the optical center. The degradation is approximately a factor of 3. The resulting position accuracy near the center of field of view is about one part in 2000, where it is about one part in 700 near the edge.

Figure 12 illustrates the relative target locations within the 90 degree field-of-view for the two dimensional calibration test. We consider the 6635 test points for our calibration process with 200 samples and averaged for each test point. Figure 13 represents the ideal locations according to the co-linearity equations of the light centroid corresponding to each calibration test point. The corresponding VisNav sensor voltage imbalance output in Figure 14 shows that the significant systematic distortion and offset in voltage space. In essence, the calibration process seeks the “map projection” functions that map from voltage space (V_y, V_z) into the corresponding ideal image coordinates (y, z) consistent with the co-linearity equations. Figure 15 and Figure 16 show that the standard deviation of samples for each test point. The standard deviation of output voltage signals indicates the signal to noise ratio. In addition, the standard deviation of V_y shows that the central area along the y-axis has smaller deviation, so more stable measurements can be given. Similarly, the central area along the z-axis of the standard deviation of V_z has smaller deviation.

The Root Mean Square (RMS) of standard deviation of V_y is 1.3916E-3 and RMS of standard deviation of V_z is 1.4842E-3. It is corresponding to signal to noise ratio of 1 part in 1000 for statistics over the active field of view, where the voltage signal range is -0.7 to 0.7. Therefore, the calibration process is expected to achieve the same level of accuracy.

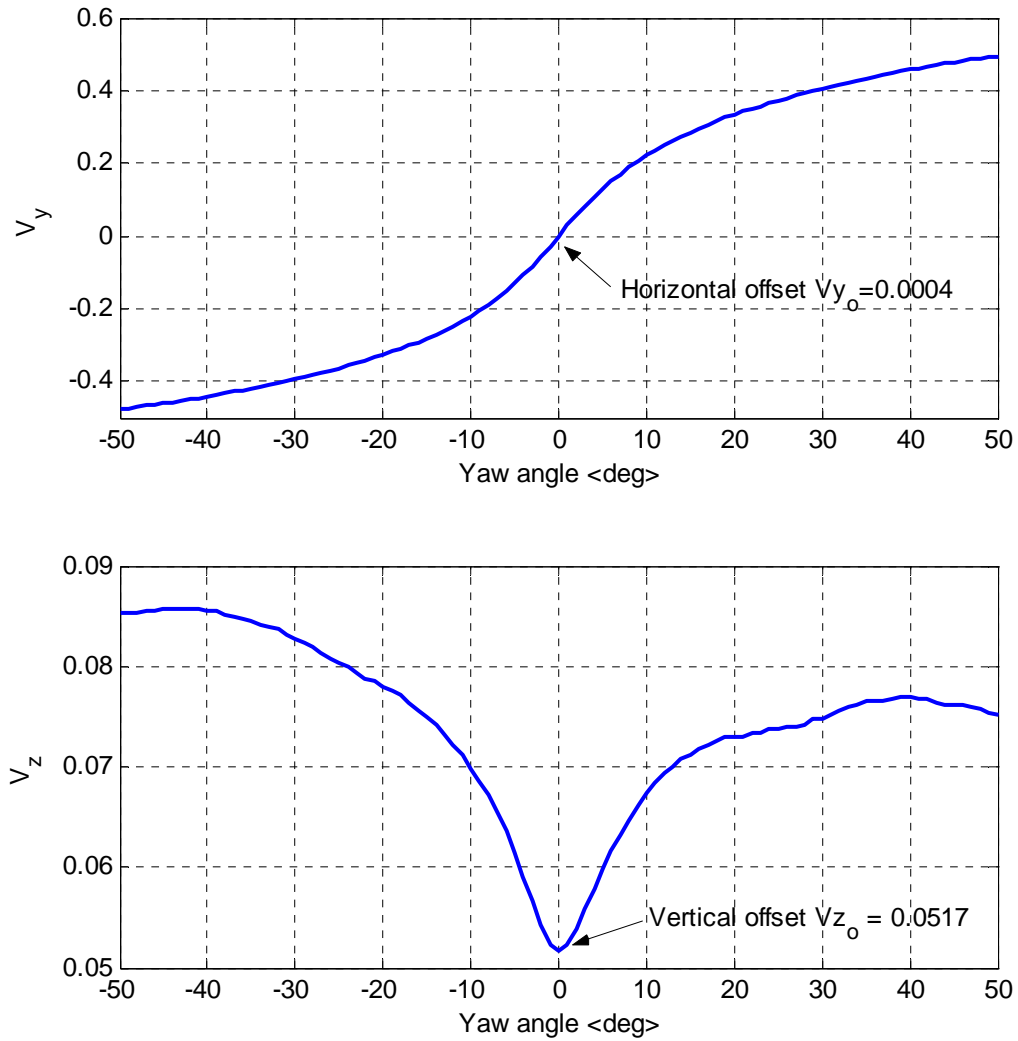


Figure 10 Nonlinearity of output voltages for the one dimensional test with fixed pitch angle = 0°

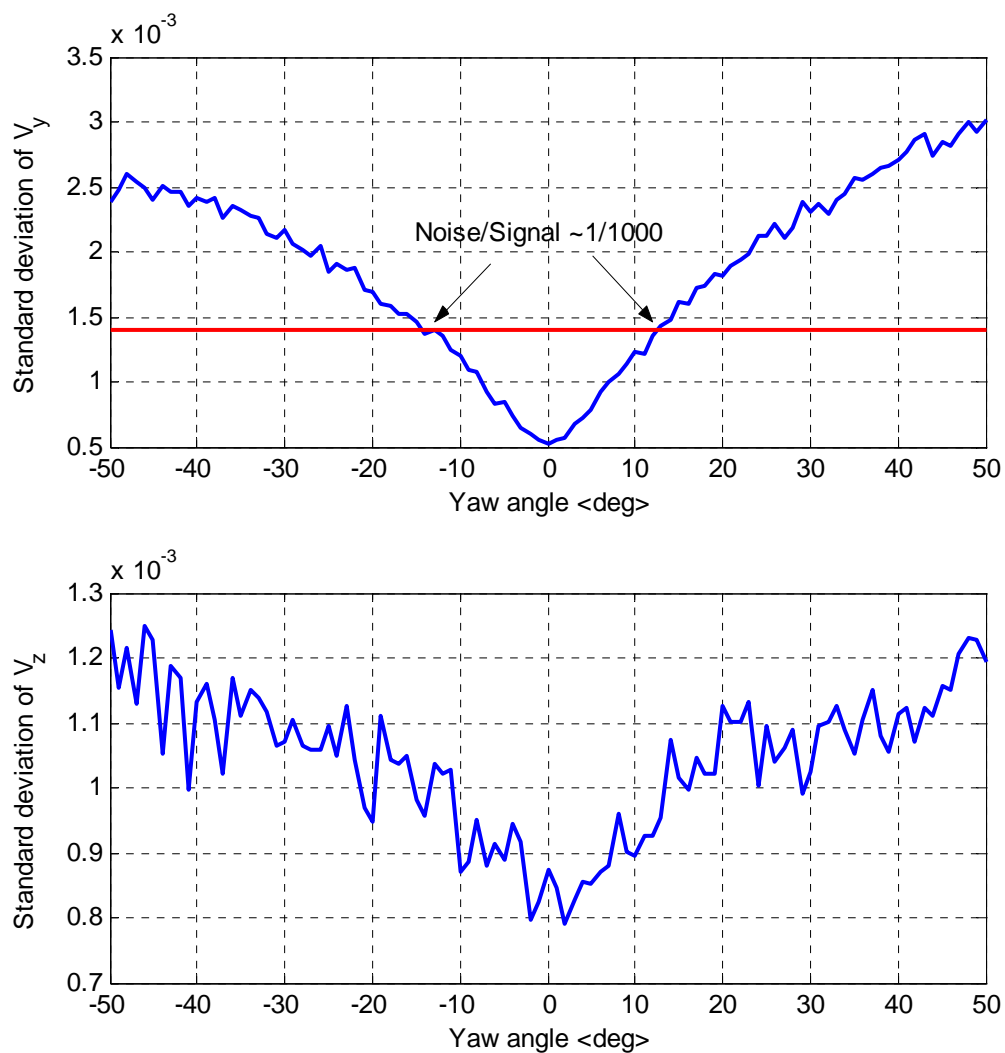


Figure 11 Standard deviation of output voltages for the one dimensional test with fixed pitch angle = 0°

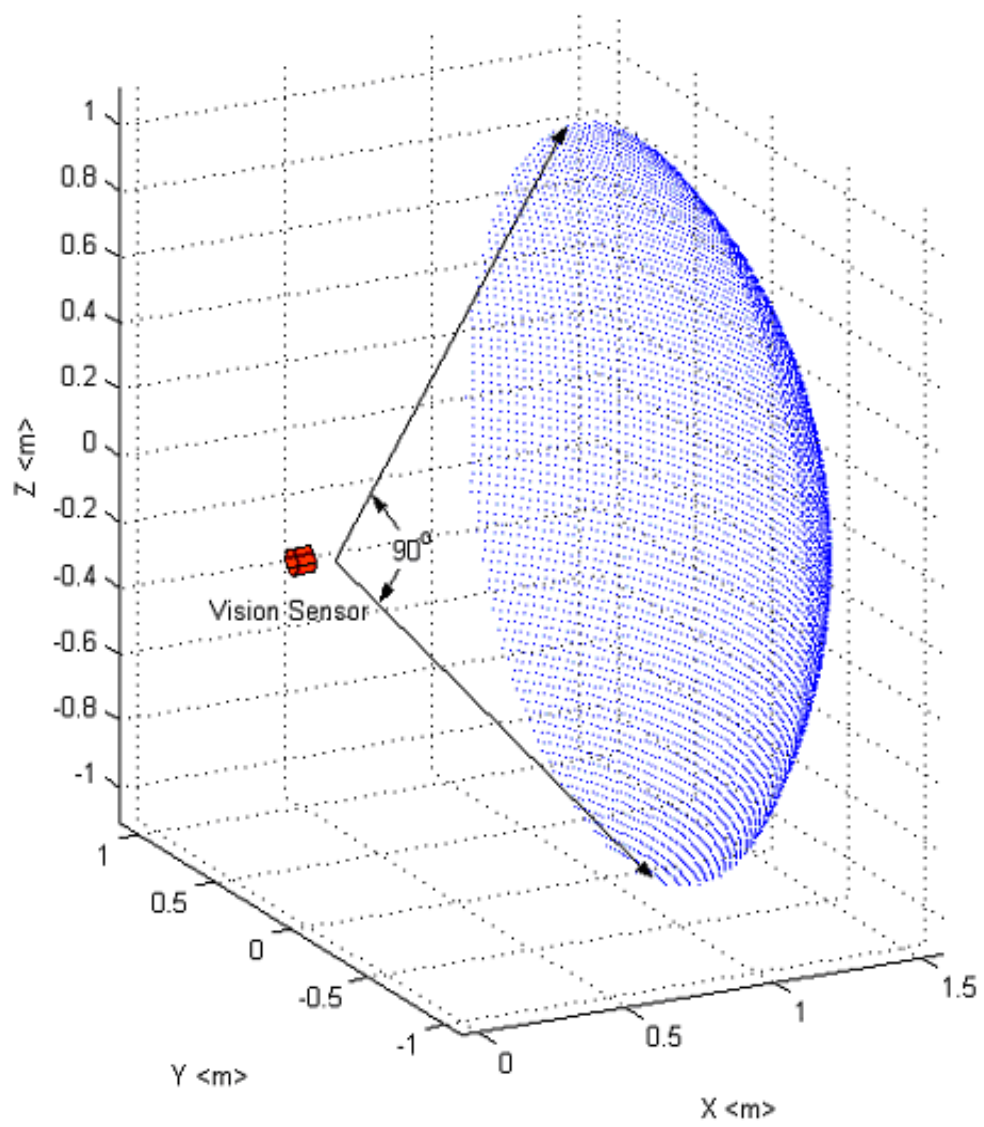


Figure 12 Relative target locations for calibration test

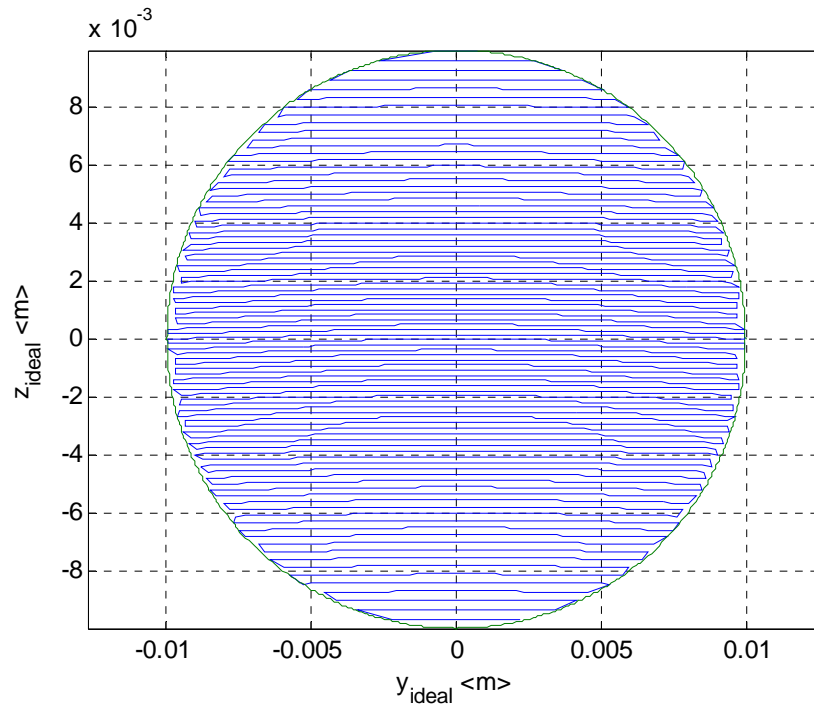


Figure 13 Ideal image coordinates, (y, z)

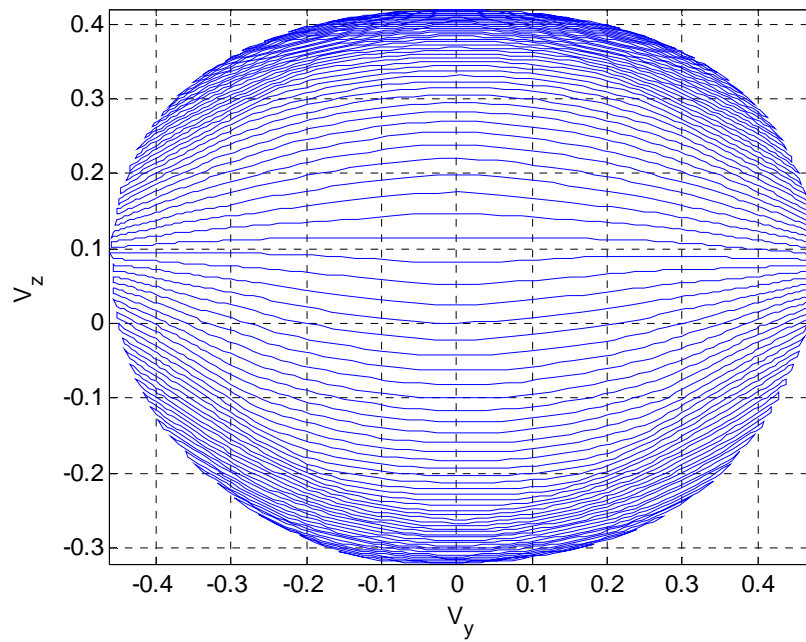


Figure 14 Actual VisNav sensor outputs, (V_y, V_z)

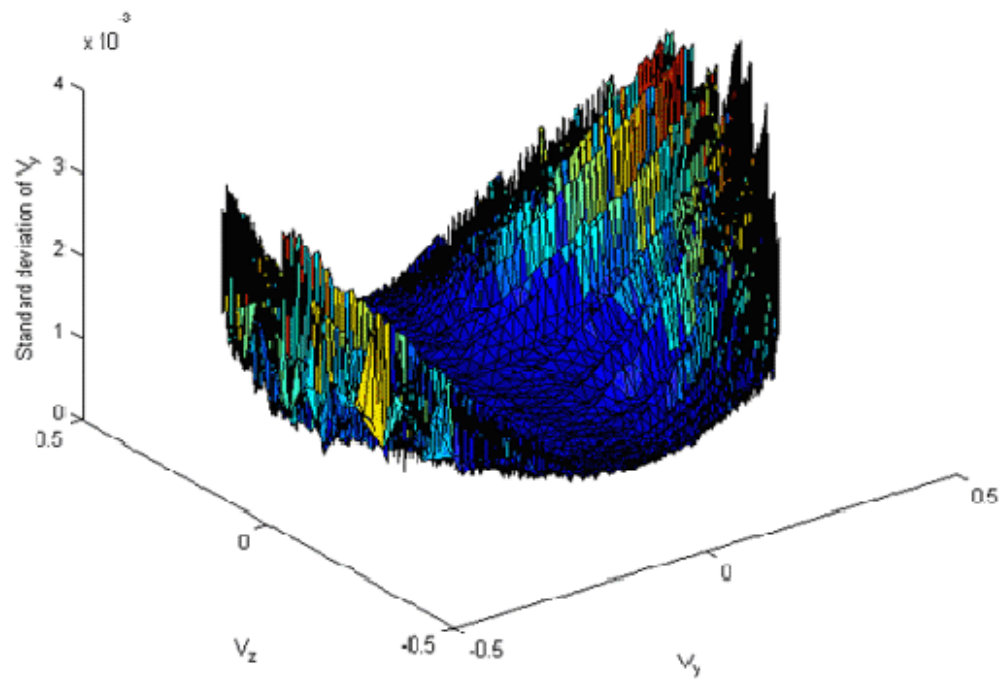


Figure 15 Standard deviation of V_y

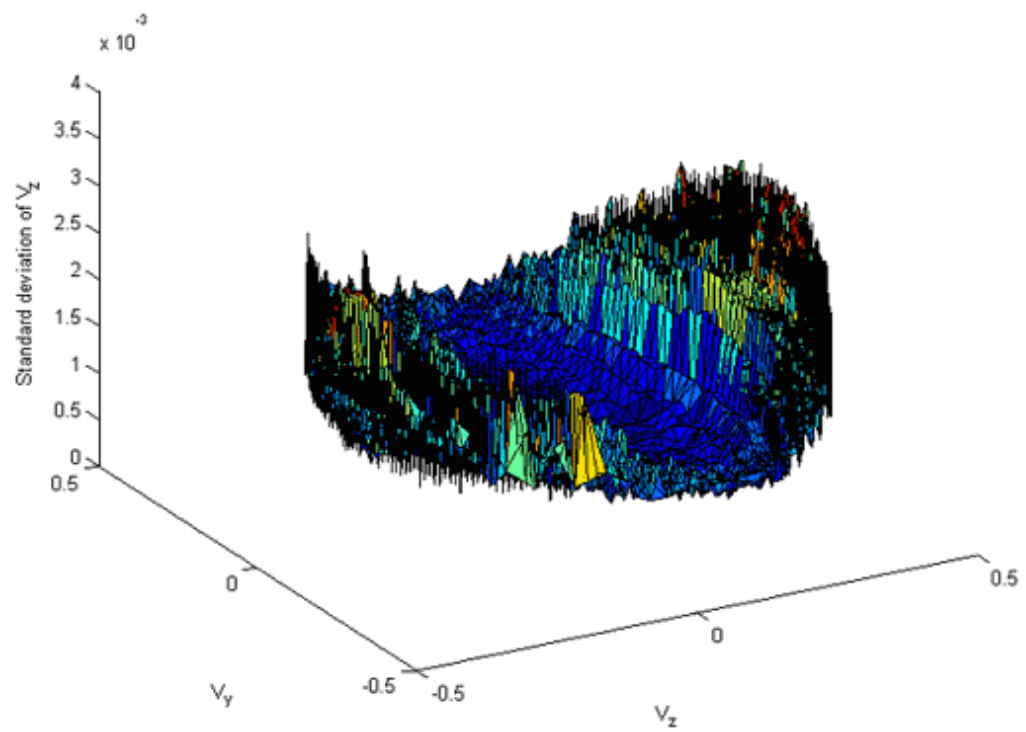


Figure 16 Standard deviation of V_z

3.2 Global Calibration

The main goal of the model based calibration is the optimal selection of a proper calibration model and determination of the best values of the unknown parameters to map the horizontal and vertical normalized voltage, (V_y, V_z) , which is the VisNav sensor output into the corresponding expected ideal image coordinates, (y, z) based on optimal estimation techniques.

3.2.1 Traditional Distortion Model

Traditionally, the simple radial, and decentering, and thin prism distortion models have been adopted for optical camera distortion model by the photogrammetric community [19]. Radial distortion is point-symmetric at the optical center of the lens and causes an inward or outward shift of image points from their initial perspective projection. The decentering distortion is induced by the misalignment of the optical centers of various lens elements in the sensor. It has both a radial and a tangential component. Thin prism distortion is introduced by manufacturing imperfections of lens elements and misalignment of sensor assembly from their ideal, perpendicular to the optical axis. Therefore, the traditional model can be parameterized with a complete set of basis functions to approximate lens distortion as:

$$\delta y = k_1 \bar{y} r^2 + k_2 \bar{y} r^4 + p_1 (3\bar{y}^2 + \bar{z}^2) + 2p_2 \bar{y} \bar{z} + q_1 r^2 \quad (3.1)$$

$$\delta z = k_1 \bar{z} r^2 + k_2 \bar{z} r^4 + 2p_1 \bar{y} \bar{z} + p_2 (\bar{y}^2 + 3\bar{z}^2) + q_2 r^2 \quad (3.2)$$

where, $r^2 = \bar{y}^2 + \bar{z}^2$ is the radial distance of image coordinates from the optical center, k_1, k_2 are radial distortion coefficients, P_1, P_2 are decentering distortion coefficients, and q_1, q_2 are the thin prism distortion coefficients. By the way, the calibration model should map the horizontal and vertical voltage into the ideal image coordinates. Thus \bar{y} and \bar{z} were replaced by \bar{y}' and \bar{z}' as following:

$$\hat{y} = \bar{y}' + \delta \bar{y}(\bar{y}', \bar{z}') \quad (3.3)$$

$$\hat{z} = \bar{z}' + \delta \bar{z}(\bar{y}', \bar{z}') \quad (3.4)$$

where \bar{y}' and \bar{z}' defined as linearly related to normalized voltages with scaling factor f_y and f_z as following:

$$\bar{y}' = f_y \bar{V}_y \quad (3.5)$$

$$\bar{z}' = f_z \bar{V}_z \quad (3.6)$$

Intuitively, this linear relationship is expected for ideal VisNav sensor which free from the distortion.

However, these traditional radial, decentering, and thin prism distortion models have been found to be inadequate to account for the deviations induced by the VisNav sensor which introduce significant amounts of image distortion which is combined the effect of lens distortion with the effect of PSD non-linearity. Overall calibration accuracy is corresponding to one part in 100 of the VisNav sensor field-of-view. It doesn't satisfy the expected VisNav system accuracy from experimental results.

3.2.2 Bivariate Polynomial Model

The VisNav system requires more general and complex nonlinear calibration model structure which can capture the fine features of distortion to obtain the required high accuracy and then determine the optimal set of calibration coefficients based on the least square criterion. First we define a nonlinear calibration model as bivariate vector functions which are combination of adequate basis:

$$\hat{y} = \sum_{i=0}^n \sum_{j=0}^i a_{ij} \Phi_{ij}(V_y, V_z) \quad (3.7)$$

$$\hat{z} = \sum_{i=0}^n \sum_{j=0}^i b_{ij} \Phi_{ij}(V_y, V_z) \quad (3.8)$$

where n is the order of the polynomial basis, $\Phi_{ij}(V_y, V_z)$ are the bivariate polynomial basis of calibration function, and \hat{y} and \hat{z} are calibrated image coordinates which is

already compensated optical center (y_o, z_o) . There are many choices for the basis function such as regular polynomial, Fourier series and radial basis function, etc. The Chebyshev polynomial is an excellent choice for the calibration functions due to recursive properties and broad acceptance in approximation.

The first type chebyshev polynomial is defined as following:

$$T_n(x) = \cos n\theta, \quad \cos \theta = x \quad (3.9)$$

Note that the input variable of the Chebyshev polynomials should be in the interval $[-1, 1]$ by the definition. Then the univariate first type Chebyshev polynomial is defined by following recursion by applying the trigonometric identity [23]

$$T_{n+1}(x) = 2xT_n(x) - T_{n-1}(x) \quad (3.10)$$

where $T_0(x) = 1$ and $T_1(x) = x$. Thus, the bivariate polynomial basis is defined by the following combination of Chebyshev polynomial (Figure 17)

$$\Phi_{ij}(V_y, V_z) = T_{i-j}(V_y)T_j(V_z) \quad (3.11)$$

Finally, the nonlinear bivariate calibration function model is defined by

$$\begin{aligned} \hat{y} &= \sum_{i=0}^n \sum_{j=0}^i a_{ij} \Phi_{ij}(V_y, V_z) = \sum_{i=0}^n \sum_{j=0}^i a_{ij} T_{i-j}(V_y) T_j(V_z) \\ &= a_{00} + a_{10}T_1(V_y) + a_{11}T_1(V_z) \\ &\quad + a_{20}T_2(V_y) + a_{21}T_1(V_y)T_1(V_z) + a_{22}T_2(V_z) \\ &\quad + a_{30}T_3(V_y) + a_{31}T_2(V_y)T_1(V_z) + a_{32}T_1(V_y)T_2(V_z) + a_{33}T_3(V_z) \\ &\quad \vdots \\ &\quad + a_{n0}T_n(V_y) + a_{n1}T_{n-1}(V_y)T_1(V_z) + \cdots + a_{nm-1}T_1(V_y)T_{n-1}(V_z) + a_{nn}T_n(V_z) \end{aligned} \quad (3.12)$$

$$\begin{aligned} \hat{z} &= \sum_{i=0}^n \sum_{j=0}^i b_{ij} \Phi_{ij}(V_y, V_z) = \sum_{i=0}^n \sum_{j=0}^i b_{ij} T_{i-j}(V_y) T_j(V_z) \\ &= b_{00} + b_{10}T_1(V_y) + b_{11}T_1(V_z) \\ &\quad + b_{20}T_2(V_y) + b_{21}T_1(V_y)T_1(V_z) + b_{22}T_2(V_z) \\ &\quad + b_{30}T_3(V_y) + b_{31}T_2(V_y)T_1(V_z) + b_{32}T_1(V_y)T_2(V_z) + b_{33}T_3(V_z) \\ &\quad \vdots \\ &\quad + b_{n0}T_n(V_y) + b_{n1}T_{n-1}(V_y)T_1(V_z) + \cdots + b_{nm-1}T_1(V_y)T_{n-1}(V_z) + b_{nn}T_n(V_z) \end{aligned} \quad (3.13)$$

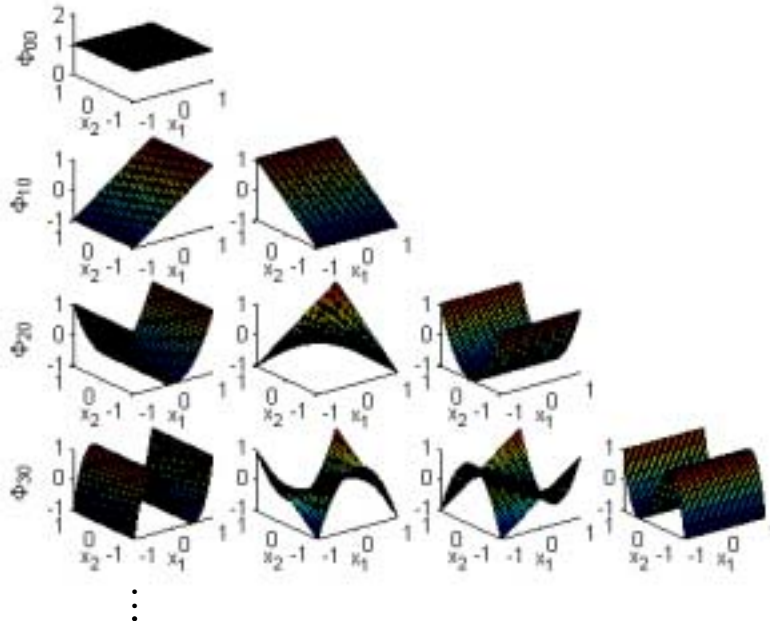


Figure 17 Bivariate basis functions

The total number of coefficients for each n^{th} order calibration function is $(n+1)(n+2)/2$. Then, our goal is to determine the two set of optimal calibration coefficient vector \mathbf{a} and \mathbf{b} . Various optimization methods may be applied to determine the optimal coefficients. For our purpose, we adopt a least squares approach to find the optimal coefficients such that minimize the sum square of the residual errors given by:

$$\begin{aligned}
 J_y &= \frac{1}{2} \sum_{i=1}^m w_i (g_{y,i} - \hat{y}_i)^2 = \frac{1}{2} (\mathbf{g}_y - H\mathbf{a})^T W (\mathbf{g}_y - H\mathbf{a}) \\
 J_z &= \frac{1}{2} \sum_{i=1}^m w_i (g_{z,i} - \hat{z}_i)^2 = \frac{1}{2} (\mathbf{g}_z - H\mathbf{b})^T W (\mathbf{g}_z - H\mathbf{b})
 \end{aligned} \tag{3.14}$$

where $\mathbf{g}_y, \mathbf{g}_z$ are column vector form of the ideal image coordinates of the given set of calibration points, $W = W^T > 0$ is the weight matrix, m is the total number of calibration points, and least-squares matrix H is expressed as:

$$H = \begin{bmatrix} \Phi_{00}(V_{y,1}, V_{z,1}), \Phi_{10}(V_{y,1}, V_{z,1}), \Phi_{11}(V_{y,1}, V_{z,1}), \Phi_{20}(V_{y,1}, V_{z,1}), \dots, \Phi_m(V_{y,1}, V_{z,1}) \\ \Phi_{00}(V_{y,2}, V_{z,2}), \Phi_{10}(V_{y,2}, V_{z,2}), \Phi_{11}(V_{y,2}, V_{z,2}), \Phi_{20}(V_{y,2}, V_{z,2}), \dots, \Phi_m(V_{y,2}, V_{z,2}) \\ \vdots \\ \Phi_{00}(V_{y,m}, V_{z,m}), \Phi_{10}(V_{y,m}, V_{z,m}), \Phi_{11}(V_{y,m}, V_{z,m}), \Phi_{20}(V_{y,m}, V_{z,m}), \dots, \Phi_m(V_{y,m}, V_{z,m}) \end{bmatrix} \quad (3.15)$$

The coefficients \mathbf{a} and \mathbf{b} are should minimize the quadratic function J_y and J_z . Thus Jacobian of J_y and J_z with respect to \mathbf{a} and \mathbf{b} should be zero.

$$\begin{aligned} \nabla_{\mathbf{a}} J_y &= H^T W H \mathbf{a} - H^T W \mathbf{g}_y = 0 \\ \nabla_{\mathbf{b}} J_z &= H^T W H \mathbf{b} - H^T W \mathbf{g}_z = 0 \end{aligned} \quad (3.16)$$

Consequently, the best calibration coefficients are given by:

$$\begin{aligned} \hat{\mathbf{a}} &= (H^T W H)^{-1} H^T W \mathbf{g}_y \\ \hat{\mathbf{b}} &= (H^T W H)^{-1} H^T W \mathbf{g}_z \end{aligned} \quad (3.17)$$

We use Singular Value Decomposition (SVD) to avoid the matrix inversion. SVD decomposes a matrix into a diagonal matrix and two orthogonal matrices:

$$(H^T W H) = U S V^T \quad (3.18)$$

where U is the $m \times (n+1)(n+2)/2$ matrix with orthogonal columns such that satisfies $U^T U = I$, S is an $(n+1)(n+2)/2 \times (n+1)(n+2)/2$ diagonal matrix, and V is an orthogonal matrix such that satisfies $V^T V = I$. Then

$$(H^T W H)^{-1} = V S^{-1} U^T \quad (3.19)$$

Another computationally efficient way to determine the coefficients \mathbf{a} and \mathbf{b} can be erived from rearranging the matrices as following:

$$\begin{aligned} W &= W^{1/2} W^{1/2}, \quad \bar{H} \equiv W^{1/2} H \\ \bar{\mathbf{g}}_y &\equiv W^{1/2} \mathbf{g}_y, \quad \bar{\mathbf{g}}_z \equiv W^{1/2} \mathbf{g}_z \end{aligned} \quad (3.20)$$

then the best calibration coefficients are given by:

$$\begin{aligned}\hat{\mathbf{a}} &= (\bar{H}^T \bar{H})^{-1} \bar{H} \bar{\mathbf{g}}_y \\ \hat{\mathbf{b}} &= (\bar{H}^T \bar{H})^{-1} \bar{H} \bar{\mathbf{g}}_z\end{aligned}\tag{3.21}$$

It is also true that the SVD of \bar{H} not $\bar{H}^T \bar{H}$ gives a more numerically well behaved solution for \mathbf{a} and \mathbf{b} .

In the case of the polynomials model based calibration, an optimization was run to determine which order is adequate for the mapping. The order of polynomial basis varying from 5 to 30 was tested for global calibration function, and each time the Standard deviation of calibration errors of the validation points within the 90 degree field-of-view was evaluated. Figure 18 and Figure 19 show that the calibration accuracy of global calibration functions as the order of Chebyshev polynomial basis. Consequently, $n = 25$ was found to be an adequate order of Chebyshev polynomial where the required number of coefficient for each axis is 702. Therefore 1404 coefficients are required for 25th Chebyshev polynomial based calibration functions.

Overall calibration accuracy of 25th Chebyshev polynomial based calibrations is corresponding to one part in 900 of the VisNav sensor field-of-view. Figure 20 and Figure 21 show that the calibration errors of global mapping using 25th Chebyshev polynomial. However, the calibration errors of the 25th global mapping using Chebyshev polynomial basis (Figure 20 Figure 21) are still show that the remaining significant systematic errors in the central region of PSD which is expected to very precise measurement. These systematic calibration errors can not be corrected using the global calibration function even though the order of polynomial basis becomes larger. The high order of polynomial basis leads high oscillations of the approximated surface so that it causes systematic errors. The qualitative criterion for truncation is to determine the lowest degree of polynomial that has residual statistics with a standard deviation equal to the measurement error.

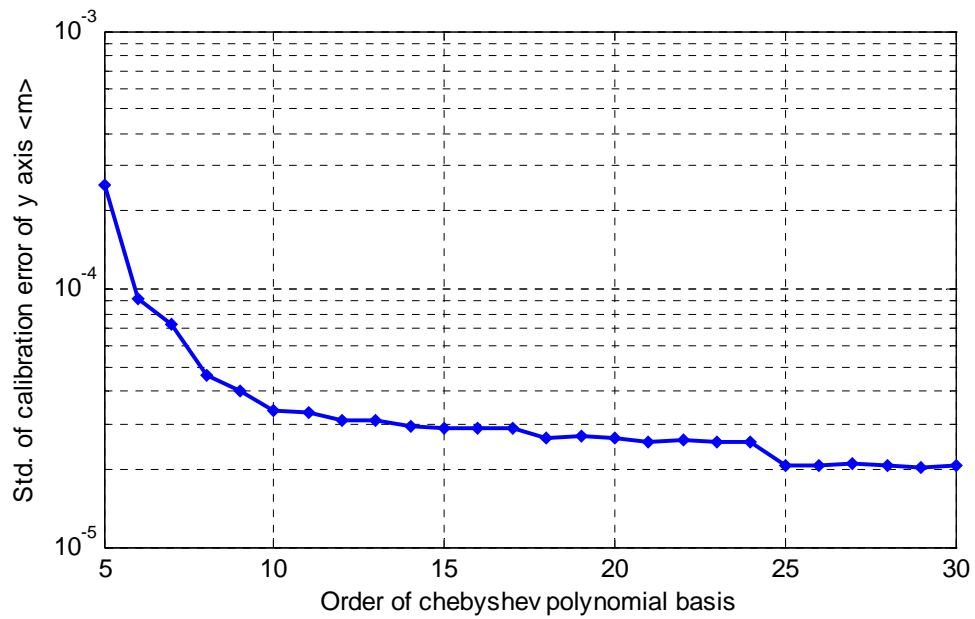


Figure 18 Order of polynomial basis vs y calibration accuracy

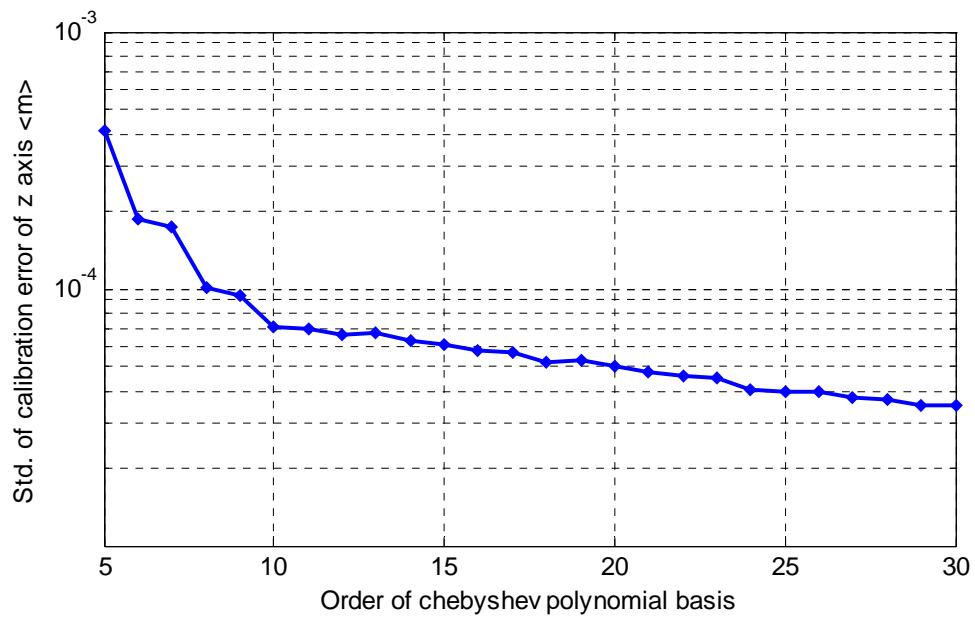


Figure 19 Order of polynomial basis vs. z calibration accuracy

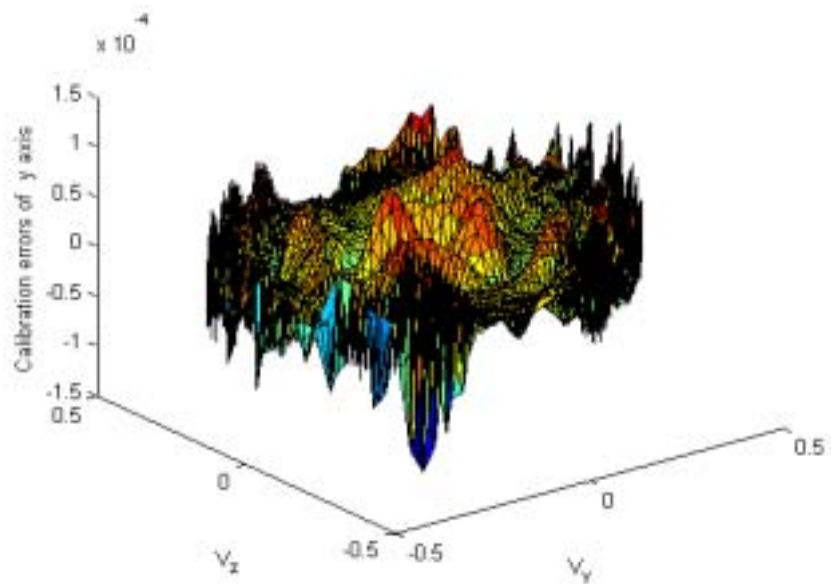


Figure 20 y axis calibration errors of 25th order Chebyshev polynomial calibration function

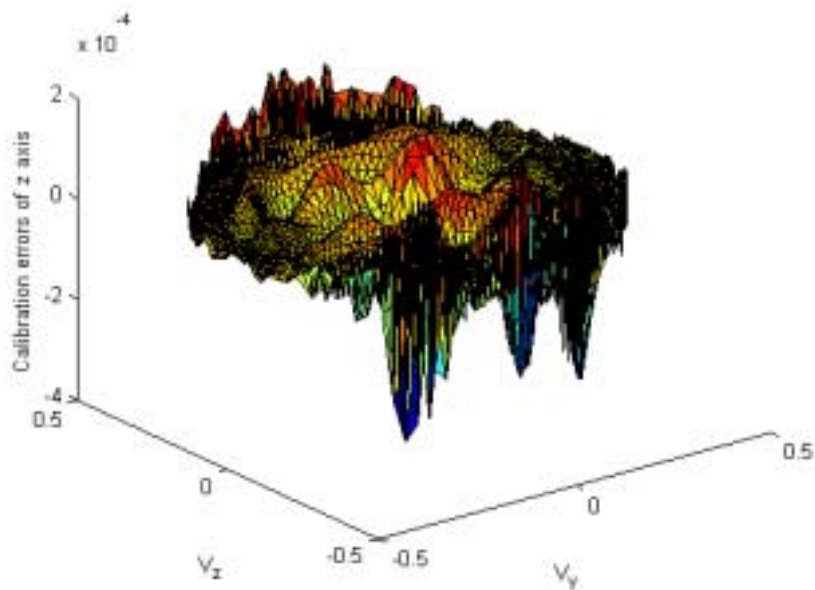


Figure 21 z axis calibration errors of 25th order Chebyshev polynomial calibration function

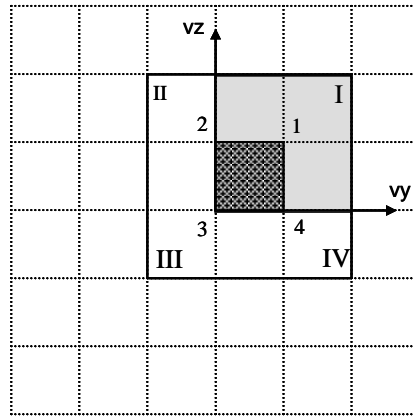


Figure 22 Local surface averaging

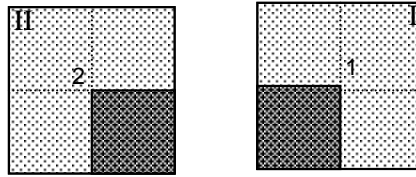
3.3 Weighted Averaging Method

The irregular surface modeling technique [24] based on the weighted averaging of locally approximated surfaces is a promising solution for fine-structure surface modeling with large observation data sets. For this purpose, consider the determination of a local preliminary surface functions and then determine the final local surface function by combining the four overlapping preliminary surface using appropriate weighting function. Figure 22 shows the local surface averaging concept.

The input variables are segmented by a number of grids and arranged to unit square cells, (v_y, v_z) by linear scaling. Four preliminary surfaces to approximate $x(v_y, v_z)$ are determined for 2 by 2 cell unit using low degree polynomial of two variables; $x_1(v_y, v_z)$, $x_2(v_y, v_z)$, $x_3(v_y, v_z)$, and $x_4(v_y, v_z)$ are assumed to be some arbitrary approximation functions. For several computational advantages, bivariate Chebyshev polynomials can be chosen. Then each preliminary surface functions can be determined by the Gaussian least squares sense with low degree basis functions.

The centroid of each preliminary surface is a 'mesh point', a mutual corner of four final surface functions. Thus the final surface function, valid above the central shared square is determined as the weighted average of four preliminary surfaces in Figure 23.

$x_2(v_y, v_z)$ valid over $x_1(y_y, v_z)$ valid over



$x_3(v_y, v_z)$ valid over $x_4(v_y, v_z)$ valid over

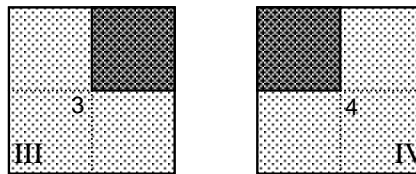


Figure 23 Four preliminary surfaces

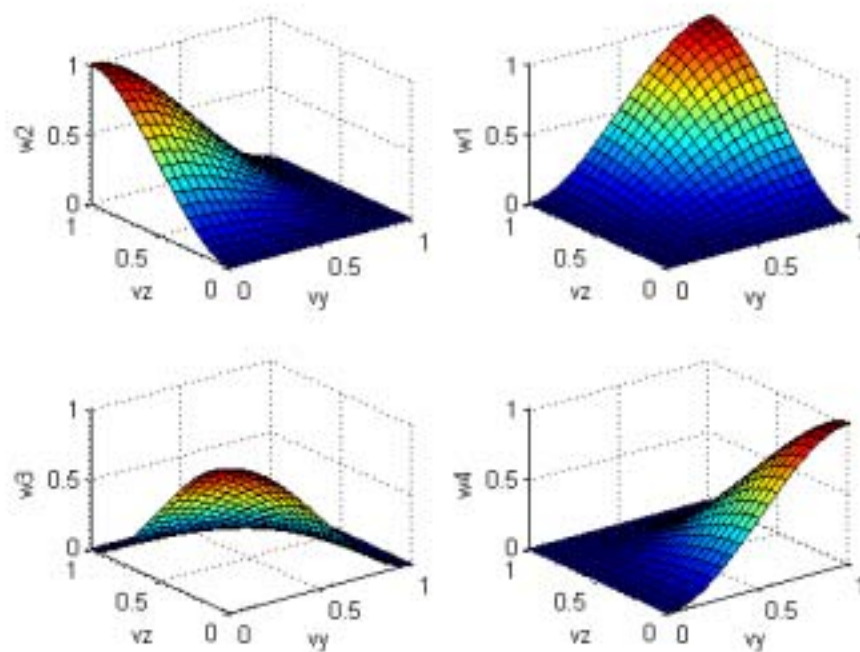


Figure 24 Weighting functions

$$x(v_y, v_z) = \sum_{i=1}^4 w_i(v_y, v_z) x_i(v_y, v_z) \quad (3.22)$$

where $w_i(v_y, v_z)$ are weighing function which can be determined in such a fashion that the continuity is ensured everywhere along mutual boundaries of adjacent final surface functions. In other word, the final surface functions osculate with the respective preliminary surfaces centered at its four corners. Also, along a typical boundary the final surface and its partial derivatives are taken to be a weighted average of only the two preliminary surfaces centered at the end points of that boundary. This constraint leads to global piecewise continuity. We must choose the adequate weighting function that satisfies the boundary condition and the normality constraint of the weighting function:

$$\sum_{i=1}^4 w_i(v_y, v_z) = 1 \quad (3.23)$$

The result weight functions have been found to be:

$$\begin{aligned} w_1 &= v_y^2 v_z^2 (3 - 2v_y)(3 - 2v_z), \\ w_2 &= w_1(1 - v_y, v_z), \\ w_3 &= w_1(1 - v_y, 1 - v_z), \\ w_4 &= w_1(v_y, 1 - v_z) \end{aligned} \quad (3.24)$$

Each of these weight functions looks like a quadrant of a bell-shaped function having a square base (Figure 24). Finally, the method sequentially operates on a moderate to small subset of the measured data. It is therefore applicable to an arbitrarily large set of observed data. However, the final surface functions of the form of Eq. (3.22) cannot be determined above a border of the observed data set owing to the required overlap pattern.

3.4 Two Step Calibration Process

The global calibration function performs the transformation the actual VisNav sensor output voltages to the expected ideal image coordinates. The global mapping can not capture the systematic distortion errors even though sufficiently high order of

polynomial basis in the central region of PSD especially. On the other hand, weighted averaging method of locally valid calibration model can capture the fine structure of the object surface except the border of the observed data set. Thus, two step calibration method has been developed. For two step calibration, 25th Chebyshev polynomial based calibration functions are determined at first and calculate the residual errors $\Delta\bar{y}$ and $\Delta\bar{z}$ of the 25th Chebyshev polynomial based calibration. And then determined the locally valid compensation functions which are fitting the remaining residuals surfaces of 25th Chebyshev polynomial based calibration. The locally valid compensation functions are defined by weighted averaging method in Eq. (3.22):

$$\Delta\hat{y}(v_y, v_z) = \sum_{i=1}^4 w_i(v_y, v_z) \Delta\bar{y}_i(v_y, v_z) \quad (3.25)$$

$$\Delta\hat{z}(v_y, v_z) = \sum_{i=1}^4 w_i(v_y, v_z) \Delta\bar{z}_i(v_y, v_z) \quad (3.26)$$

where v_y and v_z are the re-scaled value into unit square cell of input variable V_y and V_z .

We segmented the input variables into 144 grid cells and chose the 3rd order of bivariate Chebyshev polynomials as preliminary surface functions. Then 1728 number of coefficients is required for locally valied compensation functions. Figure 25 and Figure 26 show that the calibration accuracy of two step calibration. They clearly show that the systematic distortion is corrected.

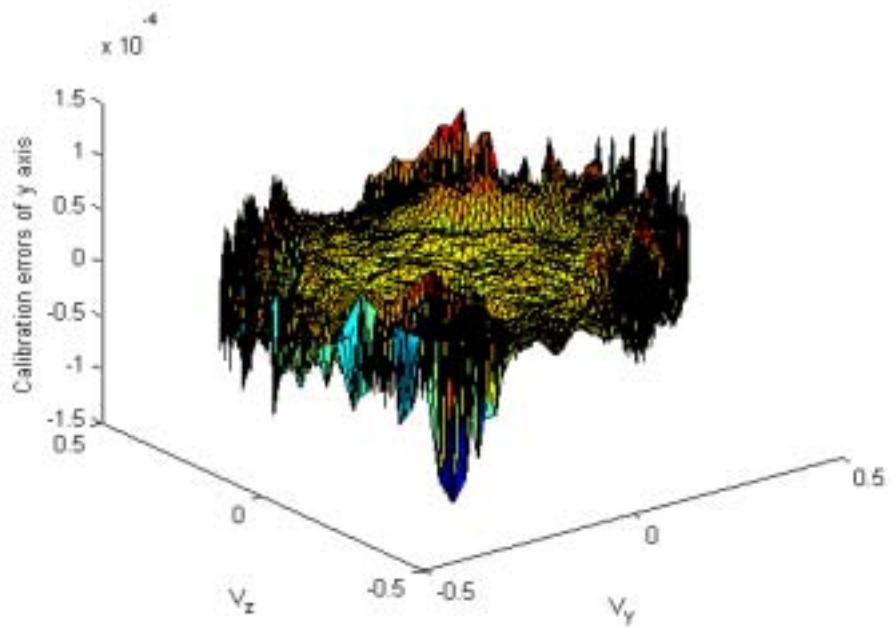


Figure 25 y axis calibration errors of two step calibration function

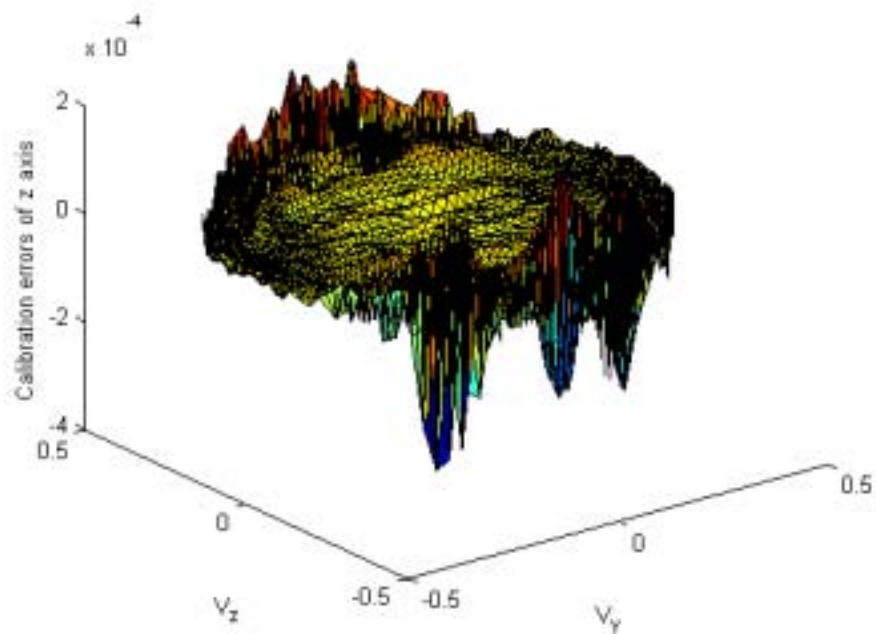


Figure 26 z axis calibration errors of two step calibration function

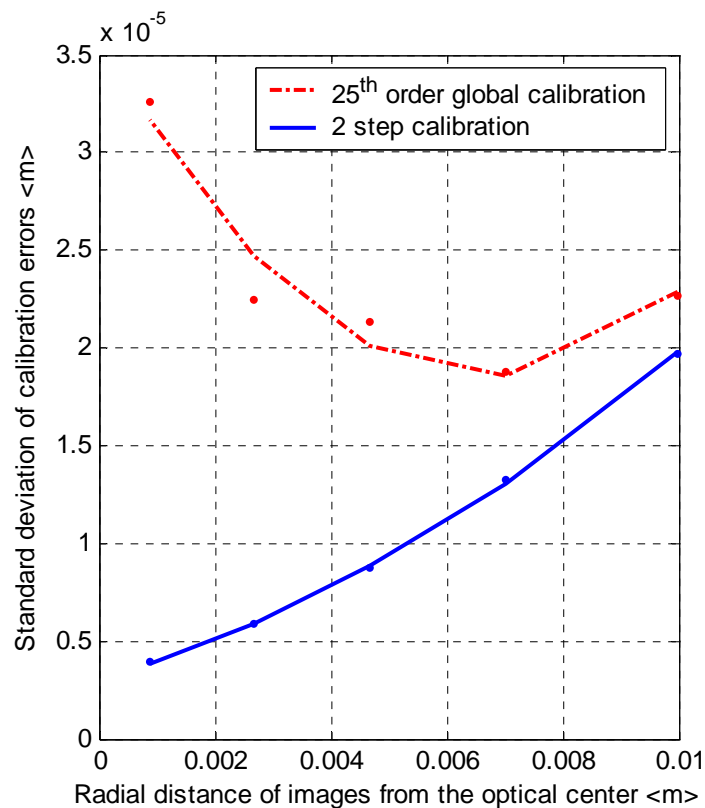


Figure 27 Radial distance of calibrated images vs standard deviation of calibration errors

3.5 Calibration Summary

The VisNav system is based on photogrammetric triangulation. More specifically, the process is known as “resection” whereby the question is answered “from what position and attitude was this photograph taken?” The non-ideal departures from the pin-hole camera model degrade the accuracy of the navigation solution. Therefore, the proposed calibration process is crucial task to determine the navigation solution. Figure 27 shows the 25th order global calibration accuracy and two step calibration accuracy. Notice, comparing Figure 11 and Figure 27, the accuracy of the two step process is consistent with the PSD centroidiry accuracy. The two step calibration achieved a better accuracy and successfully captured the systematic errors shown at the central region of

global calibration. However, note that the two step calibration requires huge memory space to store the global and local calibration coefficients. The total number of coefficients of 25th global calibration function of y and z axis is 702 and the total number of coefficients of local calibration functions 1728. Therefore, the total number of coefficients of two 2 calibration is 2430. The current experiment and calibration process shows that calibration results show high dependence upon the radial distance of calibrated images from the optical center. Therefore, it is required to approximate the expected standard deviation according to the radial distance of calibrated images in order to determine the weight of each measurement from the VisNav sensor measurements. The 2nd order approximation gives the following relationships

$$\sigma(r) = 3.0 \times 10^{-6} + 8.8 \times 10^{-3} r + 8.0 \times 10^{-2} r^2 \quad (3.27)$$

where r is the radial distance of calibrated image from the optical center. The approximated standard deviations of 25th global calibration and two step calibration methods are shown in Figure 27. At the boundary of 90 degrees field-of-view, the calibration accuracy can be determined with an accuracy of about 2.0×10^{-5} meters. It is corresponding to one part in 1000 of the VisNav sensor field of view angle.

However, the lens barrel distortion is expected to vary with the range between the VisNav sensor and optical target [25]. Especially, when the lens diameter is not negligible compared to the range i.e. largest variations from the pin-hole model near the sensor, receding to some asymptotic behavior for large distance. For the attainment of the high accuracy, it is necessary to account for the variation of lens distortion according to the range. However, it is not convenient and judged to be too complicated to determine the calibration function including the range dependence. One practical way suggested is to interpolate the evaluated values from reference sets of calibration functions determined at fixed ranges and thus indirectly capture the range dependence.

CHAPTER IV

RELATIVE POSITION AND ATTITUDE ESTIMATION

The VisNav sensor provides line-of-sight vector measurements with about one part in 1000 accuracy, after applying the calibration process discussed in Chapter III. These line-of-sight measurements should be used to estimate the six degree-of-freedom relative position and attitude the image space coordinate frame with respect to the object space coordinate frame fixed on the target vehicle.

The approach used for six degree of freedom navigation using line-of-sight vector measurements is the optimal inversion of the object to image projective transformation, modeled by the co-linearity equations in Eq. (2.5) and (2.6) [10].

Attitude determination from line of sight vector measurements commonly finds a proper orthogonal matrix that minimizes the cost function

$$L(A) = \frac{1}{2} \sum_{k=1}^N a_k \left| \hat{\mathbf{W}}_k - A \hat{\mathbf{V}}_k \right|^2 \quad (4.1)$$

where $\hat{\mathbf{W}}_k$, $k=1, \dots, N$ are a set of unit vector observations in the body frame, and $\hat{\mathbf{V}}_k$, $k=1, \dots, n$, are the representations of the same unit vectors with respect to the reference frame. This minimization problem is frequently referred as the Wahba's problem [26]. The a_k are a set of positive weights. Provided that at least two of the line-of-sight vector measurements are not parallel, a unique minimizing attitude matrix can always be determined. The TRIAD and QUEST algorithms to determine the three axis attitude from the line-of-sight vector measurements have been studied and shown to be very efficient [27].

Position determination can also be accomplished from the line-of-sight vector measurements based on triangulation from known reference base points. If the attitude is

known, then at least two non-colinear line of sight vector measurements are required to establish a three-dimensional position.

However, determining both attitude and position is more complex because the collinearity equation is highly nonlinear and there are six unknowns. At least four non-collinear line of sight vector measurements are required to uniquely solve the six degree of freedom navigation problems [28]. The determination of the position and attitude using line-of-sight vector measurements is a non-linear multi-variable optimization problem. To solve the problem, Junkins, Hughes et al, have developed the Gaussian Least Squares Differential Correction (GLSDC) using the Euler angle attitude parameters [10].

4.1 Attitude Parameterization

Attitude parameters are sets of coordinates that completely describe the orientation of a rigid body relative to some reference frame. There are an infinite number of attitude parameters to choose from. A good choice for attitude coordinates can greatly simplify the mathematics and avoid such pitfalls as mathematical and geometrical singularities or highly nonlinear kinematic differential equations [29], [30].

The direction cosine matrix written in terms of $3(\psi) - 2(\theta) - 1(\phi)$ sequence Euler angle is given by

$$A = \begin{bmatrix} \cos\theta\cos\psi & \cos\theta\sin\psi & -\sin\theta \\ \sin\phi\sin\theta\cos\psi - \cos\phi\sin\psi & \sin\phi\sin\theta\sin\psi + \cos\theta\cos\psi & \sin\phi\cos\theta \\ \cos\phi\sin\theta\cos\psi + \sin\phi\sin\psi & \cos\phi\sin\theta\sin\psi - \sin\theta\cos\psi & \cos\phi\cos\theta \end{bmatrix} \quad (4.2)$$

and the corresponding kinematic differential equation is

$$\begin{pmatrix} \dot{\psi} \\ \dot{\theta} \\ \dot{\phi} \end{pmatrix} = \frac{1}{\cos\theta} \begin{bmatrix} 0 & \sin\psi & \cos\psi \\ 0 & \cos\psi\cos\theta & -\sin\psi\cos\theta \\ \cos\theta & \sin\psi\sin\theta & \cos\psi\sin\theta \end{bmatrix} \begin{pmatrix} \omega_1 \\ \omega_2 \\ \omega_3 \end{pmatrix} \quad (4.3)$$

The Euler angle attitude parameterization is not a good choice for large angle displacements even though it gives an intuitive understanding of the attitude, since it has a singularity at $\theta = \pm 90$ degrees and behaves in a nonlinear fashion in kinematics.

Quaternion representation is the most commonly used attitude parameters owing to nonsingular attitude description. The Quaternion, $\{q_1, q_2, q_3, q_4\}$ used to represent finite rotations are defined by [29]

$$\mathbf{q} = \begin{bmatrix} \mathbf{q}_{13} \\ q_4 \end{bmatrix} \quad (4.4)$$

with the vector part of the Quaternion is related to the principal rotation direction $\hat{\mathbf{e}} = [e_1, e_2, e_3]^T$

$$\mathbf{q}_{13} = \begin{bmatrix} q_1 \\ q_2 \\ q_3 \end{bmatrix} = \hat{\mathbf{e}} \sin(\Phi / 2) \quad (4.5)$$

and the scalar part of the Quaternion is defined by principal rotation angle Φ

$$q_4 = \cos(\Phi / 2) \quad (4.6)$$

The direction cosine matrix can be written in terms of the quaternion as

$$A = \begin{bmatrix} q_4^2 + q_1^2 - q_2^2 - q_3^2 & 2(q_1q_2 + q_0q_3) & 2(q_1q_3 - q_0q_2) \\ 2(q_1q_2 - q_0q_3) & q_4^2 - q_1^2 + q_2^2 - q_3^2 & 2(q_2q_3 + q_0q_1) \\ 2(q_1q_3 + q_0q_2) & 2(q_2q_3 - q_0q_1) & q_4^2 - q_1^2 - q_2^2 + q_3^2 \end{bmatrix} \quad (4.7)$$

The quaternion kinematic differential equations can be written compactly using the angular velocity vector $\boldsymbol{\omega}$,

$$\dot{\mathbf{q}} = \frac{1}{2} [B(\mathbf{q})] \boldsymbol{\omega} \quad (4.8)$$

where

$$B(\mathbf{q}) = \begin{bmatrix} q_4 I_{3 \times 3} + [\mathbf{q}_{13} \times] \\ \cdots \\ -\mathbf{q}_{13}^T \end{bmatrix} \quad (4.9)$$

where $I_{3 \times 3}$ is 3 dimensional identity matrix, $[\mathbf{q}_{13} \times]$ is referred to as the cross product matrix, since $\mathbf{a} \times \mathbf{b} = [\mathbf{a} \times] \mathbf{b}$, with

$$[\mathbf{a} \times] = \begin{bmatrix} 0 & -a_3 & a_2 \\ a_3 & 0 & -a_1 \\ -a_2 & a_1 & 0 \end{bmatrix} \quad (4.10)$$

However, the four elements of quaternion are not independent because quaternion represents the three degree-of-freedom attitude system by a four dimensional vector. From Eqs (4.5) and (4.6), we see that \mathbf{q} satisfies the following normalization constraint

$$\mathbf{q}^T \mathbf{q} = 1 \quad (4.11)$$

The Modified Rodrigues Parameters (MRPs) are a minimal attitude parameterization defined as:

$$\boldsymbol{\sigma} = \hat{\mathbf{e}} \tan\left(\frac{\Phi}{4}\right) = \frac{\mathbf{q}_{13}}{1 + q_4}, \quad \boldsymbol{\sigma} = [\sigma_1, \sigma_2, \sigma_3]^T \quad (4.12)$$

where $(\sigma_1, \sigma_2, \sigma_3)$ are the three MRPs. The MRP vector has a geometric singularity at $\Phi = \pm 360$ degree. Thus any rotation can be described except a complete revolution back to the original orientation. Furthermore, for small rotation, the MRPs are linearized as

$$\boldsymbol{\sigma} \approx \frac{\Phi}{4} \hat{\mathbf{e}} \quad (4.13)$$

The direction cosine matrix in terms of the MRPs is expressed in compact vector form:

$$A(\boldsymbol{\sigma}) = I + \frac{8 [\boldsymbol{\sigma} \times]^2 - 4(1 - \boldsymbol{\sigma}^T \boldsymbol{\sigma}) [\boldsymbol{\sigma} \times]}{(1 + \boldsymbol{\sigma}^T \boldsymbol{\sigma})^2} \quad (4.14)$$

The kinematic differential equation in terms of the MRPs is

$$\dot{\boldsymbol{\sigma}} = \frac{1}{4} [B(\boldsymbol{\sigma})] \boldsymbol{\omega} \quad (4.15)$$

where

$$[B(\boldsymbol{\sigma})] = (1 - \boldsymbol{\sigma}^T \boldsymbol{\sigma}) I + 2[\boldsymbol{\sigma} \times] + 2\boldsymbol{\sigma} \boldsymbol{\sigma}^T \quad (4.16)$$

4.2 Measurement Model

Recall the co-linearity equations in unit vector form in Eq.(2.9). The inherent sensor properties produce the measurement noise. When measurement noise is present, the measurements are assumed to be modeled by

$$\tilde{\mathbf{b}}_i = \mathbf{h}_i(\mathbf{x}) + \mathbf{v}_i \quad (4.17)$$

where

$$\mathbf{h}_i(\mathbf{x}) = A(\boldsymbol{\sigma}_i) \mathbf{r}_i(\mathbf{p}) \quad (4.18)$$

where $\tilde{\mathbf{b}}_i$ denotes the measurements from the i^{th} beacon and $\mathbf{x} = [\mathbf{p}; \boldsymbol{\sigma}]$ is the state vector of six degree-of-freedom navigation including relative position vector $\mathbf{p} = [X_c, Y_c, Z_c]^T$ and the MRPs attitude parameters, $\boldsymbol{\sigma} = [\sigma_1, \sigma_2, \sigma_3]^T$. The sensor noise \mathbf{v}_i is modeled as zero mean white Gaussian process with covariance matrix of measurement errors R_i

$$E\{\mathbf{v}_i\} = 0 \quad (4.19)$$

$$E\{\mathbf{v}_i \mathbf{v}_j^T\} = R_i \delta_{ij} \quad (4.20)$$

4.3 Measurement Sensitivity Matrix

From the measurement model in Eq.(4.18), the Jacobian matrix for i^{th} beacon, H_i is obtained by partial differentiating the measurement model with respect to the state

$$H_i = \frac{\partial \mathbf{h}_i}{\partial \mathbf{x}} = \begin{bmatrix} \frac{\partial \mathbf{h}_i}{\partial \mathbf{p}} & \vdots & \frac{\partial \mathbf{h}_i}{\partial \boldsymbol{\sigma}} \end{bmatrix} \quad (4.21)$$

where, partial derivative of measurement model with respect to the position vector can be written as

$$\frac{\partial \mathbf{h}_i}{\partial \mathbf{p}} = -A\{I_{3 \times 3} - \mathbf{r}\mathbf{r}^T\} / \sqrt{(X_i - X_c)^2 + (Y_i - Y_c)^2 + (Z_i - Z_c)^2} \quad (4.22)$$

The partial derivative of measurement model with respect to the MRPs is derived by the brute force differentiation of Eq. (4.18). However, brute force differentiation of three elements of vector in Eq. (4.18) with respect to three elements of MRPs is complicated for implementation. The composite rotation property [29] can be applied for deriving the compact form of partial derivative of measurement model with respect to the MRPs. Assumes that the true parameters are given by

$$\boldsymbol{\sigma} = \delta \boldsymbol{\sigma} \otimes \hat{\boldsymbol{\sigma}} \quad (4.23)$$

where $\hat{\boldsymbol{\sigma}}$ is the estimated MRPS and $\delta \boldsymbol{\sigma}$ is the attitude error of MRPs. The composite rule for the MRPs leads to the following [29]

$$\boldsymbol{\sigma} = \frac{(1 - \hat{\boldsymbol{\sigma}}^T \hat{\boldsymbol{\sigma}}) \delta \boldsymbol{\sigma} + (1 - \delta \boldsymbol{\sigma}^T \delta \boldsymbol{\sigma}) \hat{\boldsymbol{\sigma}} - 2[\delta \boldsymbol{\sigma} \times] \hat{\boldsymbol{\sigma}}}{1 + \hat{\boldsymbol{\sigma}}^T \hat{\boldsymbol{\sigma}} \delta \boldsymbol{\sigma}^T \delta \boldsymbol{\sigma} - 2\hat{\boldsymbol{\sigma}} \cdot \delta \boldsymbol{\sigma}} \quad (4.24)$$

For small $\delta \boldsymbol{\sigma}$, Eq. (4.24) can be approximated using [31]

$$\begin{aligned} \boldsymbol{\sigma} &\approx (1 + 2\delta \boldsymbol{\sigma} \cdot \hat{\boldsymbol{\sigma}}) \left[(1 - \hat{\boldsymbol{\sigma}}^T \hat{\boldsymbol{\sigma}}) \delta \boldsymbol{\sigma} + \hat{\boldsymbol{\sigma}} - 2[\delta \boldsymbol{\sigma} \times] \hat{\boldsymbol{\sigma}} \right] \\ &\approx \hat{\boldsymbol{\sigma}} + \left[(1 - \hat{\boldsymbol{\sigma}}^T \hat{\boldsymbol{\sigma}}) I_{3 \times 3} + 2[\boldsymbol{\sigma} \times] + 2\hat{\boldsymbol{\sigma}} \hat{\boldsymbol{\sigma}}^T \right] \delta \boldsymbol{\sigma} \end{aligned} \quad (4.25)$$

From

$$A(\boldsymbol{\sigma}) = A(\delta \boldsymbol{\sigma}) A(\hat{\boldsymbol{\sigma}}) \quad (4.26)$$

It follows that

$$\frac{\partial \mathbf{h}_i}{\partial \boldsymbol{\sigma}} = \frac{\partial}{\partial \boldsymbol{\sigma}} A(\delta \boldsymbol{\sigma}) A(\hat{\boldsymbol{\sigma}}) \mathbf{r}_i \quad (4.27)$$

Using the fact that for small $\delta \boldsymbol{\sigma}$

$$A(\delta \boldsymbol{\sigma}) \approx I_{3 \times 3} - 4[\delta \boldsymbol{\sigma} \times] \quad (4.28)$$

Eq. (4.27) can now be evaluated using the chain rule to yield

$$\begin{aligned} \frac{\partial \mathbf{h}_i}{\partial \boldsymbol{\sigma}} &= 4[\mathbf{A} \mathbf{r}_i \times] \{ (1 - \boldsymbol{\sigma}^T \boldsymbol{\sigma}) I_{3 \times 3} + 2[\boldsymbol{\sigma} \times] + 2\boldsymbol{\sigma} \boldsymbol{\sigma}^T \}^{-1} \\ &= \frac{4}{(1 + \boldsymbol{\sigma}^T \boldsymbol{\sigma})^2} [\mathbf{A} \mathbf{r}_i \times] \{ (1 - \boldsymbol{\sigma}^T \boldsymbol{\sigma}) I_{3 \times 3} - 2[\boldsymbol{\sigma} \times] + 2\boldsymbol{\sigma} \boldsymbol{\sigma}^T \} \end{aligned} \quad (4.29)$$

4.4 Gaussian Least Square Differential Correction

The Gaussian Least Square Differential Correction determines the optimal parameters of the nonlinear static equations. The cost function of this optimization problem is formulated to minimize the weighted square sum of the residual errors based on the Wahba problem least squares error criterion, given by

$$J = \frac{1}{2} \sum_{i=1}^N (\tilde{\mathbf{b}}_i - \mathbf{h}_i(\hat{\mathbf{x}}))^T W_i (\tilde{\mathbf{b}}_i - \mathbf{h}_i(\hat{\mathbf{x}})) \quad (4.30)$$

where, i is the beacon index and N is the available total number of line-of-sight vector measurements and $W = W^T > 0$ is a weight matrix used to weight the relative importance of each measurement. In the minimum variance estimation sense, the inverse measurement covariance matrix R^{-1} is a optimal weight matrix W . This optimization problem is solved by a non-linear least square algorithm, the Gaussian Least Square Differential Correction (GLSDC) estimation method [32]. Explicit closed form solution of the minimization problem in Eq. (4.30) impossible to find directly, however, it is known that a unique global minimum usually results if four or more beacons are present. GLSDC is designed to converge to accurate least square estimates, given approximate starting values through the iterative approximation procedure. Assume that the current

estimates of the unknown states $\hat{\mathbf{x}}_k$ are available, then unknown objective states $\hat{\mathbf{x}}_{k+1}$ are related to their respective current estimates and unknown correction $\Delta \mathbf{x}$

$$\hat{\mathbf{x}}_{k+1} = \hat{\mathbf{x}}_k + \Delta \mathbf{x} \quad (4.31)$$

If the components of $\Delta \mathbf{x}$ are sufficiently small, we may linearize $\mathbf{h}(\hat{\mathbf{x}})$ in Eq. (4.18) about $\hat{\mathbf{x}}_k$ using a first-order Taylor series expansion as

$$\mathbf{h}_i(\hat{\mathbf{x}}) \approx \mathbf{h}_i(\hat{\mathbf{x}}_k) + H_{i,k} \Delta \mathbf{x} \quad (4.32)$$

where $H_{i,k}$ is the Jacobian matrix of measurement model with respect to the current best estimate

$$H_{i,k} = \left[\frac{\partial \mathbf{h}_i}{\partial \mathbf{x}} \right]_{\hat{\mathbf{x}}_k} \quad (4.33)$$

Then the residual after state update can be linearly approximated as

$$\Delta \mathbf{b}_{i,k+1} = \tilde{\mathbf{b}}_i - \mathbf{h}_i(\hat{\mathbf{x}}_{k+1}) \approx \tilde{\mathbf{b}}_i - \mathbf{h}_i(\hat{\mathbf{x}}_k) - H_{i,k} \Delta \mathbf{x} = \Delta \mathbf{b}_{i,k} - H_{i,k} \Delta \mathbf{x} \quad (4.34)$$

With N available line-of-sight vector measurement, measurement set and predicted measurement set can be written by

$$\tilde{\mathbf{Y}} = \begin{bmatrix} \tilde{\mathbf{b}}_1 \\ \tilde{\mathbf{b}}_2 \\ \vdots \\ \tilde{\mathbf{b}}_N \end{bmatrix}, \quad \hat{\mathbf{Y}}_k = \begin{bmatrix} \mathbf{h}_1(\hat{\mathbf{x}}_k) \\ \mathbf{h}_2(\hat{\mathbf{x}}_k) \\ \vdots \\ \mathbf{h}_N(\hat{\mathbf{x}}_k) \end{bmatrix} \quad (4.35)$$

and the measurement residual set and sensitivity matrix are given by

$$\Delta \mathbf{Y}_k = \tilde{\mathbf{Y}} - \hat{\mathbf{Y}}_k = \begin{bmatrix} \tilde{\mathbf{b}}_1 - \mathbf{h}_1(\hat{\mathbf{x}}_k) \\ \tilde{\mathbf{b}}_2 - \mathbf{h}_2(\hat{\mathbf{x}}_k) \\ \vdots \\ \tilde{\mathbf{b}}_N - \mathbf{h}_N(\hat{\mathbf{x}}_k) \end{bmatrix}, \quad A_k = \begin{bmatrix} H_1 \\ H_2 \\ \vdots \\ H_N \end{bmatrix} \quad (4.36)$$

The local strategy for determining the approximate corrections is to select the particular corrections that lead to minimize the sum of squares of the linearly predicted residuals:

$$J_{k+1} \approx \frac{1}{2} (\Delta \mathbf{Y}_k - A_k \Delta \mathbf{x})^T W (\Delta \mathbf{Y}_k - A_k \Delta \mathbf{x}) \quad (4.37)$$

The minimization Eq. (4.37) is analogous to the minimized quadratic form. Therefore the appropriate state correction is given by

$$\Delta \mathbf{x} = P_k A_k^T W \Delta \mathbf{Y}_k \quad (4.38)$$

where P_k is the covariance matrix which is given by

$$P_k = (A_k^T W A_k)^{-1} \quad (4.39)$$

Then, $\hat{\mathbf{x}}_k$ will be updated with an improved estimate of $\hat{\mathbf{x}}_{k+1}$ from Eq. (4.31).

In order to implement the GLSDC, an initial guess $\hat{\mathbf{x}}_o$ is required to begin the algorithm and stopping condition of iteration with an accuracy dependent tolerance given by

$$\delta J \equiv \frac{|J_k - J_{k-1}|}{J_k} < \frac{\varepsilon}{\|W\|} \quad (4.40)$$

where ε is a prescribed small value. If Eq. (4.40) is not satisfied, then the update procedure is iterated with the new estimate as the current estimate until the process converges, or maximum number of iterations is exceeded, or J increases on successive iterations. The complete GLSDC algorithm is summarized in Figure 28.

While a theoretical proof of convergence of the GLSDC algorithm is not available, for four distinct line-of-sight measurements and starting estimates adequate starting values, reliable convergence has been achieved. It is expected that the MRPs are not used and Euler angle are used, then much more restrictive i.e. good starting values are necessary for convergence due to kinematic and geometric non-linearity. Experience indicates that initial attitude errors of $\|\Delta \boldsymbol{\sigma}\| \leq 0.2$, which is corresponding to large

rotational errors of less than $\sim 45^\circ$ about any axis, converges very quickly, Likewise, position errors of $\|\Delta\mathbf{r}\|/\|\mathbf{r}\| \leq 0.2$ usually converge quickly. Even for such large starting errors, we find ten or fewer iterations are usually required to reach a converged solution. When more iterations are required, we typically find the reason to be that the beacons are too close in an angular sense as seen by the sensor. When the suffered angle is less than ten degrees, poor geometric and convergence difficulties arise. The actual convergence statistics is studied in Chapter VI.

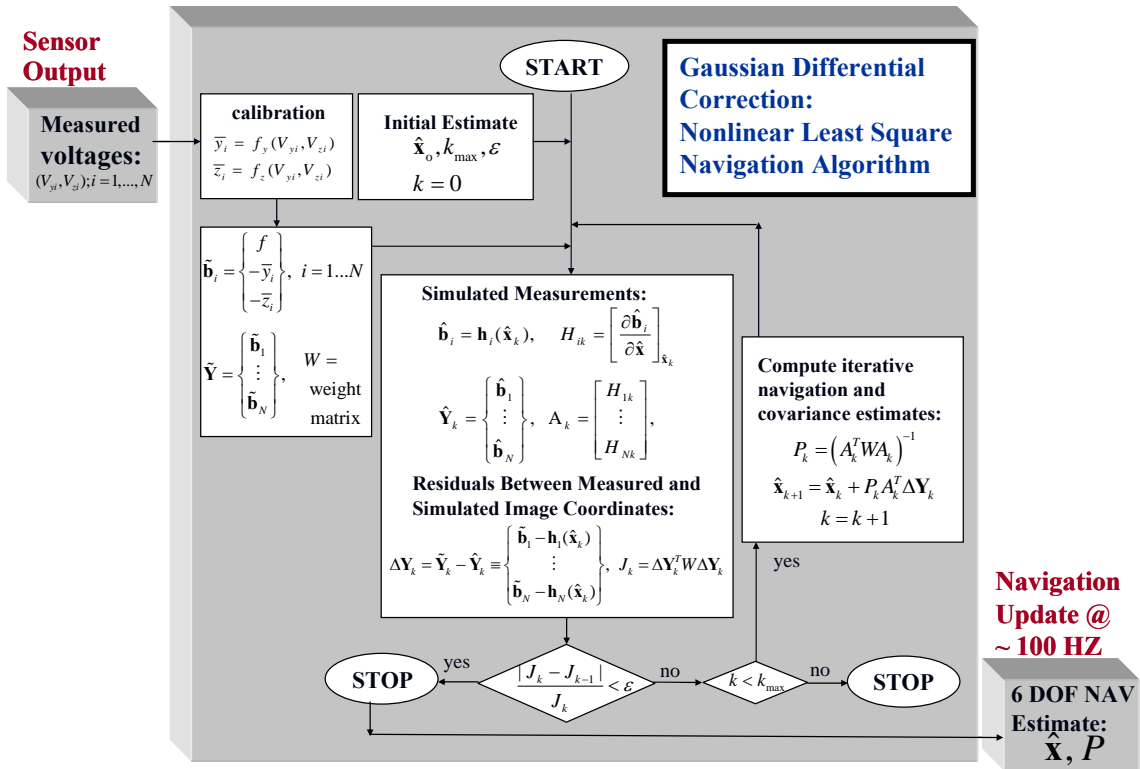


Figure 28 Gaussian Least Squares Differential Correction algorithm

CHAPTER V

DYNAMIC STATE ESTIMATION

In case we have information about the nonlinear system dynamics and stochastic properties of measurement and model error, we can better estimate position, attitude, linear velocities, and angular velocities using dynamic optimal estimation technique [32], [33], [34]. For slow motions and fast update rates, a very simple dynamical model may suffice. For fast irregular motions and slow update rates, however, a complicated and accurate dynamical model is required. Alternatively, we may use very precise rate or acceleration sensor (IMU) in lieu of a dynamical model. The dynamical model can vary from near trivial to very complicated, as mentioned above. In the presented research, an EKF algorithm is developed using line of sight measurement from the VisNav system with attitude parameters by the MRPs, for various dynamical models.

5.1 Extended Kalman Filter Description

The VisNav systems involve nonlinear continuous-time state and discrete-time measurements in Eq. (4.17) collected by a digital signal processor. The state equation and measurement equations are represented by [32], [33]:

$$\dot{\mathbf{x}}(t) = \mathbf{f}(\mathbf{x}(t), t) + G(t)\mathbf{w}(t) \quad (5.1)$$

$$\tilde{\mathbf{Y}}_k = \mathbf{h}(\mathbf{x}_k, t_k) + \mathbf{v}_k \quad (5.2)$$

where process noise $\mathbf{w}(t)$ and measurement noise \mathbf{v}_k are zero mean Gaussian noise with covariance given by

$$E\{\mathbf{w}(t)\} = 0, \quad E\{\mathbf{w}(t)\mathbf{w}^T(\tau)\} = Q(t)\delta(t - \tau) \quad (5.3)$$

$$E\{\mathbf{v}_k\} = 0, \quad E\{\mathbf{v}_k \mathbf{v}_l^T\} = R_k \delta_{kl} \quad (5.4)$$

The structure of EKF can be divided into two primary parts, propagation and update. The state equations and error covariance matrix equation are propagated forward in time until a measurement occurs

$$\dot{\hat{\mathbf{x}}}(t) = \mathbf{f}(\mathbf{x}(t), t) \quad (5.5)$$

$$\dot{P} = F(t)P(t) + P(t)F^T(t) + G(t)Q(t)G^T(t) \quad (5.6)$$

where $F(t)$ is the sensitivity matrix of the state equation with respect to the best current estimate

$$F(t) = \left[\frac{\partial \mathbf{f}}{\partial \mathbf{x}} \right]_{\hat{\mathbf{x}}(t)} \quad (5.7)$$

For computational efficiency, continuous-time state and covariance matrix equation may be converted into discrete-time system [32]

$$\hat{\mathbf{x}}_{k+1}^- = \Phi_k \hat{\mathbf{x}}_k^+ \quad (5.8)$$

$$P_{k+1}^- = \Phi_k P_k^+ \Phi_k^T + G_k Q_k G_k^T \quad (5.9)$$

where Φ_k is the state transition matrix for the step from t_k to t_{k+1} , and $Q_k = E\{\mathbf{w}_k \mathbf{w}_k^T\}$. where \mathbf{w}_k is the driven response at t_{k+1} due to the presence of the white Gaussian noise during the (t_k, t_{k+1}) interval. If we can assume that F is constant over (t_k, t_{k+1}) interval of sampling, Then the state transition matrix is simply the matrix exponential of $F_k \Delta t$:

$$\Phi_k = e^{F_k \Delta t} \approx I + F_k \Delta t \quad (5.10)$$

Given the new measurement at time t_k , the state and covariance can be updated using the following equations:

$$\hat{\mathbf{x}}_k^+ = \hat{\mathbf{x}}_k^- + K_k \left[\tilde{\mathbf{Y}}_k - \mathbf{h}(\hat{\mathbf{x}}_k^-) \right] \quad (5.11)$$

$$P_k^+ = (I - K_k A_k(\hat{\mathbf{x}}_k^-)) P_k^- \quad (5.12)$$

where the superscript + and – denote the estimate after measurements update and the propagated estimate at the update time, respectively. The optimal Kalman gain K_k can be determined which minimizes the norm of the estimation error. It is equivalent to minimize the trace of the error covariance P_k^+

$$\text{Min } J(K_k) = \text{Tr} \left[E \left\{ (\hat{\mathbf{x}}_k^+ - \mathbf{x})(\hat{\mathbf{x}}_k^+ - \mathbf{x})^T \right\} \right] = \text{Tr}(P_k^+) \quad (5.13)$$

Then, the optimal Kalman gain K_k is determined as

$$K_k = P_k^- H_k^T \left[A_k P_k^- A_k^T + R_k \right]^{-1} \quad (5.14)$$

where A_k is the sensitivity matrix of the measurement equations:

$$A_k = \left[\frac{\partial \mathbf{h}}{\partial \mathbf{x}} \right]_{\hat{\mathbf{x}}_k^-} \quad (5.15)$$

5.2 Zero Acceleration Dynamic Model

The applicability of the EKF rests on the availability of an accurate dynamical model because we use a dynamical model to predict the states. However, dynamical modeling for aircraft and spacecraft includes many difficulties in establishing valid torque and force models. This research assumes the simplest model, namely a piecewise constant linear and angular velocity model between each measurement, which has been forced a reasonable assumption for high sampling rate. In this case, the state vector for the EKF is the relative position vector \mathbf{p} , the modified Rodrigues attitude parameters $\boldsymbol{\sigma}$, the relative linear velocity vector \mathbf{v} , and the relative angular velocity vector $\boldsymbol{\omega}$. Therefore, the state equations are given by

$$\begin{aligned}
\dot{\mathbf{p}} &= \mathbf{v} \\
\dot{\boldsymbol{\sigma}} &= \frac{1}{4}[(1 - \boldsymbol{\sigma}^T \boldsymbol{\sigma})I + 2[\boldsymbol{\sigma} \times] + 2\boldsymbol{\sigma}\boldsymbol{\sigma}^T] \boldsymbol{\omega} = \frac{1}{4}[B(\boldsymbol{\sigma})] \boldsymbol{\omega} \\
\dot{\mathbf{v}} &= \mathbf{d}_v \\
\dot{\boldsymbol{\omega}} &= \mathbf{d}_\omega
\end{aligned} \tag{5.16}$$

where \mathbf{d}_v and \mathbf{d}_ω are the zero mean white Gaussian process noise. Notice the exact nonlinear kinematic model is used to propagate $\boldsymbol{\sigma}(t)$; this enables large angle displacements. The exact kinematics wisely make approximations at the acceleration level where the physical uncertainty actually arises.

Then the linearized model Jacobian matrix used in the EKF are given by

$$F = \begin{bmatrix} 0 & 0 & I_{3 \times 3} & 0 \\ 0 & \frac{\partial \dot{\boldsymbol{\sigma}}}{\partial \boldsymbol{\sigma}} & 0 & \frac{1}{4}[B(\boldsymbol{\sigma})] \\ 0 & 0 & 0 & 0 \\ 0 & 0 & 0 & 0 \end{bmatrix} \tag{5.17}$$

where the partial derivatives of $\dot{\boldsymbol{\sigma}}$ with respect to $\boldsymbol{\sigma}$ and $\boldsymbol{\omega}$ are arranged as

$$\frac{\partial \dot{\boldsymbol{\sigma}}}{\partial \boldsymbol{\sigma}} = \frac{1}{2} \left\{ -\boldsymbol{\omega}\boldsymbol{\sigma}^T - [\boldsymbol{\omega} \times] + \boldsymbol{\sigma}^T \boldsymbol{\omega} I_{3 \times 3} + \boldsymbol{\sigma}\boldsymbol{\omega}^T \right\} \tag{5.18}$$

The first two equations in Eq. (5.16) represent the exact kinematic relationships. So, they are enforced exactly, i.e. process noise should not affect these two exact kinematic differential equations. The structure of the G matrix should reflect how the process noise covariance Q should propagate the covariance matrix between measurement updates. Therefore the first two rows of G are zeros, G has the structure

$$G = \begin{bmatrix} 0 & 0 & 0 & 0 \\ 0 & 0 & 0 & 0 \\ 0 & 0 & I_{3 \times 3} & 0 \\ 0 & 0 & 0 & I_{3 \times 3} \end{bmatrix} \tag{5.19}$$

5.3 VisNav / IMU Integration

In the previous chapter, we assumed the zero acceleration model with process noise so that the EKF will “forget” the past and revise the position and velocity estimate accordingly. However, the estimated state history is not actually constrained to enforce zero acceleration. Furthermore, the VisNav system requires the VisNav sensor to access the number of beacons’ signals being received. Sometimes, one or more of the optical target will be out of sensor field-of-view or the viewing angles between two or more beacons may be so small that we could encounter a geometric singularity. These events occasionally make geometric solutions via GLSDC impossible and cause an intermittent data dropout. In this case, we can continue to provide a navigation estimate by propagating with the equations of motion or by integrating the dead reckoning sensor output such as an IMU. On the other hand, the IMU output is corrupted by bias and drift; but these can be neatly estimated by the EKF from the independent VisNav measurement. The VisNav/IMU integration method can take advantage of the strengths of both systems while minimizing the impact of their weaknesses. Thus, integration of the VisNav with an IMU into a forward EKF is necessary to establish a robust navigation system. For the same reasons, there are analogous GPS/INS integration studies, leading to Kalman filter based navigation algorithms [35], [36], [37] that use two or more data types.

The present research has developed a more precise and robust navigation algorithm by employing a VisNav/IMU sensor fusion technique in which the independent VisNav system measurements serve to correct long-term drift of IMU. These lead to an EKF (EKF) which computes the optimal navigation solution by proper gains operating on the inputs from the VisNav and IMU. Thereby, this fused navigation system provides a continuous best estimate of the dynamic system’s position, velocity and attitude vector, and is much more robust with respect to occasional VisNav data dropouts than forward propagation using an approximate dynamical model..

5.3.1 IMU Measurement Model

An Inertial Measuring Unit (IMU) provides densely measured linear acceleration and angular rate by the accelerometer and gyro. IMU has a wide dynamic bandwidth and can be sampled at high rates, therefore it can capture the fast dynamics of a maneuverable vehicle such as an aircraft. Furthermore, an IMU does not rely on any external aids and does not necessary to emit or receive any detectable radiation. However, IMU measurements are corrupted by noise, scale factor errors, bias and drift variation so that the errors may be accumulated and lead to significant drift in the position, velocity, and attitude output.

The IMU of six degree-of-freedom measurement systems is designed to measure linear acceleration along three orthogonal axes and rotation rates around three orthogonal axes using three accelerometers and three axis gyro to make a complete six degree-of-freedom measurement of the dynamics. The acceleration and angular rate measured by the accelerometers and gyro respectively is represented as:

$$\begin{aligned}\tilde{\mathbf{a}} &= \mathbf{a} + \mathbf{b}_a + \boldsymbol{\eta}_a \\ \tilde{\boldsymbol{\omega}} &= \boldsymbol{\omega} + \mathbf{b}_\omega + \boldsymbol{\eta}_\omega\end{aligned}\tag{5.20}$$

where, $\tilde{\mathbf{a}}$ is the linear accelerometer output along body axes, \mathbf{a} is true linear acceleration, \mathbf{b}_a is the acceleration bias, $\boldsymbol{\eta}_a$ is the white Gaussian acceleration output noise, $\tilde{\boldsymbol{\omega}}$ is the gyro output angular rate around body axes, $\boldsymbol{\omega}$ is true angular rate, \mathbf{b}_ω is the angular rate bias, and $\boldsymbol{\eta}_\omega$ is the white Gaussian angular rate output noise.

As one inexpensive and moderately accurate IMU, consider the specifications for the Crossbow IMU-300CB as summarized in Table 4 [38].

Table 4 Specifications of Crossbow IMU-300CB

Update rate(Hz)	> 100Hz
3 axis -Gyro	
Range(deg/sec)	± 100
Bias(deg/sec)	< ± 2.0
Scale Factor Accuracy(%)	< 1
Non-Linearity(% FS)	< 0.3
Resolution(deg/sec)	< 0.05
Random Walk(deg/min)	< 0.85
3 axis – accelerometer	
Range(g)	± 2
Bias(mg)	< ± 30
Scale Factor Accuracy(%)	< 1
Non-Linearity(% FS)	< 1
Resolution(mg)	< 1.0
Random Walk(m/s/min)	< 0.15

5.3.2 Extended Kalman Filter with VisNav/IMU Integration

The application of the EKF to combine the VisNav and IMU measurements requires an adequate dynamic model:

$$\dot{\mathbf{x}}(t) = \mathbf{f}(\mathbf{x}(t), t) + \mathbf{G}(t)\mathbf{w}(t) \quad (5.21)$$

where $\mathbf{x}(t)$ is 15×1 system state vector defined as:

$$\mathbf{x}(t) = [\mathbf{p} : \boldsymbol{\sigma} : \mathbf{v} : \mathbf{b}_a : \mathbf{b}_\omega] \quad (5.22)$$

Recall that the state vector is comprised by relative position vector \mathbf{p} , modified rodrigues attitude parameters $\boldsymbol{\sigma}$, and relative velocity vector \mathbf{v} , defined with respect to the inertial reference frame. On the other hand, acceleration bias \mathbf{b}_a and angular rate bias \mathbf{b}_ω are defined with respect to the body frame. The system dynamics is represented by

$$\begin{aligned} \dot{\mathbf{p}} &= \mathbf{v} \\ \dot{\boldsymbol{\sigma}} &= \frac{1}{4} [B(\boldsymbol{\sigma})][\tilde{\boldsymbol{\omega}} - \mathbf{b}_\omega - \boldsymbol{\eta}_\omega] \\ \dot{\mathbf{v}} &= C_{B/N}^T(\boldsymbol{\sigma})[\tilde{\mathbf{a}} - \mathbf{b}_a - \boldsymbol{\eta}_v] \\ \dot{\mathbf{b}}_a &= \mathbf{v}_a \\ \dot{\mathbf{b}}_\omega &= \mathbf{v}_\omega \end{aligned} \quad (5.23)$$

where $C_{B/N}$ is the direction cosine matrix which transforms the inertial reference frame to body frame, so $C_{B/N}^T$ transforms the body frame to the inertial reference frame. In order to apply the EKF described in section 5.1, the Jacobian matrix of state differential equations

$$F(t) = \begin{bmatrix} 0 & 0 & I_{3 \times 3} & 0 & 0 \\ 0 & \frac{\partial \dot{\boldsymbol{\sigma}}}{\partial \boldsymbol{\sigma}} & 0 & 0 & -\frac{1}{4}B(\boldsymbol{\sigma}) \\ 0 & 0 & 0 & -C_{B/N}^T(\boldsymbol{\sigma}) & 0 \\ 0 & 0 & 0 & 0 & 0 \\ 0 & 0 & 0 & 0 & 0 \end{bmatrix} \quad (5.24)$$

where the partial derivatives of $\dot{\boldsymbol{\sigma}}$ with respect to $\boldsymbol{\sigma}$ and $\boldsymbol{\omega}$ are arranged as:

$$\frac{\partial \dot{\boldsymbol{\sigma}}}{\partial \boldsymbol{\sigma}} = \frac{1}{2} \left\{ -\hat{\boldsymbol{\omega}} \boldsymbol{\sigma}^T - [\hat{\boldsymbol{\omega}} \times] + \boldsymbol{\sigma}^T \hat{\boldsymbol{\omega}} I_{3 \times 3} + \boldsymbol{\sigma} \hat{\boldsymbol{\omega}}^T \right\} \quad (5.25)$$

\mathbf{w} is 15×1 system noise vector defined as

$$\mathbf{w} = [0_{1 \times 3} : \boldsymbol{\eta}_\omega : \boldsymbol{\eta}_v : \mathbf{v}_a : \mathbf{v}_\omega] \quad (5.26)$$

where \mathbf{v}_a is white Gaussian noise of accelerometer first-order Markov and \mathbf{v}_ω is white Gaussian noise of gyro first-order Markov process error. The corresponding system noise influence matrix $G(t)$ is defined as

$$G(t) = \begin{bmatrix} 0 & 0 & 0 & 0 & 0 \\ 0 & -\frac{1}{4}[B(\boldsymbol{\sigma})] & 0 & 0 & 0 \\ 0 & 0 & -C_{B/N}^T(\boldsymbol{\sigma}) & 0 & 0 \\ 0 & 0 & 0 & I_{3 \times 3} & 0 \\ 0 & 0 & 0 & 0 & I_{3 \times 3} \end{bmatrix} \quad (5.27)$$

CHAPTER VI

SIMULATION STUDIES

For the numerical simulation studies, it was assumed that the chase vehicle which uses the VisNav sensor system during a range 65 meters i.e. we adopt as typical initial condition, the initial position $\mathbf{p} = [-50, 30, 30]^T$ meters to target vehicle (Figure 29). It was also assumed that the 20 degree in roll, 10 degree in pitch, and 5 degree in yaw occur during maneuver. These position and attitude initial conditions initiate a nominal maneuver to the origin performed in 60 seconds.

The position and attitude data update rate was taken as 100Hz which is the data update rate of the current invented VisNav system. Based on historical understanding of spacecraft and aircraft dynamics, this update is more than adequate for all but the most aggressive of maneuvers. Using a modern IMU, this rate can be increased, if needed, to accommodate special applications. For sake of simplicity, the ISC is assumed to be the same as that the vehicle's body frame. Eight beacons within a volume of $1 \times 2 \times 2$ meters are used with locations in on the target vehicle as seen Figure 30. This is compatible with near optimum geometry for the end game of a rendezvous and docking maneuver.

The simulated VisNav measurements were calculated from the co-linearity equations and white Gaussian noises were added to the measurements according to the VisNav calibration accuracy with a standard deviation of $2.0E-5$ meters. Figure 31 shows that the image coordinates corresponding to the simulated trajectory.

6.1 GLSDC Implementation

A GLSDC optimal estimation algorithm using line-of-sight vector measurements from the VisNav system is applied to measured data consistent with the simulated navigation trajectory.

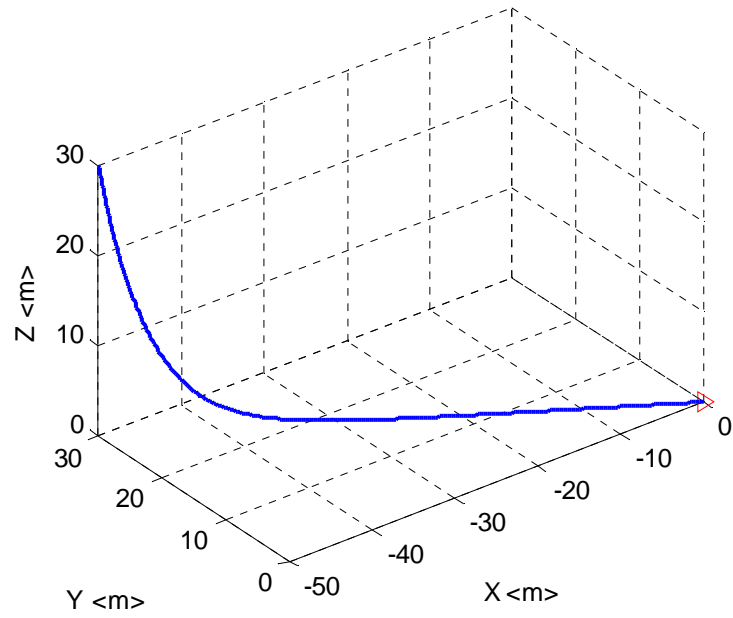


Figure 29 Simulated trajectory

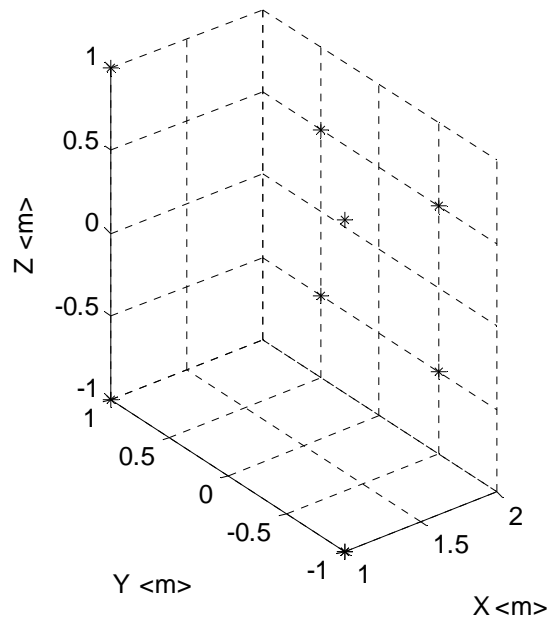


Figure 30 Beacons' configuration

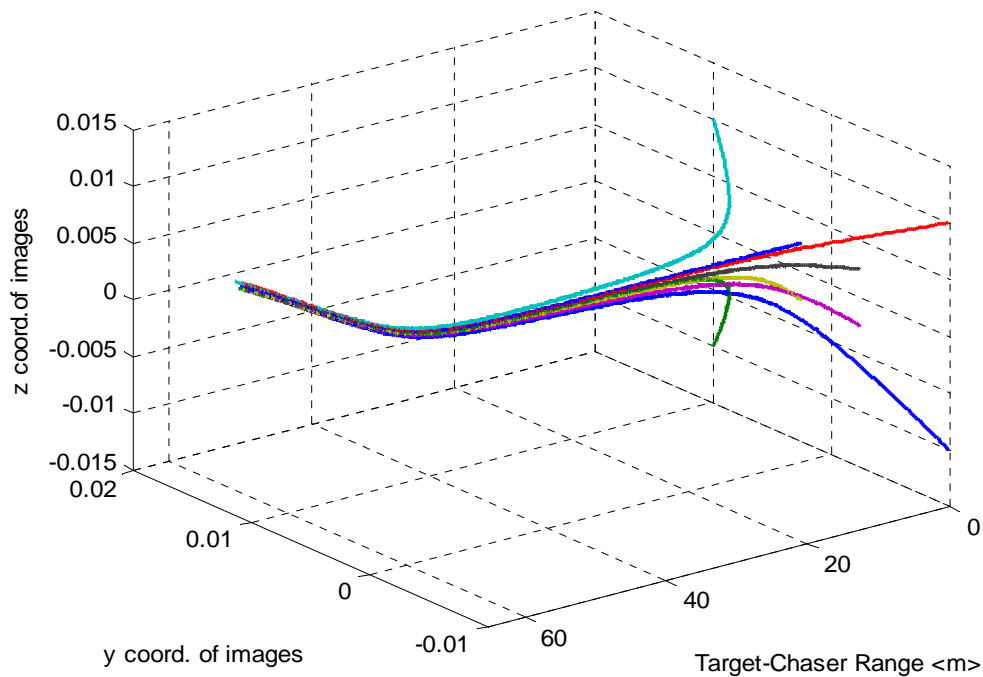


Figure 31 Time evolution of the image coordinates corresponding to the simulated trajectory

In order to check the robustness of the initial guess of the GLSDC for case of using MRPs, very poor initial guess as almost arbitrary values are set for the initial guess as shown in Table 5.

The condition number of covariance matrix is shown in Figure 32 and the number of iterations of GLSDC as measurements are received as a function of time are shown in Figure 33. For all of these iterations, we used the poor starting estimates of Table 5. Note the extremely well conditioned iterations as range approaches zero results in extremely efficient terminal convergence, but even in the worst conditioned cases at the beginning stage, ten or fewer iterations were required. In practice, the convergence can be vastly accelerated by using a neighboring converged solution to begin, rather than initiation with large estimation errors was done for illustration here. These are reputation of many similar trials to verify that these solutions are the global minima.

Table 5 Initial guess of GLSDC

	True values	Initial Guess
Position <m>	$[-50, 30, 30]^T$	$[-1, 1, 1]^T$
MRPs	$[0.09, -0.04, 0.03]^T$	$[0, 0, 0]^T$

As the chaser approaches the target, the image coordinates are more separated over the whole span the PSD active area (Figure 31), so there is a better geometric condition (the beacons become separated by about 90 degrees). On the other hand, small separations of beacon images reduce the distinction of each beacon, which geometric produces a dilution of precision (the beacons approach angular co-location). In the limit, as the beacons image approach a point, the measurement Jacobian has only two non-zero singular values, rather the six, as required for six degree of freedom navigation solution. The condition number becomes smaller approaching the ideal minimum of unity as the chaser approaches to the target and just a few iterations are necessary at the final stage of navigation.

The position/attitude errors and 3-sigma bounds from the converged covariance matrix, for case of using GLSDC algorithm are shown in Figure 34 and Figure 35. The converged position estimate errors at the beginning of the navigation are around 5 meters, and reduce to less than 1 centimeters as the chaser reaches its target just in front of the beacons. The converged attitude estimate errors at the beginning of the maneuver are around 5 degrees, and reduce to values less than 0.1 degree at final stage.

It is emphasized that each plot in Figure 34 and Figure 35 correspond to a six degree-of-freedom least square position and attitude estimated based purely or geometry. As will be evident in the next chapter, these geometrical best estimates can be tied together using the EKF, to proceed a smoother and even more precise optimal estimate for relative position and attitude.

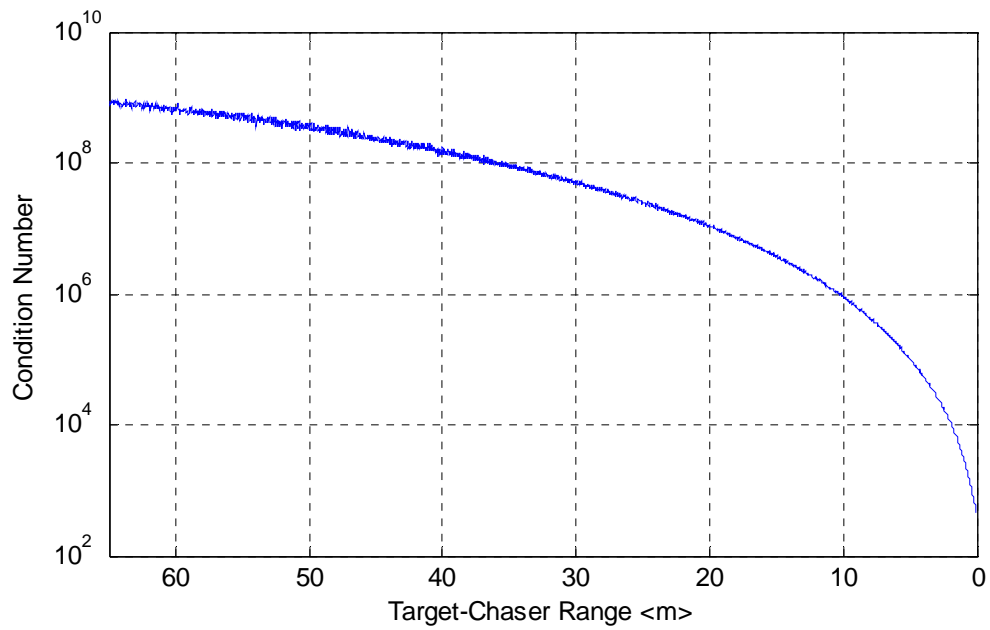


Figure 32 Condition numbers of GLSDC (Approach phase)

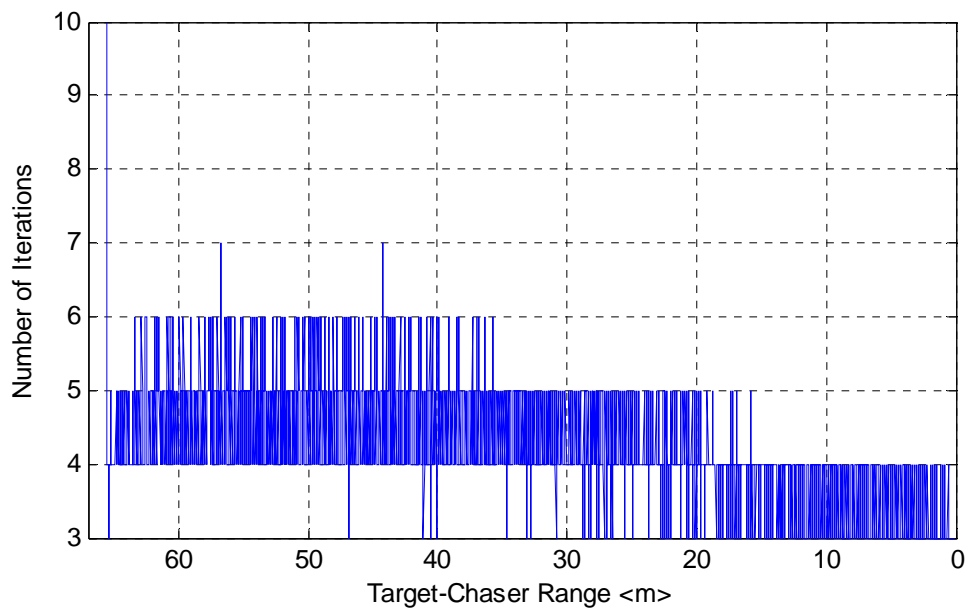
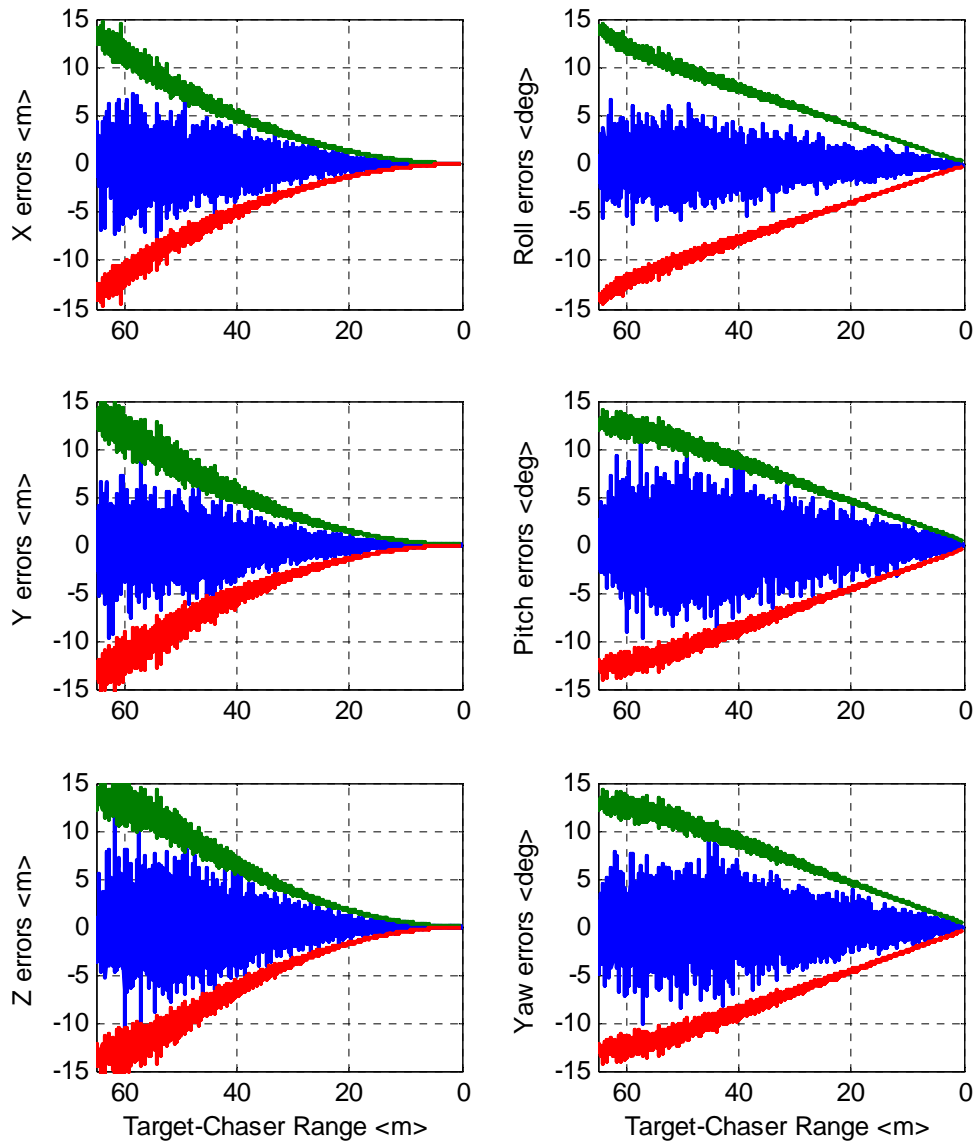
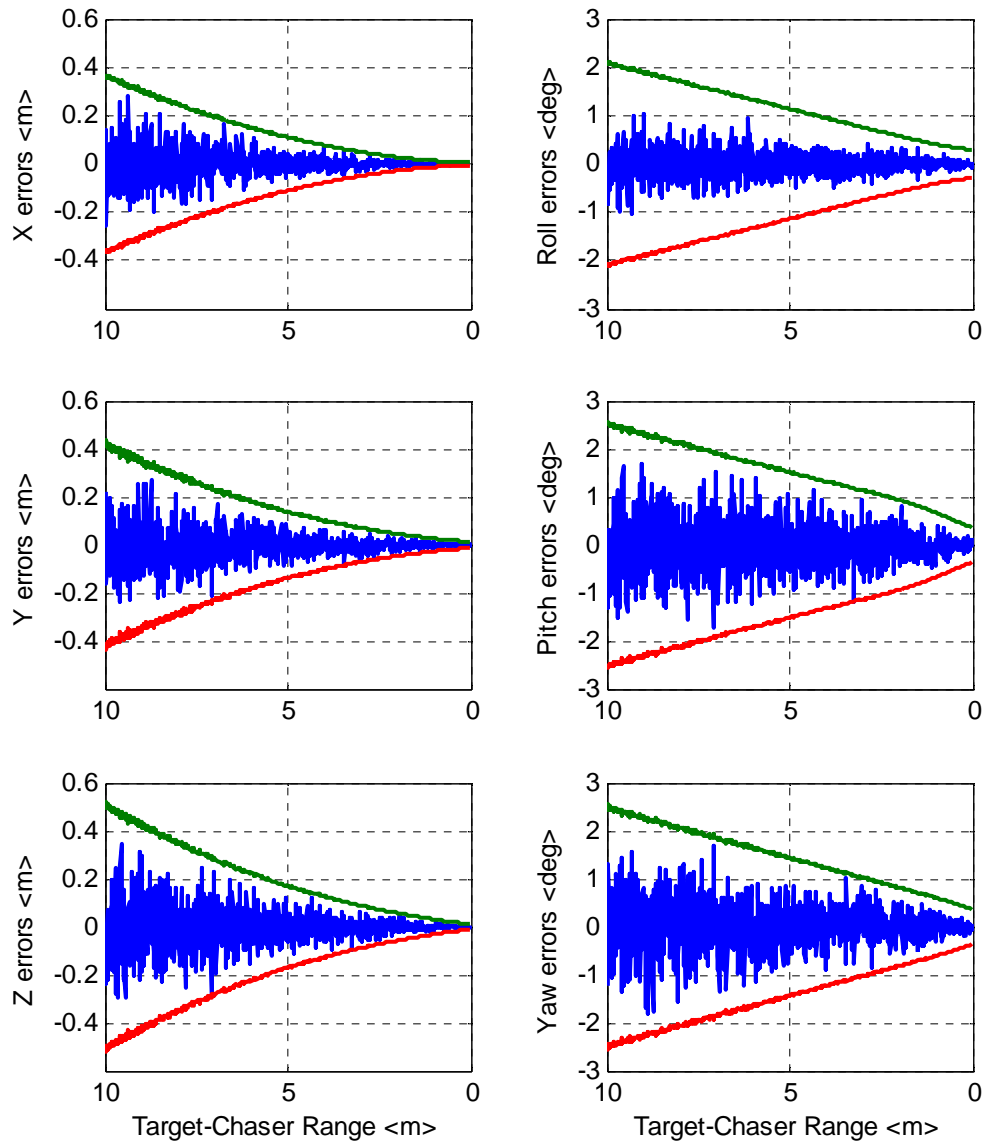


Figure 33 Iteration numbers of GLSDC (Approach phase)



**Figure 34 Position/attitude errors and 3-sigma bounds of GLSDC
(Approach phase)**



**Figure 35 Position/attitude errors and 3-sigma bounds of GLSDC
(End-game)**

6.2 EKF Implementation with Zero Acceleration Model

To illustrate convergence from a poor starting estimate, the initial estimates for the EKF implementation are set to 80% of their respective true state values. This initial estimates accuracy corresponds approximately to the GLSDC accuracy at the beginning stage of the navigation. The initial covariance matrix is set to the following diagonal matrix

$$P_o = 10^3 I_{12 \times 12} \quad (6.1)$$

It have been verified that the convergence history depends only weakly on P_o , whereas the long-term convergence is especially independent of P_o . The covariance matrix of process noise Q is assumed to be

$$Q = \begin{bmatrix} 0_{3 \times 3} & & & 0 \\ & 0_{3 \times 3} & & \\ & & 10^{-5} I_{3 \times 3} & \\ 0 & & & 10^{-3} I_{3 \times 3} \end{bmatrix} \quad (6.2)$$

The position and attitude errors and 3-sigma bounds in case of using an EKF algorithm are shown in Figure 36 and Figure 37. The converged position estimate errors near the beginning of the navigation process are around 1 meter, and reduce to a few millimeters as the chaser reaches near the target, just in front of the beacons. The converged attitude estimate errors at the beginning of the maneuver are around 1 degree, and reduce to values less than 0.03 degree at final stage. The EKF also provides dynamic information such as linear velocity and angular rate with processing of VisNav measurements. The velocity/angular rate estimation errors are shown in Figure 38. Figure 39 clearly shows that the EKF with the zero acceleration plus process noise model performs extremely well in case the motion of the chaser was sufficiently slow as compared to the rate of acquisition and processing of line of sight measurements.

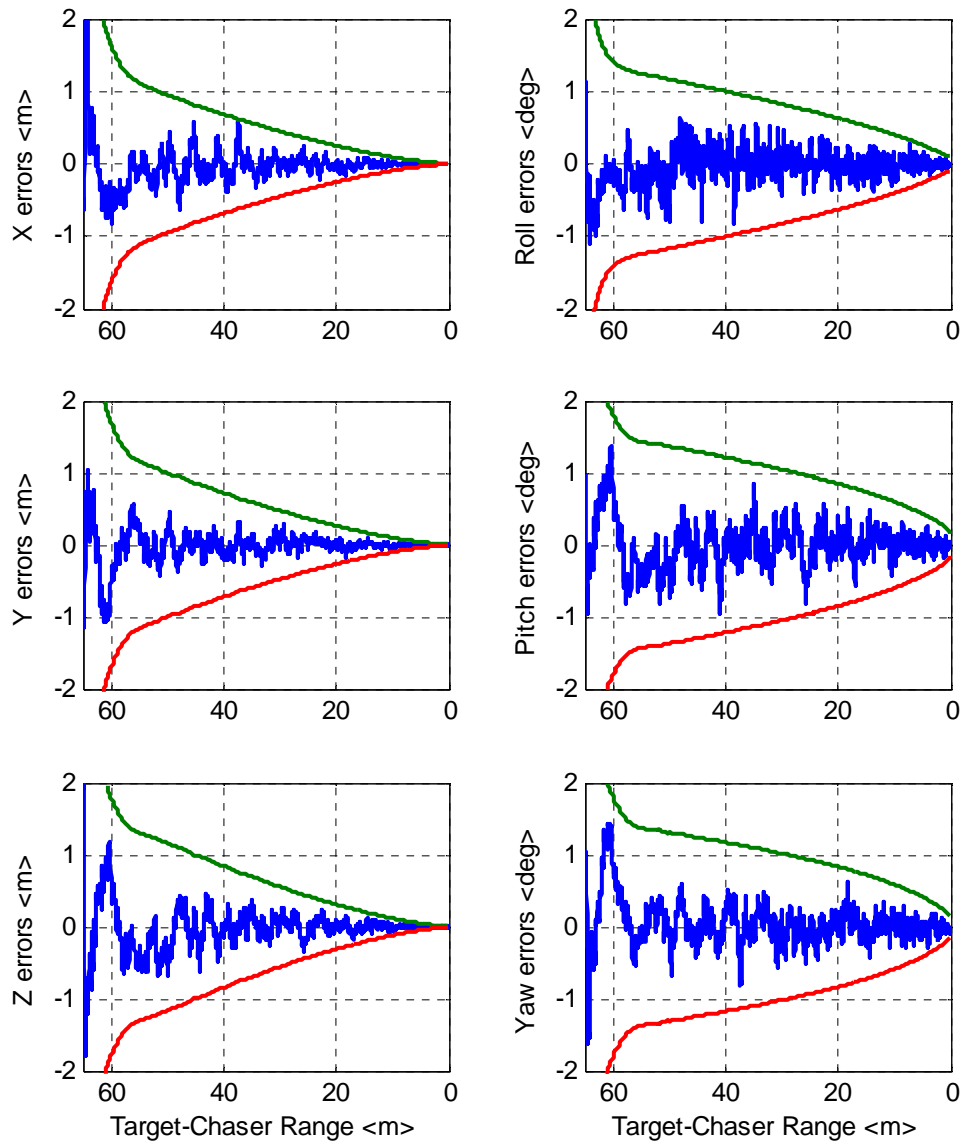


Figure 36 Position/attitude errors and 3-sigma bounds of EKF with zero acceleration model (Approach phase)

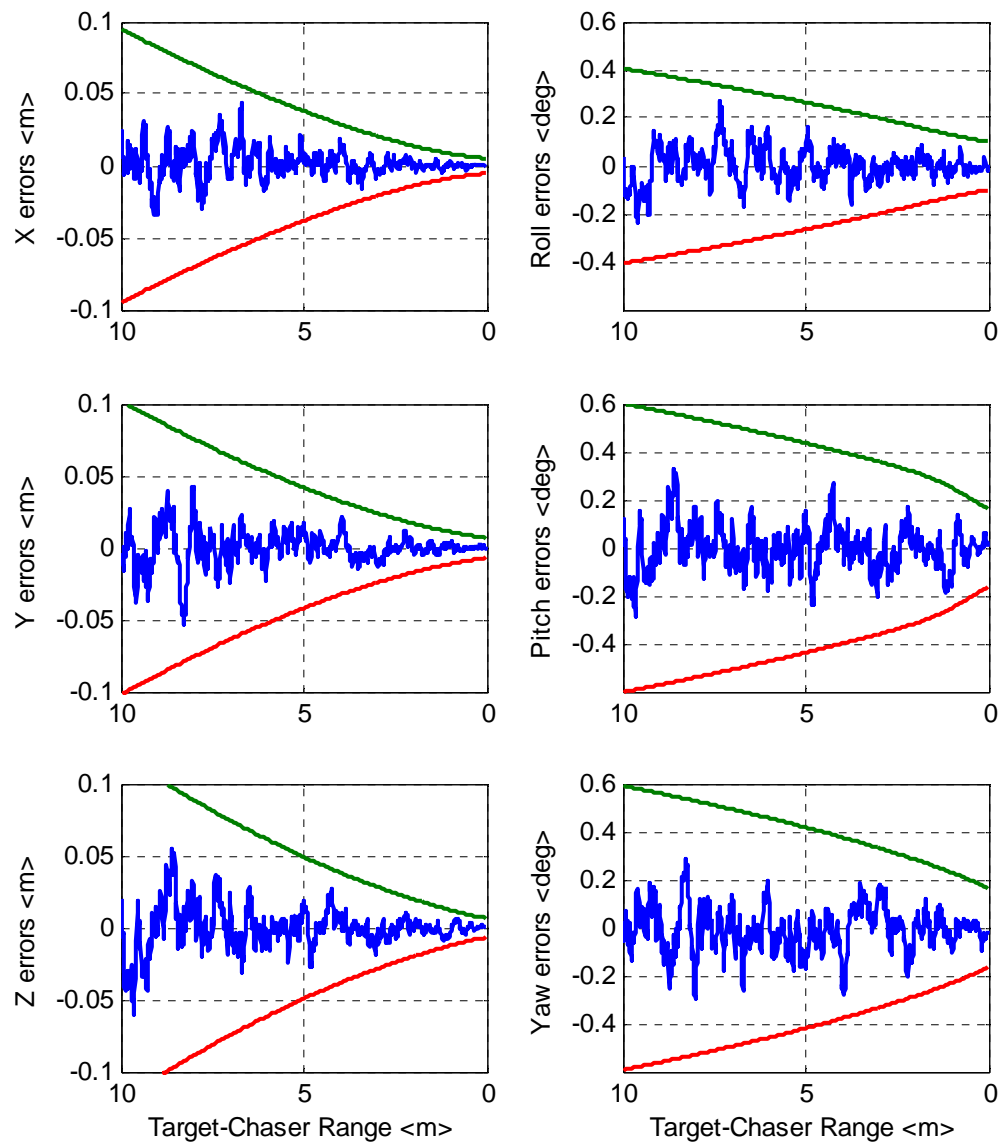


Figure 37 Position/attitude errors and 3-sigma bounds of EKF with zero acceleration model (End-game)

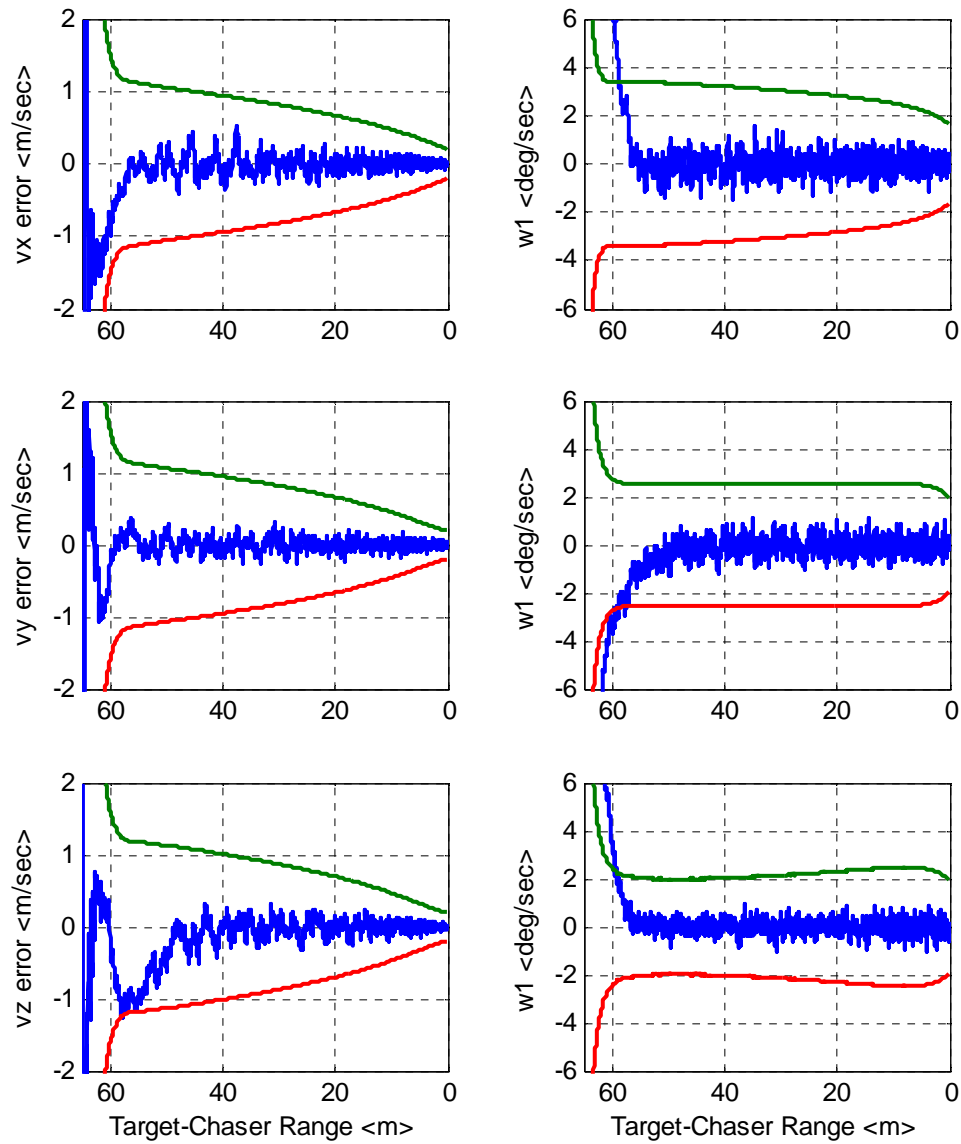


Figure 38 Linear velocity/angular rate errors and 3-sigma bounds of EKF with zero acceleration model (Approach phase)

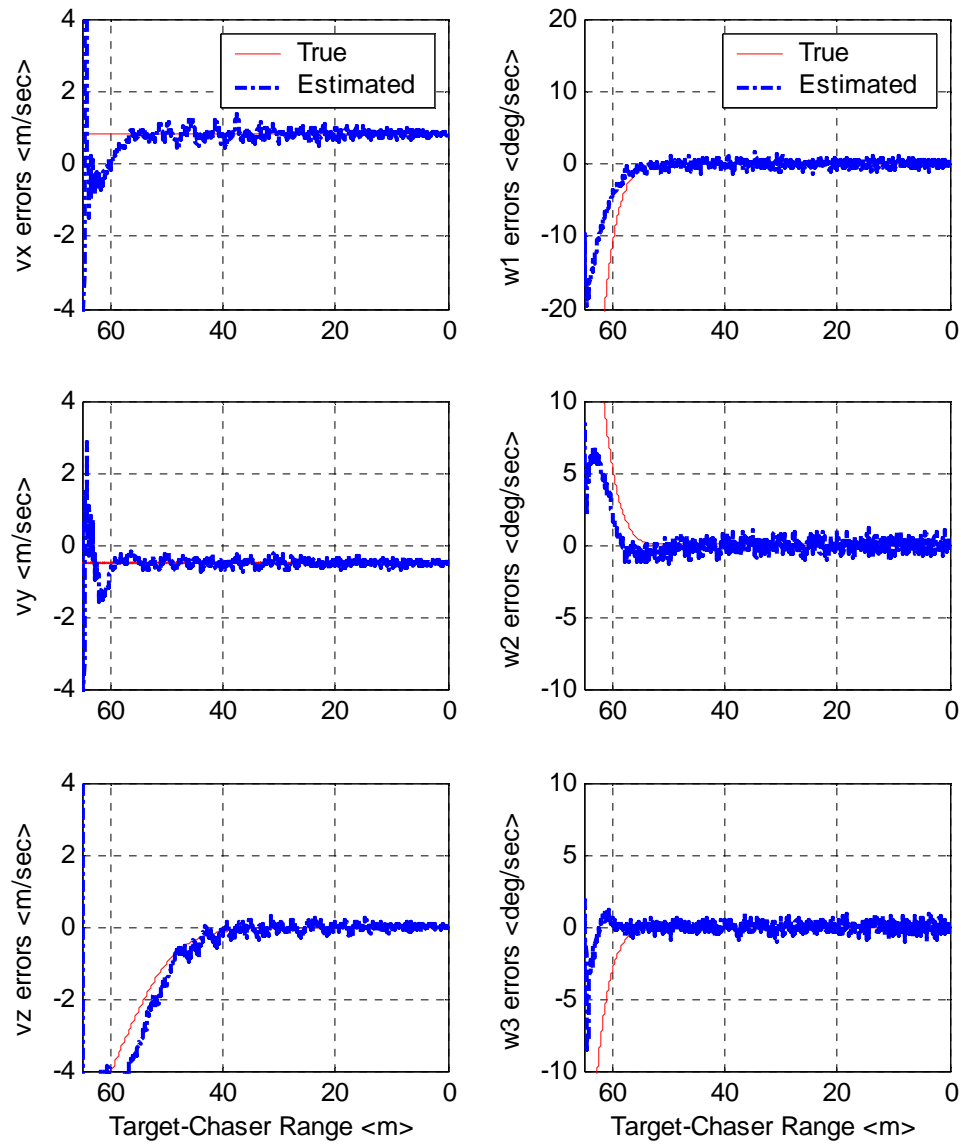


Figure 39 Linear velocity/angular rate estimation of EKF with zero acceleration model (Approach phase)

Table 6 Acceleration and gyro error specifications for the IMU

Accelerometer Error			
	Bias	White noise (Std.)	Bias noise (Std.)
x-axis	$0.3\cos(t/100) < m/sec^2 >$	$1.0 \times 10^{-3} < m/sec^2 >$	$1.0 \times 10^{-8} < m/sec^2 >$
y-axis	$0.3\cos(t/200) < m/sec^2 >$	$1.0 \times 10^{-3} < m/sec^2 >$	$1.0 \times 10^{-8} < m/sec^2 >$
z-axis	$0.3\sin(t/100) < m/sec^2 >$	$1.0 \times 10^{-3} < m/sec^2 >$	$1.0 \times 10^{-8} < m/sec^2 >$
Gyro Error			
	Bias	White noise (Std.)	Bias noise (Std.)
x-axis	$2\sin(t/100) < deg/sec >$	$8.0 \times 10^{-3} < deg/sec >$	$1.0 \times 10^{-8} < deg/sec >$
y-axis	$2\sin(t/200) < deg/sec >$	$1.0 \times 10^{-3} < deg/sec >$	$1.0 \times 10^{-8} < deg/sec >$
z-axis	$2\cos(t/100) < deg/sec >$	$1.0 \times 10^{-3} < deg/sec^2 >$	$1.0 \times 10^{-8} < deg/sec >$

6.3 EKF Implementation with VisNav/IMU Integration

For implementation of the VisNav/IMU integrated EKF, it was assumed that the IMU performance was as shown in Table 6. The bias and standard deviation of noise of accelerometer and gyro applying to the measurement simulation are selected based on the specification of Crossbow IMU-300CB in Table 4. To show a typical convergence, the initial estimates for the EKF implementation are set to 80% of their respective true state values. This initial estimates accuracy is corresponding to the GLSDC accuracy at the beginning stage of the simulation.

The initial covariance matrix is set to the following diagonal matrix:

$$P_o = 10^3 I_{15 \times 15} \quad (6.3)$$

and the covariance matrix of process noise Q is assumed to be

$$Q = \begin{bmatrix} 0_{3 \times 3} & & & & & \\ & 10^{-10} I_{3 \times 3} & & & & \\ & & 10^{-10} I_{3 \times 3} & & & \\ & & & 0 & & \\ & 0 & & & 10^{-4} I_{3 \times 3} & \\ & & & & & 10^{-4} I_{3 \times 3} \end{bmatrix} \quad (6.4)$$

In order to check the feasibility in case of VisNav measurements drop out, it was assumed that only two beacons are within the field-of-view for 1 second at 37 meters far from the target and all beacons are out of field-of-view for 1 second at 18 meters far from the target.

The position/attitude errors and 3-sigma bounds using VisNav/IMU EKF are shown in Figure 40 and Figure 41 . The position errors at the beginning of the navigation are around 1 meters, and reduce to errors less than 1 millimeter as the chaser reaches its target just in front of the beacons. The attitude errors at the beginning of the maneuver are around 1 degree, and reduce to values less than 0.01 degree at final stage.

The VisNav/IMU also provides precise dynamic information such as linear velocity, angular rate, and linear acceleration. Figure 42 shows the linear velocity and angular rate errors and 3-sigma bounds. Consequently, the VisNav/IMU integrated EKF permits the improved and continuous state estimates in case of VisNav measurements dropout for a short duration. The VisNav/IMU integrated EKF state estimates remains stable during the complete loss of VisNav measurements.

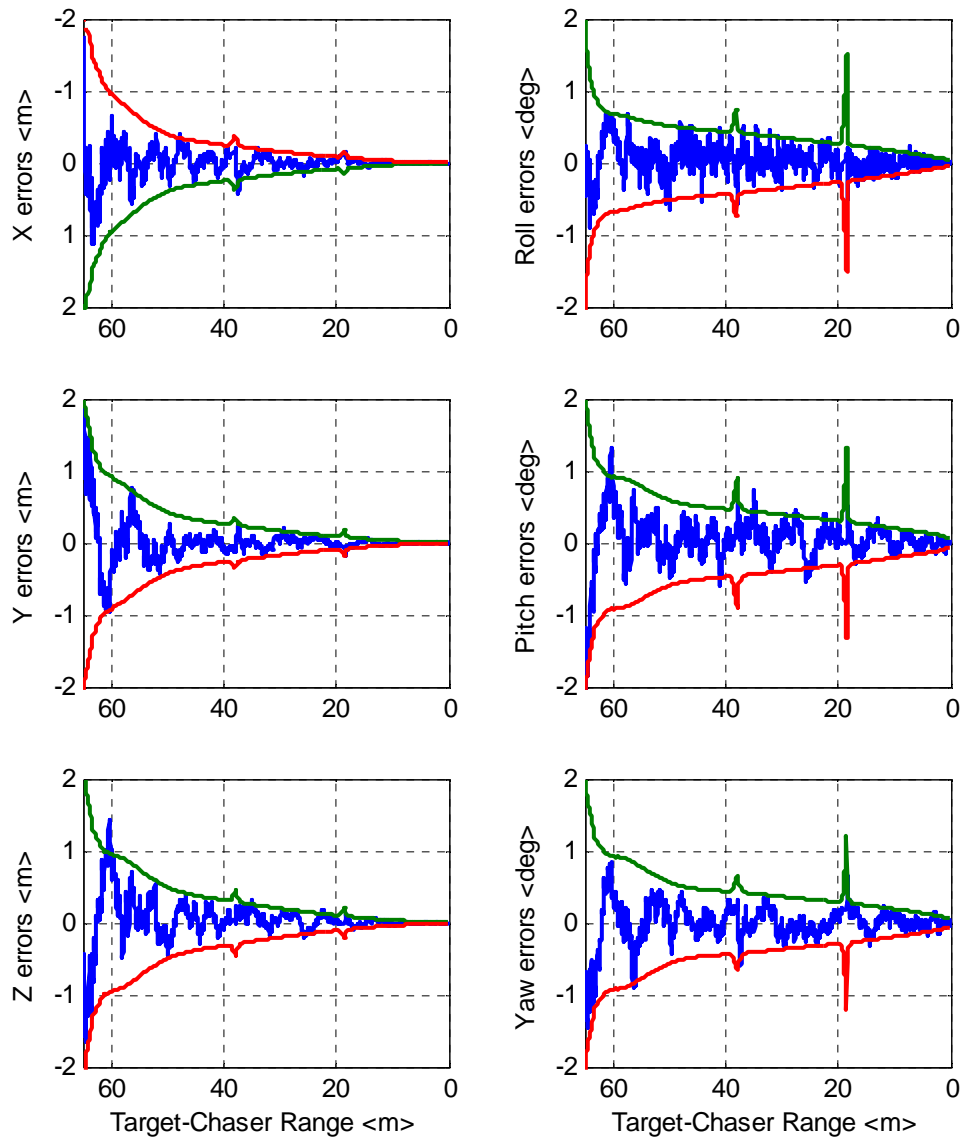


**Figure 40 Position/attitude errors and 3-sigma bounds of EKF with IMU
(Approach phase)**

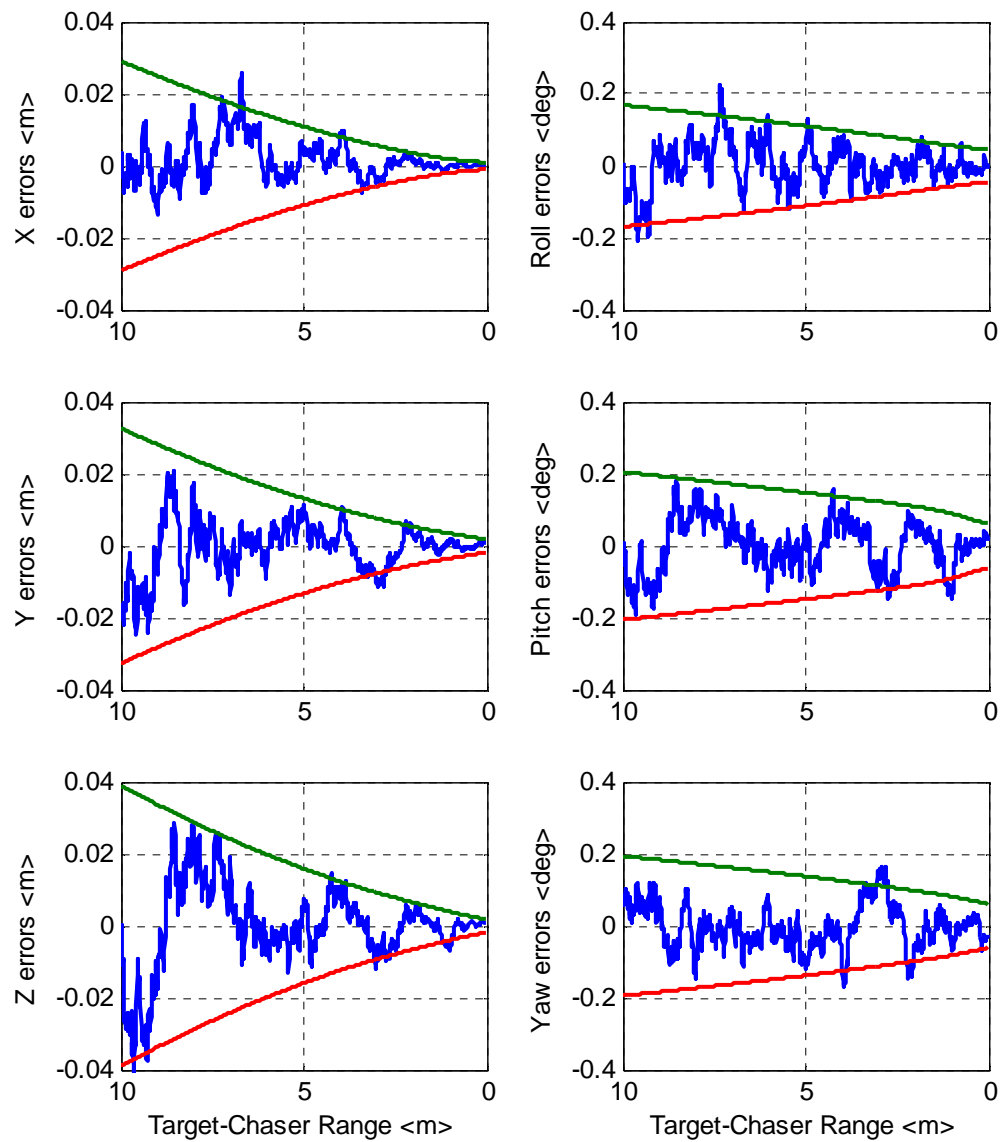


**Figure 41 Position/attitude errors and 3-sigma bounds of EKF with IMU
(End-game)**

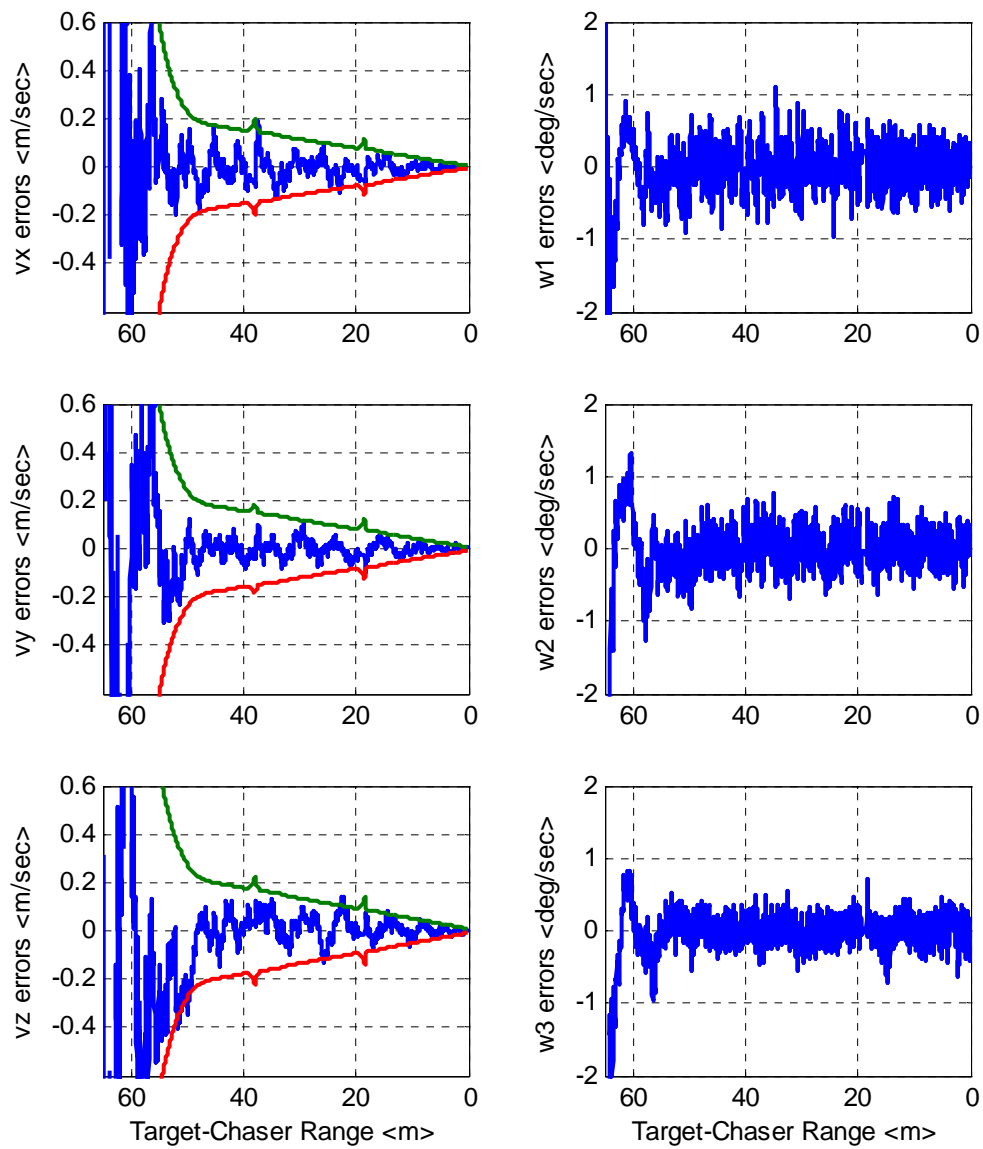


**Figure 42 Linear velocity/angular rate errors of EKF with IMU
(Approach phase)**

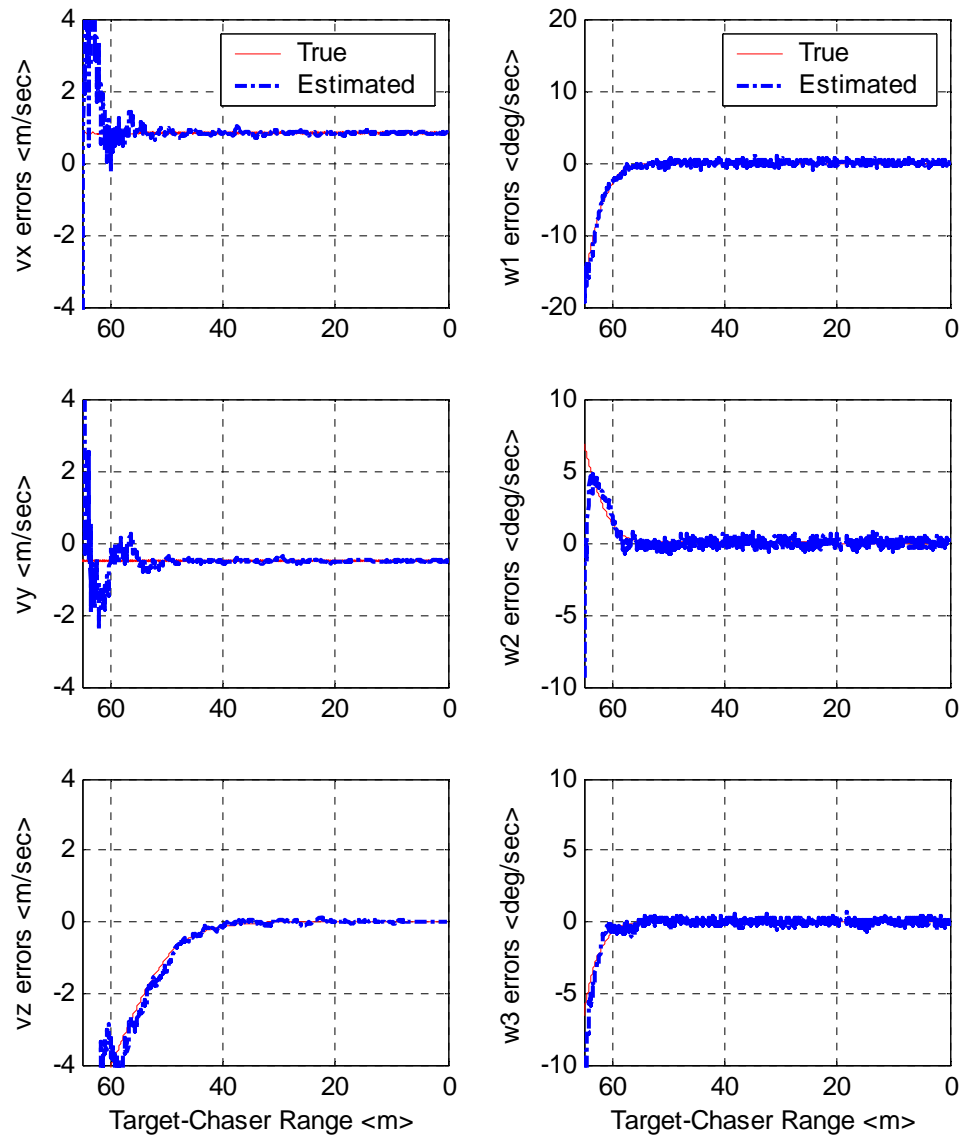


**Figure 43 Linear velocity/Angular rate estimation of EKF with IMU
(Approach phase)**

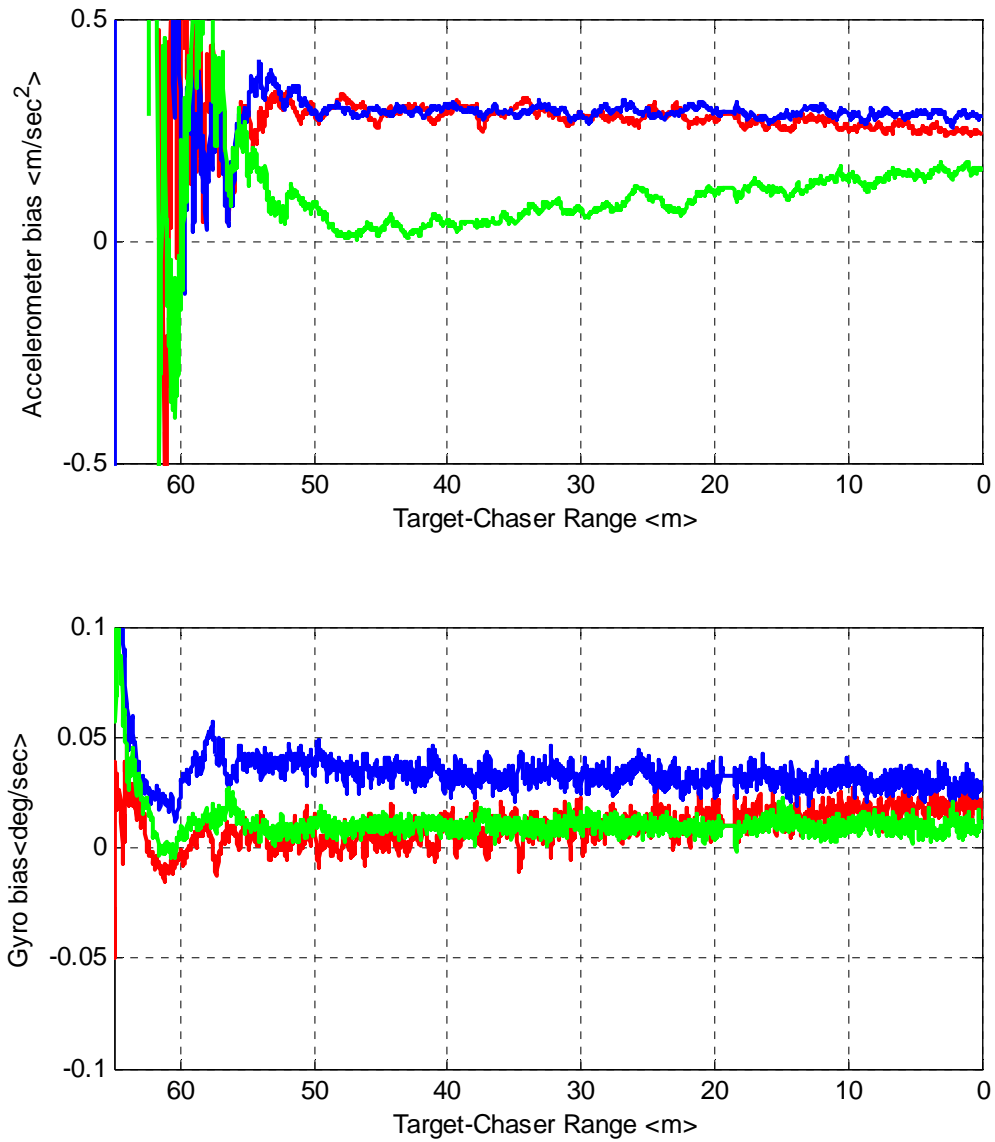


**Figure 44 Accelerometer bias/ gyro bias estimation of EKF with IMU
(Approach phase)**

Table 7 Navigation accuracy summary

Target-chaser range <m>	Navigation accuracy (1σ)					
	Relative position accuracy <m>			Relative attitude accuracy <deg>		
	GLSDC	Zero accel.	VisNav/IMU	GLSDC	Zero accel.	VisNav/IMU
60	4	0.3	0.3	4	0.3	0.3
30	1	0.1	0.06	2	0.2	0.1
10	0.15	0.02	0.01	0.8	0.1	0.06
5	0.01	0.003	0.002	0.2	0.05	0.02
Dock	0.003	0.001	0.0005	0.1	0.03	0.01

6.4 Discussion

As the vehicle approaches to the target, the navigation accuracies of both GLSDC and dynamics state estimation solution become significantly better due to better geometric condition for triangulation. GLSDC successfully determined the position and attitude through several iterations even given a poor initial guess. The nonlinearities of measurement model and state model are reduced using MRPs. However, the iteration caused a computational load and GLSDC geometric solution is sensitive to the measurement noise, especially as range to the beacons increase. The EKF with zero acceleration model determined the position and attitude as well as the linear velocity and angular rate, without iteration. Since the VisNav sensor gives the line-of-sight vector measurements at a very high rate, the zero acceleration model is reasonable (assuming that the linear velocity and angular rate are piecewise constant during the time interval of each measurements). The EKF results shows a more stabilized and accurate solution,

as compared to the GLSDC results. The position and attitude errors of EKF were reduced about one order of magnitude compared to the GLSDC. Furthermore, EKF is more efficient from a computational point of view by avoiding iteration procedure for each set of measurements.

The simulated navigation accuracy is summarized with reference to Table 7. These accuracies are improved somewhat with respect to the EKF without the IMU, however the robustness with respect to data dropout is vastly improved. The accuracy, bandwidth, and robustness of the integrated VisNav/IMU navigation system are superior to any other existing proximity navigation approach.

CHAPTER VII

SUMMARY AND CONCLUSION

In this dissertation, an analytical, computational, and experimental study of proximity navigation is reported. Central to the approach, a recently developed analog optical navigation sensor system (VisNav) is considered. This sensor orchestrates the energy emitted by four or more optical beacons to optimize the signal-to-noise of individual measurement and eliminate the pattern recognition problem altogether.

A central difficulty that comes with application of the VisNav system is calibration of the systematic departure from the ideal co-linearity relationship of the object-to-image projection. The calibration process developed lead to errors on the order of one part in 100 being reduced to about one part in 1000.

GLSDC was developed for determining the best geometric position and attitude information from each set of 4 or more measurements. By considering the MRPs as attitude parameters, robust convergence with respect to the poor initial guess was achieved as well as computational efficiency.

Two EKF filter algorithm were developed for recursive dynamic state estimation, the first used only VisNav measurements and the second integrated VisNav and IMU measurements. It was found that the VisNav/IMU integration using EKF achieved substantially superior performance, and eliminating the need for a dynamical model (for acceleration level motion), and also making the system robust in the presence of occasional VisNav data dropout .

Several issues remain to be better addressed in future research, as follows:

1. The calibration process needs to be refined to find optimal basis functions that optimize storage and real-time computational burden.

2. The VisNav hardware design needs to be further optimized to minimize measurement error and thereby improve the accuracy of the resulting navigation solution.
3. Consider the case of range being too great to geometrically solve for the navigation estimation problem via GLSDC. The line-of-sight to the beacons still contains information, than the integrated system combined with an IMU should result in a navigation solution.

REFERENCES

- [1] E. Nebot, "Sensors Used for Autonomous Navigation," in *Advanced Intelligent Autonomous Systems*, S.G Tzafestas, ed., Boston: Kluwer Academic Press, 1999, pp. 135-156.
- [2] K. R. Britting, *Inertial Navigation System Analysis*, New York: Wiley, 1971.
- [3] A. B. Chatfield, *Fundamentals of High Accuracy Inertial Navigation*, Washington, DC: AIAA series, 1997.
- [4] J.L. Junkins, H. Schaub, and D. Hughes, "Noncontact Position and Orientation Measurement System and Method," U.S. Patent No. US 6,266,142 B1, Issued July 24, 2001.
- [5] B. Parkinson and J. Spiker, Jr., *Global Positioning System: Theory and Applications*. Washington, DC: American Institute of Aeronautics and Astronautics, Inc., 1996.
- [6] J. Lomas and J. Blucker, "Precision Relative Navigation for Automated Rendezvous and Docking," in *Proc. of 22nd Annual AAS Guidance and Control Conference*, Breckenridge, CO, Feb. 1999, pp. 368-379.
- [7] M. Polites, "An Assessment of the Technology of Automated Rendezvous and Capture in Space," Marshall Space Flight Center, AL, NASA/TP-1998-208528.
- [8] P. Calhoun and R. Dabney, "A Solution to the Problem of Determining the Relative 6 DOF State for Spacecraft Automated Rendezvous and Docking," *SPIE* vol. 24667, pp. 175-184.
- [9] T. Sutherland, "Unmanned Vehicle Guidance Using Video Camera/Vehicle Model," Marshall Space Flight Center, AL, NASA/TM-1999-209788.
- [10] J. Junkins, D. Hughes, and K. Wazni, V. Pariyapong, "Vision-Based Navigation for Rendezvous, Docking, and Proximity Operations," in *Proc. of 22nd Annual AAS Guidance and Control Conference*, Breckenridge, CO, Feb. 1999, pp. 203-220.

- [11] H. Schaub, "Real-Time Stereo Vision Using Laser Scanning and Position Sensitive Photodetectors: Analytical and Experimental Results," M.S. Thesis, 1994, Texas A&M University, College Station, TX.
- [12] K. Gunnam, D. Hughes, J. Junkins, and N. Kehtarnavaz, "A DSP Embedded Optical Navigation System," *IEEE Sensor Journal*, vol. 2, no. 5, pp. 428-442, 2002.
- [13] K. Wazni, "Vision Based Navigation Using Novel Optical Sensors," M.S. thesis, Texas A&M University, College Station, TX, 1999.
- [14] F. Moffitt, *Photogrammetry*, New York: Harper and Row, 1980.
- [15] On-Trak Photonics Inc, "Position Sensing Detectors: Theory of Operation," www.on-trak.com, 2000.
- [16] UDT Sensor Inc, "Photodiode Characteristic," www.udt.com, 2002.
- [17] J. Weng, P. Cohen, and M. Herniou, "Camera Calibration with Distortion Models and Accuracy Evaluation," *IEEE Transactions on Pattern Analysis and Machine Intelligence*, vol. 14, no. 10, pp. 965-980, 1992.
- [18] S. Shah and J. Aggarwal, "Intrinsic Parameter Calibration Procedure for a High-Distortion Fish-Eye Lens Camera with Distortion Model and Accuracy Estimation," *Pattern Recognition*, vol. 29, no. 11, pp. 1775-1788, 1996.
- [19] J. Fryer, D. Brown, "Lens Distortion for Close-Range Photo-grammetry," *Photogrammetric Engineering and Remote Sensing*, vol 52, no. 1, pp. 51-58, 1986.
- [20] Z. Zhang, "A Flexible New Technique for Camera Calibration," *IEEE Transactions on Pattern Analysis and Machine Intelligence*, vol. 22, no. 11, pp. 1330-1334, 2000.
- [21] R. Hartley. "An Algorithm for Self Calibration from Several Views," in *Proc. of the IEEE Conference on Computer Vision and Pattern Recognition*, Seattle, WA, June 1994, pp. 908-912.

- [22] R. Tasi, "A Versatile Camera Calibration Technique for High Accuracy 3D Machine Vision Metrology Using Off-the-Shelf TV Cameras and Lense," *IEEE Journal of Robotics and Automation*, vol. 3, no.4, pp 323-345, Aug. 1987.
- [23] D. Kincaid and W. Chaeney, *Numerical Analysis*, Berkeley: Brooks/Cole Publishing Company, 1996.
- [24] J. Junkins, G. Miller, and J. Jancaitis, "A Weighting Function Approach to Modeling of Irregular Surfaces," *Journal of Geophysical Research*, vol. 78, no. 11, pp. 1794-1803, 1973.
- [25] C. Fraser, M. Shortis, "Variation of Distortion within the Photographic Field," *Journal of Photogrammetric Engineering and Remote Sensing*, vol. 58, no. 6, pp. 851-855, 1992.
- [26] G. Wahba, "A Least-Squares Estimate of Satellite Attitude," *SIAM Review*, vol. 7, no. 3, pp. 409, 1965.
- [27] M. Shuster, S. Oh, "Three-Axis Attitude Determination from Vector Observations," *Journal of Guidance and Control*, vol. 4, no. 1, pp. 70-77, 1981.
- [28] J. Crassidis, R. Alonso, and J. Junkins. "Optimal Attitude and Position Determination from Line-Of-Sight Measurements," in *Proc. Richard H. Battin Astrodynamics Conference*, College Station, TX, March 2000, pp. 268-280.
- [29] H. Schaub and J. Junkins, *Analytical Mechanics of Space Systems*, Washington, DC: AIAA Education Series, 2003.
- [30] J. Wertz, *Spacecraft Attitude Determination and Control*, Boston: D. Reidel Publishing Company, 1978.
- [31] J. Crassidis and F. Markley, "Attitude Estimation Using Modified Rodrigues Parameters," in *Proc. of the Flight Mechanic/Estimation Theory Symposium*, NASA-Goddard Space Flight Center, Greenbelt, MD, 1996, pp. 71-83.
- [32] J. Crassidis and J. Junkins, *Optimal Estimation of Dynamics Systems*, Boca Raton, FL: Chapman and Hall/CRC, 2004.
- [33] R. Brown and Y. Hwang, *Introduction to Random Signals and Applied Kalman Filtering*, New York: Wiley, 1997.

- [34] E. Lefferts, F. Markley, and M. Shuster. “Kalman Filtering for Spacecraft Attitude Estimation,” *Journal of Guidance*, vol. 5, no. 5, pp. 417-429, 1982.
- [35] M. Farrel, *The Global Positioning System and Inertial Navigation*, New York: McGraw-Hill, 1999.
- [36] E. Nebot and H. Durrant-Whyte, “Initial Calibration and Alignment of Low Cost Inertial Navigation Units for Land Vehicle Applications,” *Journal of Robotics Systems*, vol 16, no.2, pp. 81-92, 1999.
- [37] D. Gaylor, “GPS/INS Kalman Filter Design for Spacecraft Operating in the Proximity of the International Space Station,” Ph.D. dissertation, University of Texas, Austin, TX, 2003.
- [38] Crossbow Technology Inc, “Crossbow DMU User’s Manual”, www.xbow.com, San Jose, CA, 1999.

VITA

Ju-Young Du was born in Chonju, Korea, on April 19, 1973, the eldest daughter of Byoung-Sun Du and Kyoung-Ja Kim. She has two brothers and two sisters. She received the Bachelor of Science and Master of Science degrees in astronomy from Yonsei University, Seoul, Korea in 1996 and 1998, respectively. While she was attending Yonsei University for her M.S. degree, she also served as a part time member of the engineering staff for Korea Electronics and Telecommunications Research Institute (ETRI). She enrolled in the Department of Aerospace Engineering at Texas A&M University in the fall of 1999 and earned her Doctor of Philosophy in aerospace engineering in December 2004. Her research interests include navigation sensor systems and their applications, dynamics and control, and optimal estimation theory.

The author can be reached at judu419@yahoo.com. Her permanent address is 116-15 Sillim-dong, Kwanak-ku, Seoul, Republic of Korea.